NTNU
Norwegian University of
Science and Technology

Nonlinear Modeling, Controller and Observer Design for Roll Damping on a Surface Effect Ship with Split Air Cushion

Håkon Engebretsen Bryn
Jonas Tønnessen

Master of Science in Cybernetics and Robotics

Submission date:	June 2017
Supervisor:	Jan Tommy Gravdahl, ITK
Co-supervisor:	Vahid Hassani, IMT Øyvind Auestad, Umoe Mandal

Norwegian University of Science and Technology
Department of Engineering Cybernetics

Preface

In this Master thesis, a roll damping control system for a surface effect ship (SES) with a longitudinally split air cushion is developed, implemented and tested in co-operating with Umoe Mandal. Håkon Engebretsen Bryn and Jonas Tønnessen, from the Department of Engineering Cybernetics at NTNU, have co-operated and developed both a linear control plant model and a nonlinear process plant model to catch the roll dynamics off the vessel.

We would like to thank our supervisors Professor Jan Tommy Gravdahl (Department of Engineering Cybernetics, NTNU), Adjunct Associate Professor Vahid Hassani (Department of Marine Technology, NTNU) and Dr. Øyvind Auestad (Umoe Mandal). Thank you Jan Tommy Gravdahl for meeting arrangements, support and being helpful all the way through the process. We would like to thank Vahid Hassani, specifically for being a great resource during the model test period, thank you for being so interested and always checking in to see if we need any help. A special thanks goes to Øyvind Auestad, for always being there for us, we can not thank you enough for all the effort you have put in. From all the meetings to the long evenings during the model tests, and also the genuine wish you have in our success.

We would like to thank all the employees at Marintek and Sintef Ocean that has given a helping hand. A special thanks goes to Terje Rosten (Marintek) for the great help with getting everything ready for the modeltests, and the support during the tests. We would also like to thank Torgeir Wahl (Marintek) for help with setting up the controller.

At last we want to thank Umoe Mandal and the Research Council of Norway MAROFF project 256442 for the opportunity to work with this project.

Abstract

For the first time, a controller is presented for roll motion damping, exclusively by the use of air cushion pressure, on a surface effect ship (SES) with a longitudinally split air cushion. The Wave Craft, manufactured by Umoe Mandal, is considered in this study. Experimental testing of the control system and split cushion design is done by utilizing a model scale vessel. The roll motion dynamics are modeled, and together with the pressure dynamics for the air cushions included in a linear control plant model and a nonlinear process plant model. The models are implemented in Simulink and verified through model test comparisons. A tunable and a hybrid PID controller is implemented and tested. Two Kalman filters are implemented to provide suitable feedback signals for the controllers.

Model test results indicate that roll motions are damped significantly. A roll motion damping percentage of 63% and 92% can be achieved for beam and quartering seas, respectively. The control system is also able to reduce both heave and roll motions, simultaneously. The Boarding Control System (BCS) is able to perform its objective when using the split cushion design; namely, damping of vertical bow motions. Hence, the split cushion design should be considered implemented for the full scale vessel.

For future work, the simulation models should be developed further by modeling the pressure dynamics more realistic. Leakages and inertia for the pressure propagation should be considered. The control system should be able to damp roll motions when the wave craft is free floating at zero speed and when it is in contact with a wind turbine. This should also be included in the mathematical models, by adding friction forces and moments acting between the vessel and the turbine. A hybrid control system for multiple DOF damping should also be considered, as the foundation already is implemented in this project.

Contents

List of Figures

List of Tables

Nomenclature

C_A^*	Linearized coriolis-centripetal matrix due to hydrodynamic added mass.
C_{RB}^*	Linearized coriolis-centripetal matrix due to rigid-body mass.
M	Mass matrix.
α	Angle of the bow skirt.
$\bar{\psi}$	Vessel heading.
$\bar{\zeta}$	Wave amplitude.
$\bar{K}(t)$	Matrix of retardation functions.
χ	Wave propagation direction with respect to the body frame.
$\delta\nu$	Matrix of retardation functions.
ΔA_i^{ctrl}	Controlled leakage areas for, $i = \{s, p\}$, starboard and port air cushion
$\dot{V}_0(t)$	Wave volume pumping
ϵ	Wave phase.
η	Generalized position vector.
η_i	Heave displacement, roll angle and pitch angle, $i = \{3, 4, 5\}$
γ	Ratio of specific heat for air
λ	Wave length
μ	Fluid memory effects.
μ_{u_i}	Relative pressure parameter for $i = \{s, p\}$ starboard and port air cushion
ν	Generalized velocity vector.
ν_r	Relative velocity vector, taking ocean current into account
ω	Angular rate vector, $[p, q, r]^\top$
ω	Circular wave frequency.
ω_e	Encountered wave frequency
Ω_i	Cushion volume for $i = \{s, p\}$.
ρ_a	Air density at P_a

ρ_{c0}	Density of air inside the cushion at P_0
$\rho_{c_i}(t)$	Air density inside cushion for $i = \{s, p\}$.
$\tau_{cushion}$	Cushion forces.
τ_{exc}	External forces.
τ_{hyd}	Radiation-induced hydrodynamic forces.
Θ	Euler angle vector, $[\phi, \theta, \psi]^\top$
ζ_a	Wave amplitude
$\zeta_i(x, y, t)$	Spatial wave elevation for $i = \{s, p\}$.
$\{b\}$	Body coordinate frame of the vessel
$\{m\}$	Measurement coordinate frame
$\{n\}$	NED coordinate frame
$\{S\}$	Seakeeping frame.
A_c	Single air cushion area
A_0^{CTRL}	Mean operating value for vent valve leakage area
A_{c_p}	Port air cushion area
A_{c_s}	Starboard air cushion area
A_{ii}	Added mass coefficients $i = \{3, 4, 5\}$
A_i^j(t)	Leakage areas for $j = \{hull, wall, seals, ctrl\}$ and $i = \{s, p\}$
A_{L_i}	Total leakage area for $i = \{s, p\}$, starboard and port air cushion
$A(\omega)$	Frequency dependent added mass matrix.
$B(\infty)$	Potential damping.
$B_V(\infty)$	Viscous damping.
B_{ii}	Potential damping coefficients $i = \{3, 4, 5\}$
$B_{total}(\infty)$	Sum of potential and viscous damping.
$B(\omega)$	Frequency dependent added mass matrix.
c_n	Vent valve shape coefficient
C_{ii}	Restoring coefficients for $i = \{3, 4, 5\}$
D	Total linear damping.
$F_i^e(t)$	Wave excitation forces for $i = \{3, 4, 5\}$
F_i	Pressure induced forces for $i = \{s, p\}$ starboard and port air cushion
$h_{c_i}(t)$	Spatial height from the baseline to the wet deck for $i = \{s, p\}$.

h_h	Distance from the baseline to the wet deck.
I_{44}	Moment of inertia around body x-axis
I_{55}	Moment of inertia around body y-axis
$J_{\boldsymbol{\Theta}}(\boldsymbol{\eta})$	Kinematic transformation matrix.
K_i	Constants related to the linearized pressure dynamics. $i = \{1, 2, 3\}$
L, h_0	Length and height of the air cushions, respectively
$L_i(t)$	Length of cushion for $i = \{s, p\}$.
m	Mass of vessel
M_A	Constant infinite-frequency added mass matrix.
M_{RB}	Inertia matrix.
p_0	Equilibrium cushion pressure
p_a	Atmospheric pressure
$p_i(t)$	Total pressure for $i = \{s, p\}$ starboard and port air cushion
p_{u_i}	Excess pressure for $i = \{s, p\}$ starboard and port air cushion
q	Number of lift fans
Q_0	Equilibrium airflow at the equilibrium pressure
Q_{in}	Volumetric inlet airflow for the air cushions
Q_{out_i}	Volumetric outlet airflow for $i = \{s, p\}$ starboard and port air cushion
$T_0(x)$	Mean draught value.
$T_i(t)$	Draughts for $i = \{s, p\}$.
U	Vessel speed.
$V_{0_i}(t)$	Volume inside the cushion due to waves for $i = \{s, p\}$.
$W_i(t)$	Width of cushion for $i = \{s, p\}$.
$x_{AP/CG}$	Longitudinal distance between AP and CG
$x_{bag/CG_i}(t)$	x coordinate of the bag relative to CG for $i = \{s, p\}$
x_{bag}	Length of the aft bag.
$x_{bow/CG_i}(t)$	x coordinate of the bow relative to CG for $i = \{s, p\}$
$x_{cp_i}(t)$	Longitudinal distance between CG and CP for $i = \{s, p\}$
x_{cp}	Longitudinal distance between CG and CP
$x_{FP/CG}$	Longitudinal distance between FP and CG
y_{c0}	Cushion width for $\eta_4(t) = 0$

$y_{cp_i}(t)$	Transverse distance between CG and CP for $i = \{s, p\}$
y_{cp}	Transverse distance between CG and CP
z_{bag}	Height of the aft bag.

Chapter 1

Introduction

A control system for damping of roll motions on a surface effect ship (SES) is presented. The traditional SES, which is introduced and explained in Chapter 1.3, is slightly modified by installing a longitudinally separating wall which splits the air cushion into one starboard and one port air cushion.

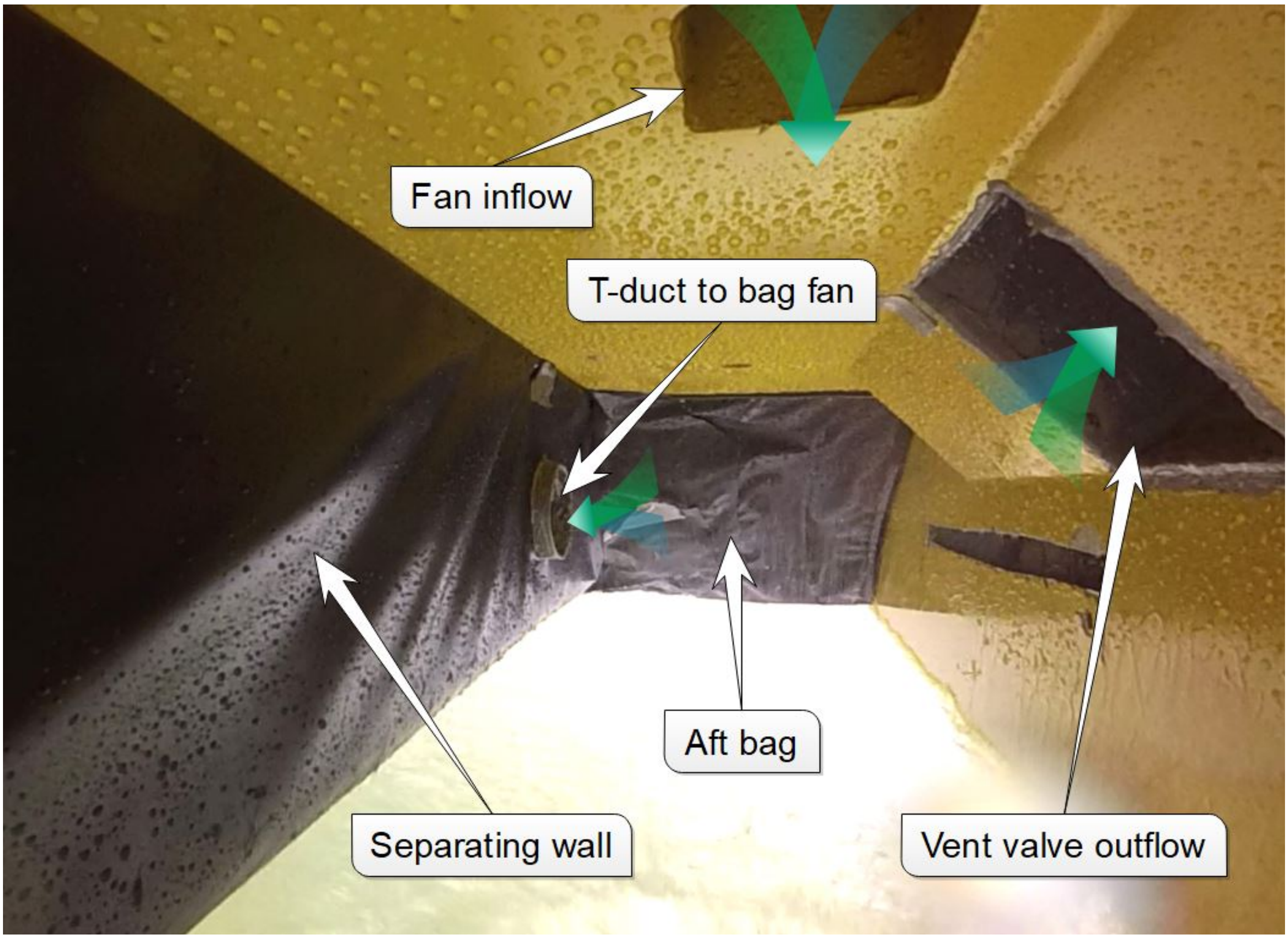

Figure 1.1: Port air cushion on the modified SES.

Figure 1.1 shows the modified SES. The work presented in this thesis deals with air cushion pressure control in these two air cushions for roll motion damping. Roll reduction will increase turbine accessibility in wave headings approximately between 45-135 degrees. Also, according to O'Hanlon and McCauley (1974), vertical accelerations have significant effect on seasickness. Since vertical motions in the NED frame is coupled with the current roll and pitch angles of the craft (Fossen, 2011), it is expected that damping of roll motions will induce less seasickness. This led to the work of Bryn (2016) and Tønnessen (2016), where a longitudinally split air cushion and a roll damping control system were designed for a control plant model. Simulations indicated that roll motions could be damped by exploiting this design, which further led to this Master thesis where a roll damping control system and separating wall design were developed, implemented and tested on a model scale vessel.

1.1 Background and Motivation

The Wave Craft project for wind farm service was initiated by Umoe Mandal in 2010/2011. The Wave Craft is a Crew Transfer Vessel (CTV) which transfers service crew from shore to offshore wind farms. In 2011, Umoe Mandal started to investigate the possibilities for vertical motion damping on the Wave Craft. Auestad (2015) lead to a control system for active air cushion control to reduce vertical motion; namely, the Boarding Control System (BCS). This control system was mainly developed for safer transfer of personnel and equipment between the vessel and an offshore wind turbine. Since it reduces vertical motions, in zero or low speeds, it also serves for comfort and reducing seasickness.

Figure 1.2: The Wave Craft (Courtesy of Umoe Mandal)

New wind farms are located further from shore and for deeper waters as seen from Figure 1.3. This is the main motivation behind the development of the Wave Craft. The wind farm location tendency favours the Wave Craft due to its high speed and comfort in various sea states. The sharply increasing trend for cumulative capacity of offshore wind installations the past decade, shown in Figure 1.4, indicates that the wind farm market grows. Hence, the demand for a product that is able to transfer personnel safe, comfortable and fast between shore and wind farms is expected to increase in the near future.

Since SES offer great advantages in form of speed, comfort and safety, it is of great interest to investigate the SES concept further. The BCS already damps vertical bow motions, which is coupled by heave and pitch motions. By including a roll damping control system, all degrees of freedom in the vertical plane can be damped. Additionally, when damping of motions is not prioritized, the vent valves may be utilized to control surge, sway and yaw in the horizontal plane. Hence, a DP operation can be executed exclusively by use of the vent valves (Bua and Vamråk, 2016). Consequently, SES offers a unique total package of motion control/motion damping.

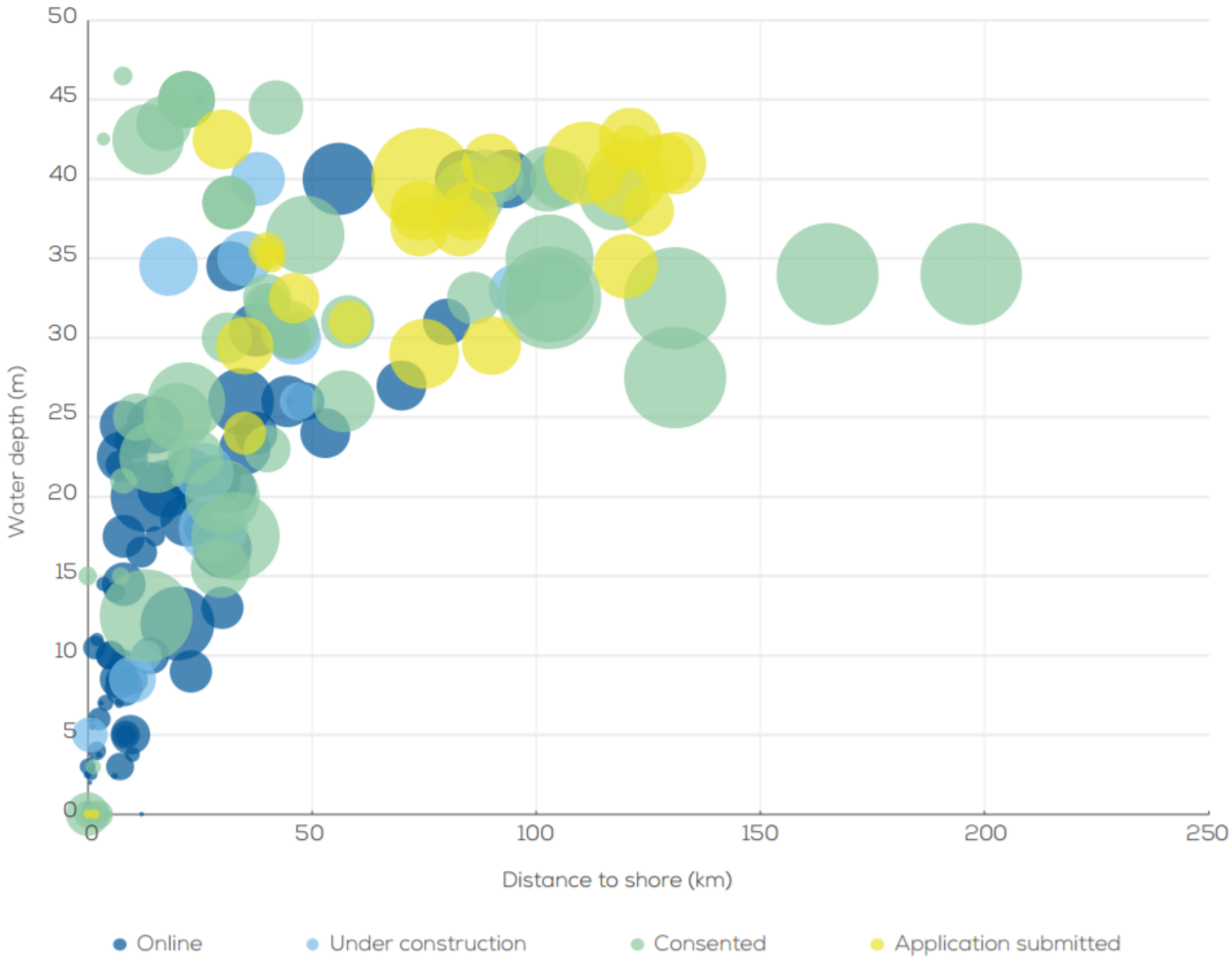

Figure 1.3: Development status for bottom-fixed offshore wind farms relative to their location and average water depth. The bubble sizes indicate the overall capacity of the site (WindEurope, 2017).

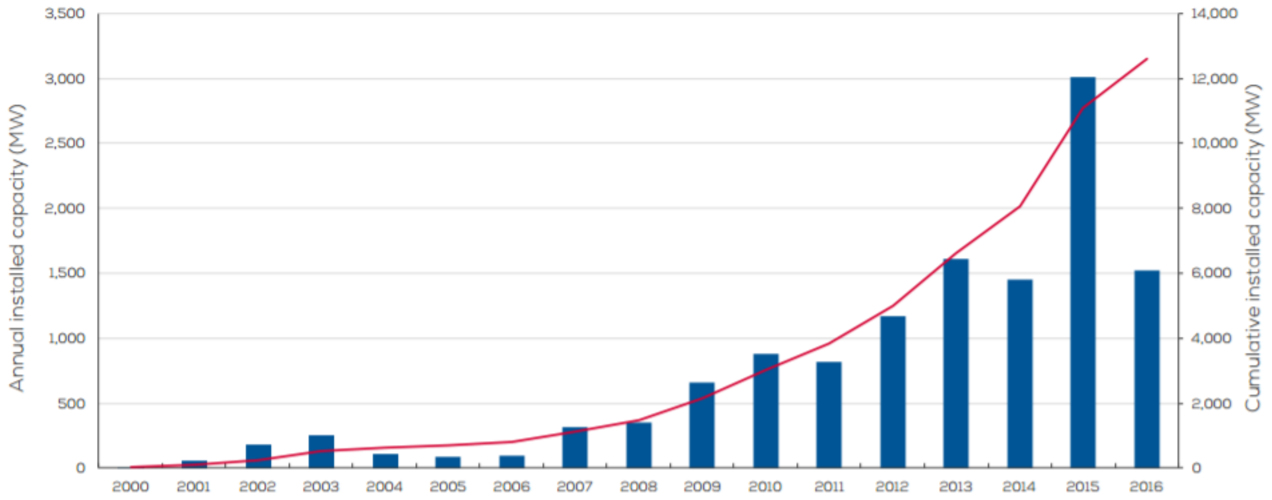

Figure 1.4: Cumulative and annual offshore wind installations 2000-2016. (WindEurope, 2017)

1.2 Roll Damping Systems

This section is based on Fossen (2011) and Perez (2005) and considers the most widely used systems for roll damping. The roll damping systems can conveniently be divided into two groups; passive and active systems. For passive systems, no separate source of power and control system are required. For active systems, a roll moment counteracting roll motions is induced by moving masses or control surfaces by means of power.

1.2.1 Passive Systems

Bilge Keels

Bilge keels act like fins and are often placed where the bilge turns as seen in Figure 1.5. Their length varies according to $25 - 50$ % of the length of the vessel. Bilge keels are widely used. They are inexpensive, but increases the hull resistance. They are effective mainly around the natural roll frequency of the ship. However, this effect decreases substantially with the speed of the ship.

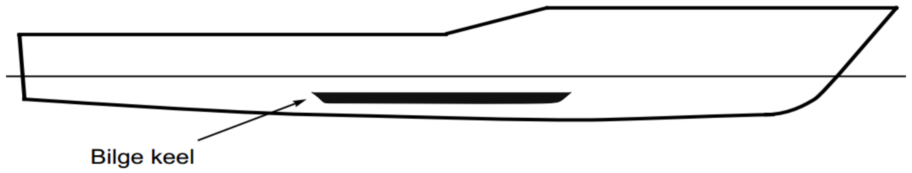

Figure 1.5: Bilge keel. (Perez, 2005)

Hull Modifications

Using hydrostatic and hydrodynamic properties, the shape and size of the ship hull can be optimized to minimize rolling motion. The disadvantage of this is that it needs to be implemented as the ship is built.

Anti-Rolling Tanks

Three types of anti-rolling tanks are frequently used; free-surface tanks, U-tube tanks and diversified tanks. Figure 1.6 displays a typical anti rolling tank setup. The main advantage of tank systems is that they provide roll damping even at low vessel speed. However, they reduce the metacentric height due to free water surface effects and also occupy a large amount of space. Anti-rolling tanks have been installed since 1874.

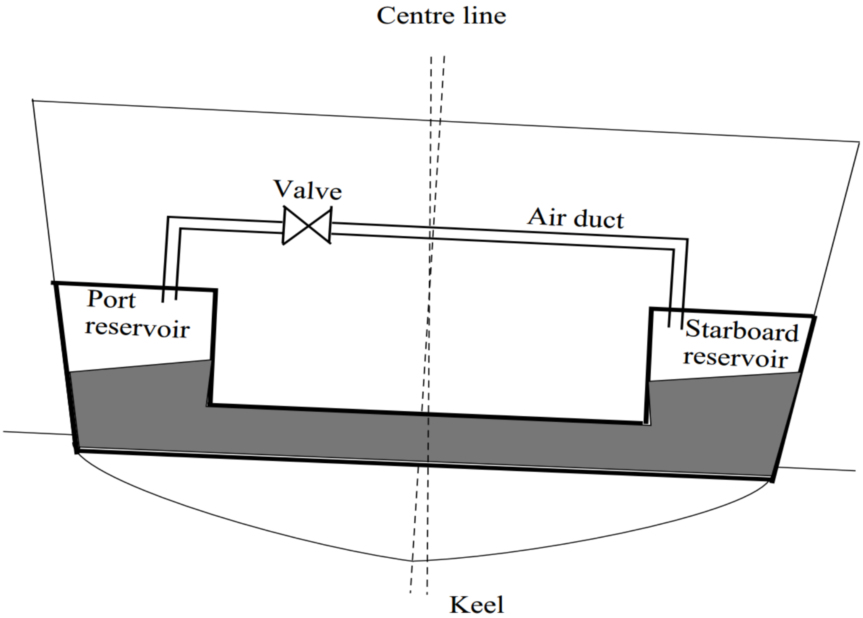

Figure 1.6: Anti-Rolling Tanks (Fossen, 2011).

1.2.2 Active Systems

Fin Stabilizers

Fin stabilizers, shown in Figure 1.7 provide significant roll damping when the vessel speed is not too low. At least two hydraulic systems must be installed, inducing a high cost associated with the first time installation. Fin stabilizers increases hull resistance and underwater noise, although this can be eliminated when they are not used, by implementing retractable fins. At low speed, they are ineffective.

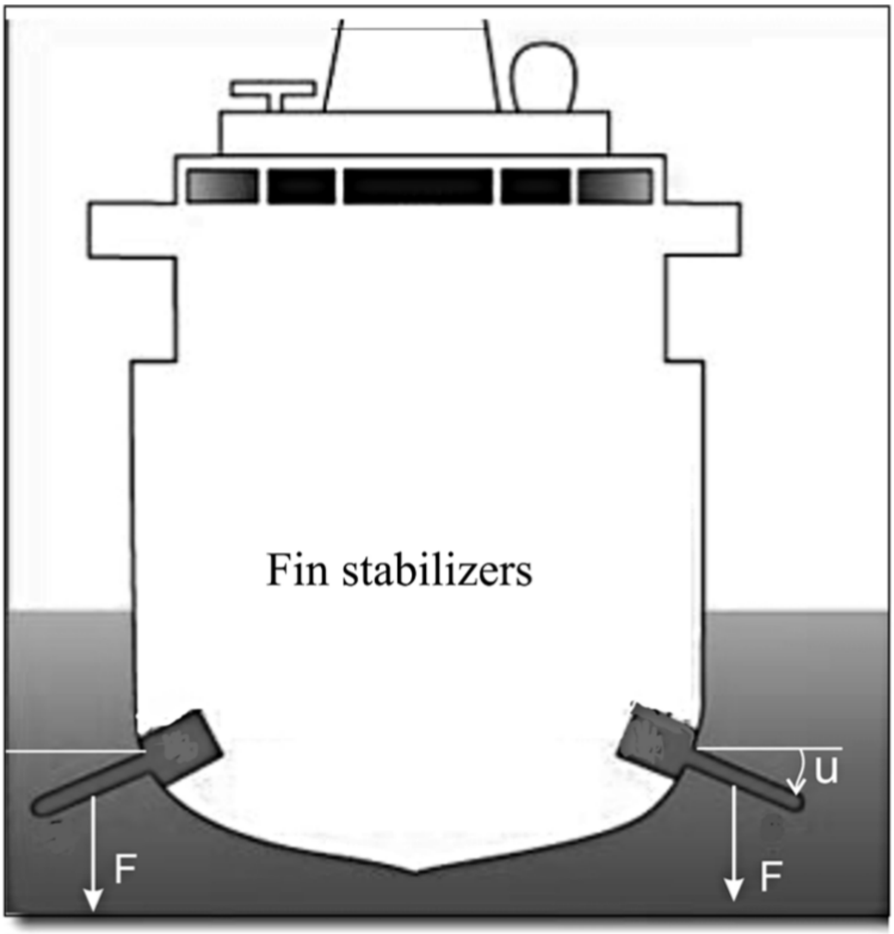

Figure 1.7: Fin stabilizers (Fossen, 2011).

Rudder-Roll Damping (RRD)

Compared to fin stabilizers, roll damping utilizing the rudder is relatively inexpensive, and has approximately the same roll damping performance. An illustration is shown in Figure 1.8. If the system is turned off, no drag or underwater noise are induced. The constraint is that in order for RRD to be effective, it requires a relatively fast rudder, and as with the fin stabilizers, RRD will not be effective for low speed applications.

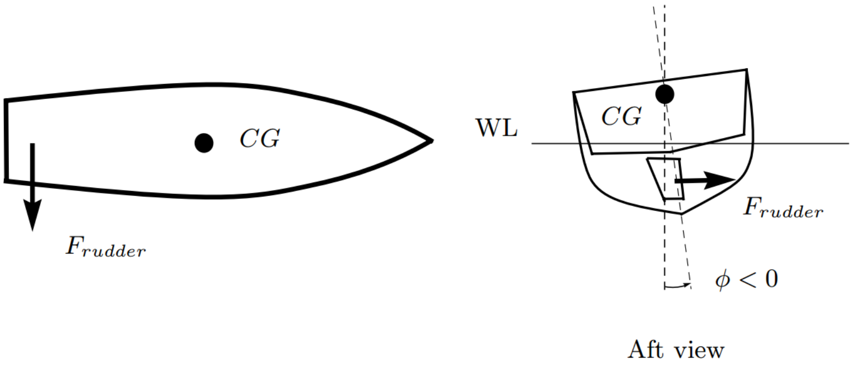

Figure 1.8: Rudder-Roll Damping (RRD) (Perez, 2005).

Gyroscopic Roll Stabilizers

A gyroscopic stabilizer has a spinning rotor that will generate a roll stabilizing moment that counteracts the wave-induced roll motions. They are typically used for boats and yachts under 100 feet, because unlike stabilizing fins, they can only produce a limited roll stabilizing moment.

1.3 The Surface Effect Ship

1.3.1 Concept

This section is based on Butler (1985), Faltinsen (2005) and Auestad (2015).

A Surface effect ship (SES) is a marine craft with catamaran hull, equipped with flexible seal systems at the bow and stern. Hence, an air cushion occurs for the enclosed volume between the hull, seals and water plane as seen from Figure 1.9. This cushion may be pressurized by utilizing lift fans, which supplies the air cushion with a volumetric air inflow. A SES is also equipped with variable vent valves, in order to control the volumetric air outflow from the cushion. Hence, the vent valves can be utilized to control the air cushion pressure. Figure 1.9 and 1.10 illustrates a simplified SES setup. The air cushion, where the pressure are $P_a + P_c$, i.e. total cushion pressure, is enclosed by the catamaran side hulls, aft bag, finger skirt and water line. The air inflow and outflow denote the lift fans and vent valves, respectively.

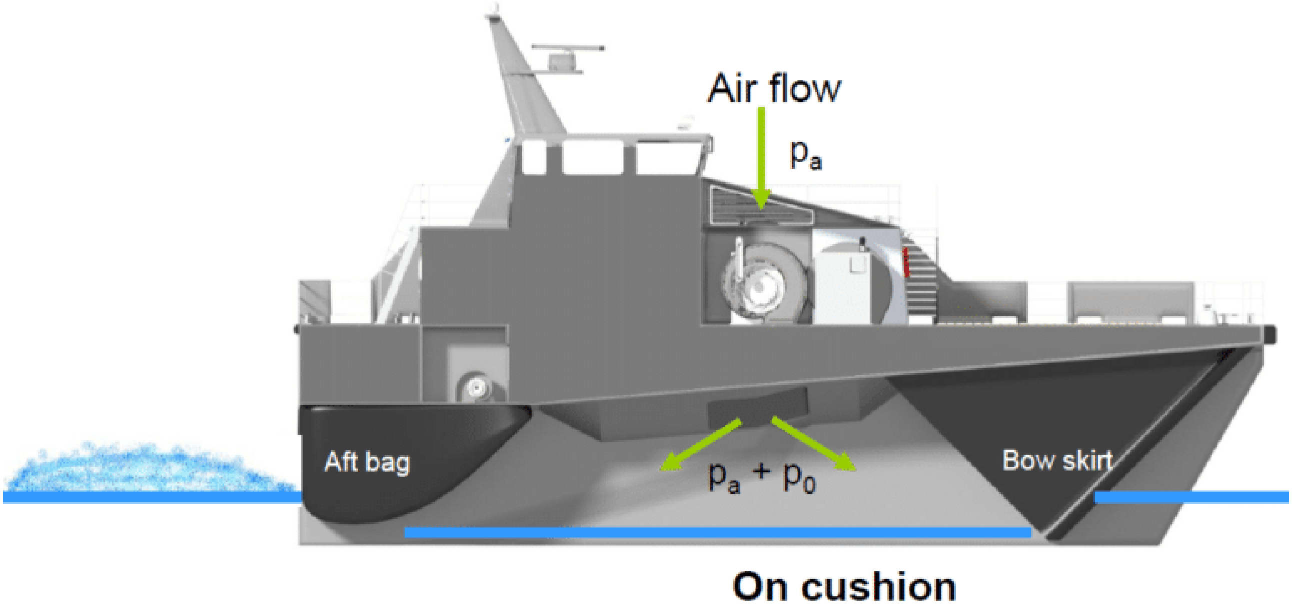

Figure 1.9: SES concept (Courtesy of Umoe Mandal)

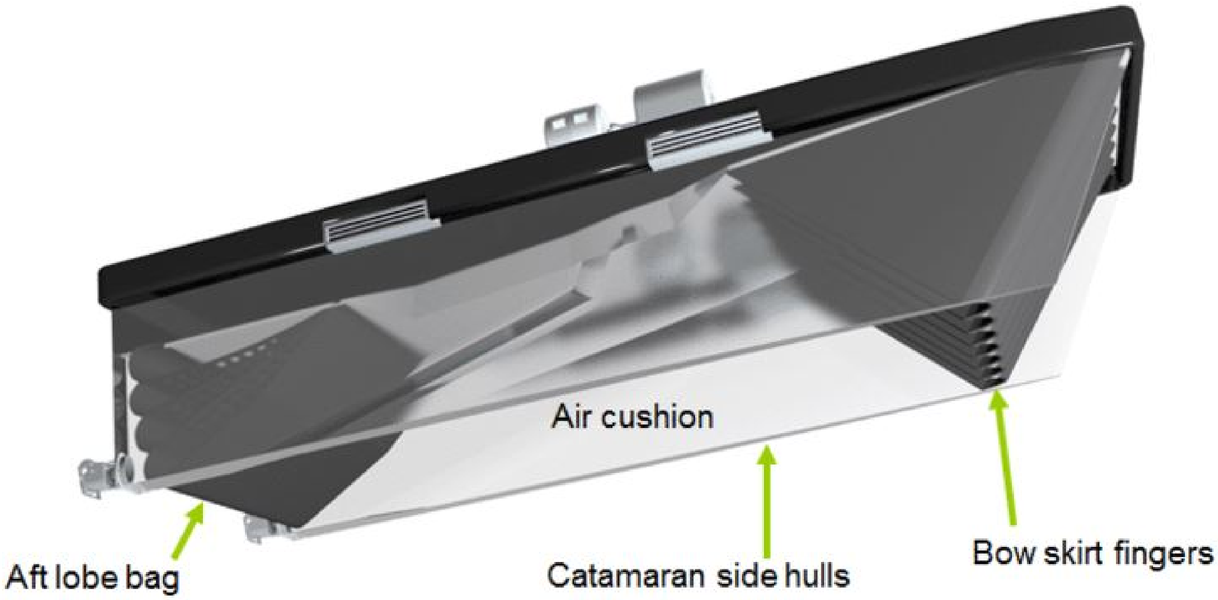

Figure 1.10: SES aircushion (Courtesy of Umoe Mandal)

Air Cushion Dimensions

The air cushion dimensions have a major influence on the size and proportions of a SES. The area of the air cushion and the lift fans characteristics determine how much weight the cushion can carry. An air cushion with low length-to-beam ratio (l/b ratio) has better stability abilities than an cushion with high l/b ratio. On the other side, a vessel with high l/b ratio is better suited for high-speed applications. The height of the air cushion is a trade-off between how large sea states the vessel is going to operate in and the transverse stability of the vessel. Generally, an air cushion with greater height decreases the metacentric height, which reduce the transverse stability. However, a SES with an air cushion with greater height is able to operate in heavier sea states (Butler, 1985).

Lift Fans and Vent Valves

The air cushion pressure is caused by lift fans and controlled by varying the leakage areas of the vent valves. A typical air fan system is shown in Figure 1.11, while the vent valve system that is exploited for the Wave Craft is shown in Figure 1.12. The cushion pressure induce a vertical force, lifting the vessel up from the water which reduces the water resistance acting on the hull. Typically, for SES, the cushion is able to carry 80 % of its weight, reducing the hydrostatic and hydrodynamic forces acting on the hull significantly and makes SES beneficial for high speed applications (Butler, 1985). When the vessel is operating at zero speed, the hydrostatic vertical buoyancy forces will carry the rest of the vessel (Faltinsen, 2005).

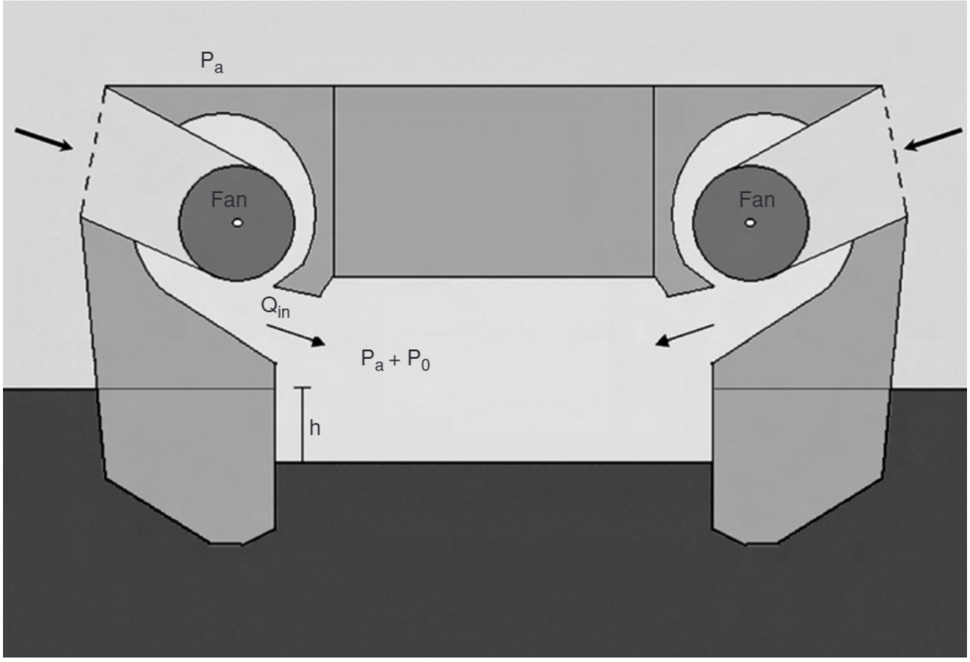

Figure 1.11: Front-view of catamaran hull including the air fan system (Faltinsen, 2005)

Figure 1.12: Hydraulic actuated vent valve system for the Wave Craft (Courtesy of Umoe Mandal) (Auestad, 2015)

Finger Skirt and Aft Bag

The purpose of the finger skirt and aft bag is to retain the air cushion fixed between the side hulls and the seals (finger skirt and aft bag). In addition, they provide low drag and better stability abilities (Butler, 1985). The aft bag, shown in Figure 1.13, is often a flexible bag consisting of 3 lobes, which are open against the side hulls. The aft bag booster fan ensures that the bag is pressurized and leakages do not occur under the bag. The finger skirt, shown in Figure 1.14, consists of a row of vertical loops in flexible material (Faltinsen, 2005).

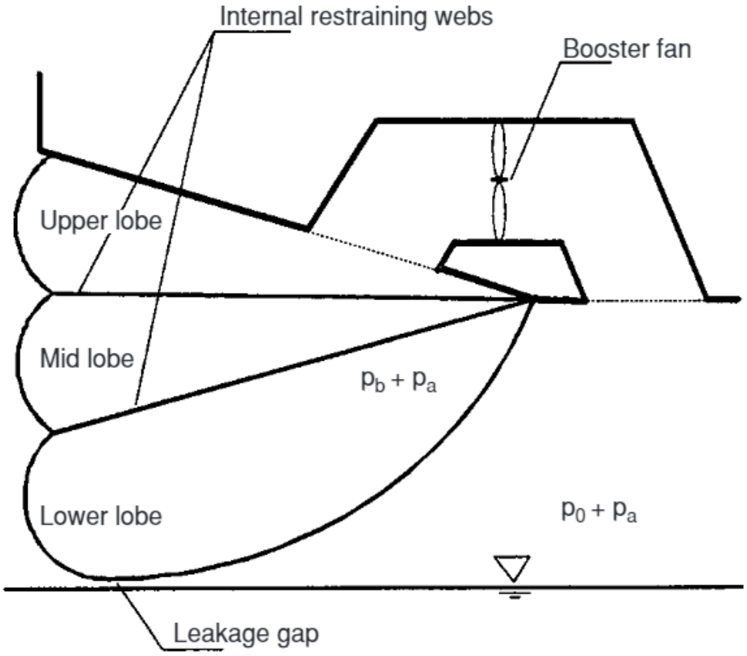

Figure 1.13: Aft bag and bag booster fan (Faltinsen, 2005)

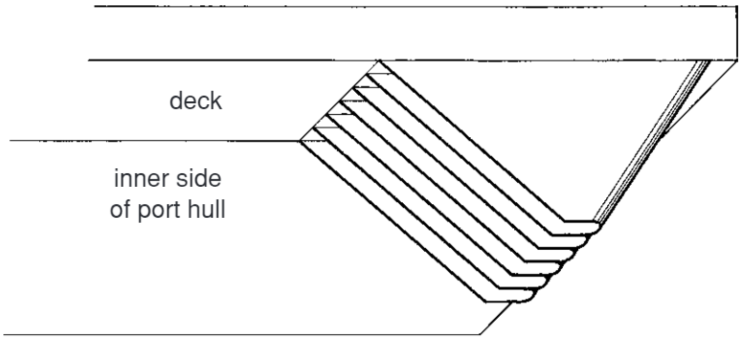

Figure 1.14: Finger skirt (Faltinsen, 2005)

Operating Modes

Typically, a SES is operating between two extreme modes; hull- and cushionborne. Usually, the lift ratio is controlled from 0 to 100 % to optimize performance depending on the application. Hullborne, or off-cushion, occurs when the lift and bag fan are turned off. Cushionborne, or on-cushion, occurs when the lift and bag fan are turned on and the vent valves are fully closed, i.e. the air cushion is subject to the maximum cushion pressure achievable. A hullborne mode for the Wave Craft is illustrated in Figure 1.15, while a cushionborne mode is shown in Figure 1.16. The roll damping control system developed in this project, and other motion damping control systems, are operating between these two extreme modes, hence they are partially cushionborne. In most cases, a SES is able to change between these two extreme modes in a couple of seconds.

Several benefits are related to dual mode operations. When hullborne, the SES is operating as a catamaran where the side hulls are fully displaced. Both in hullborne and partially cushionborne, the seals ensure that the air cushion volume acts like a passive motion damping accumulator which reduce large motions significantly (Butler, 1985). Another great advantage with operating both hull- and cushionborne is that the side hulls can be optimized for low speed resistance, since the SES operates cushionborne at high speeds. A monohull must be effective at both low and moderate speeds, i.e. the design of the hull is a trade-off between efficiency at different speeds.

Figure 1.15: Hullborne operation (Auestad, 2015)

Figure 1.16: Cushionborne operation (Auestad, 2015)

The SES offers the following characteristics:

- Shallow draft
- Fewer wave-induced forces on the hull
- Damping effect from vertical motion control system ensures a smooth ride
- In a seaway the vessel behaves more like a much larger vessel
- Reduced hull friction as vessel is “lifted” up from the water, resulting in very high-speed from generated by the conventional main propulsion system, and hence, ensuring low fuel consumption (litre / nm)
- High efficiencies deliver reduced environmental impact

1.3.2 History

The following section is mainly based on Butler (1985) and Lavis (1998). A brief overview of the most important SES designs and SES development through the history is presented. The development from the mid-90s until today is based on Auestad (2015).

Allen Ford invented the surface effect ship in 1960. Since 1961, over 50 SES designs have been built as test crafts or prototypes that have led to production. The historical evolution prior 1985, when Butler published his paper, can conveniently be divided into three distinct periods.

The first period started when the XR-1 followed by the XR-2, XR-3, 100A and 100B was built. These SESs were designed with low l/b ratios and thin side hulls. They were intended for high-speed operations, operating exclusively cushionborne. Therefore, they were well suited for missions such as high-speed passenger ferries. The 100A and 100B, shown in Figure 1.17, were both operational from 1972 to 1982. They reached top speeds of 80 and 94 knots, respectively.

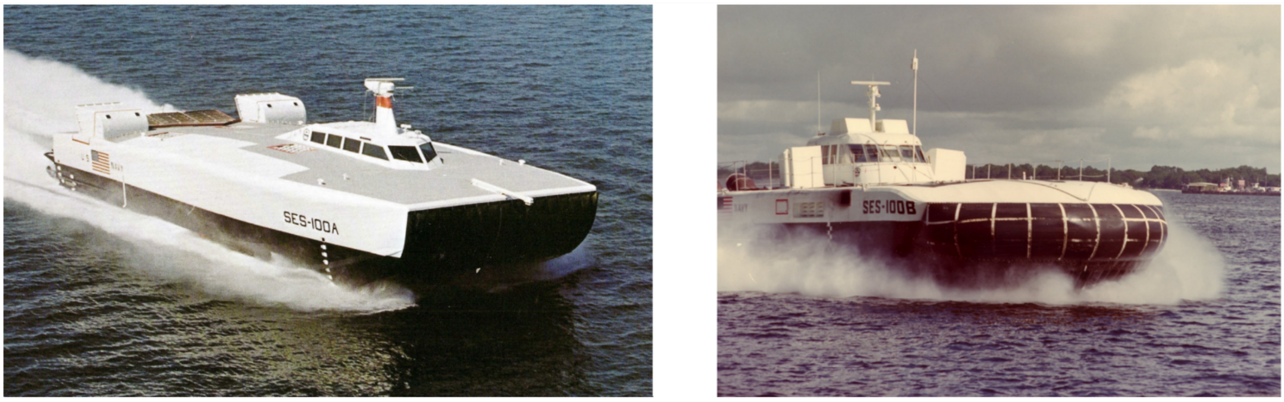

Figure 1.17: SES-100A and SES-100B, left and right figure, respectively (Auestad, 2015)

The second generation of the surface effect ship was designed with high l/b ratio. The USN XR-5 and multiple russian designs belong to this generation. These were designed for operations that did not require higher speeds than 50 to 60 knots for 100- to 1000-tons SESs.

The Russians have found these SESs very efficient for river transport due to their low-speed drag characteristics, and being able to stop by simply nudging the bow into the river bank.

The third generation of the surface effect ship is well described by the XR-5A and BH-110. The vital modification for these SESs, compared to the prior ones, was the shape of the catamaran side hulls. The new design led to a greater buoyancy force acting on the hull. Consequently, these SESs floated like a true catamaran in hullborne mode. This modification was included in the majority of new U.S. Navy SES designs, and made them efficient both at low and high speed. In 1982, NAVSEA produced the SES-200, shown in Figure 1.18, which was almost the same as the BH-110, but with increased length to beam ratio.

Figure 1.18: U.S. Navy's SES-200 (Lavis, 1998).

When Butler (1985) was published, the US Navy Minesweeper Hunter (MSH), shown in Figure 1.19, was the state of the art SES. The air cushion partly lifts the hull out off the water, thus making it less susceptible to underwater shock from mine explosions. The air cushion also makes it less likely that today's sophisticated mines will be triggered before they can be detected and neutralized.

Figure 1.19: U.S Navy Minesweeper Hunter (Courtesy of the US Navy.

Through the 80s and 90s, commercial SES ferries were dominating, due to their high speed and comfort. The Cirrus series, developed by Cirrus in cooperation with Brødrene Aa Batbyggeri A/S, were developed for this period. Brødrene Aa later joined the Ulstein group and built the luxury passenger ferry, UT904, shown in Figure 1.20.

Figure 1.20: Ulstein Group UT904 Luxury SES Passenger Ferry (Lavis, 1998)

In later years, new SES designs have mainly been developed in Europe. In the United States, only six new air cushion vehicles (ACVs) designs, of a certain size, have been built since 1980. According to Auestad (2015), operational SES has only been launched by Umoe Mandal since the mid-90s and up to this date. Umoe Mandal developed the Missile Torpedo Boat(MTB) Skjold in 1999, which has a maximum speed of 60+ knots and overall extreme performance. Early in 2015, Umoe delivered the Wave Craft prototype, which was designed for the commercial market (Auestad, 2015).

1.3.3 Air Cushion Control Systems

The following section is based on Sørensen and Egeland (1995), Adams et al. (1983) and Auestad (2015).

Ride Control System (RCS)

The ride control system is exploited to reduce wave-induced pressure fluctuations in the air cushion during transit. This will make the ride smoother and more comfortable. The main motivation behind the development is conveniently described by the citation

> *"Surface effect ships are known to offer a high quality ride in heavy sea states compared to conventional catamarans. However, in low and moderate sea states there are problems with discomfort owing to high frequency vertical accelerations induced by resonances in the pressurized air cushion."*
>
> Sørensen and Egeland (1995)

The main purpose of the developed RCSs are lowering vertical accelerations during moderate to high vessel speed. Three papers has gained high acknowledgment in the literature. The first by Kaplan and Davis (1978), the second one byAdams et al. (1983) and the third by Sørensen and Egeland (1995). MDI (Adams) og andre aktører utviklet operasjonelle RCS lenge før det ble skrevet om i litteraturen. Maritime Dynamics(MDI) and other actors developed RCSs long before these papers were published, and MDI became a leading actor as they provided the RCS that worked best and had the greatest commercial success. MDI also developed the first digital RCS. Initially, this system was implemented on the SES-200, and in 1982 installed and tested on the XR-1E (Adams et al., 1983).

According to Sørensen and Egeland (1995), previous RCSs have been based on the coupled equations of motion in heave and pitch derived by Kaplan and Davis (1978). "Their work was based on the assumption that the major part of the wave-induced loads from the sea was imparted to the craft as dynamic uniform air pressure acting on the wetdeck, while a minor part of the wave-induced loads from the sea was imparted to the craft as dynamic water pressure acting on the side hulls" (Sørensen and Egeland, 1995). Sørensen and Egeland (1995) extended this work by including the effect of spatial pressure variations in the air cushion which was demonstrated to give rise to significant vertical vibrations in high speeds.

Boarding Control System (BCS)

The most recent development of air cushion control systems is the BCS. As the RCS aims to keeps a constant air cushion pressure, the BCS does quite the opposite by altering the pressure to counteract, or compensate for, motion set up by sea waves.

developed by Auestad (2015). As the RCS aims for applications where the vessel has a moderate forward speed, the BCS is meant for reducing vertical motions in zero and low-speed operations.

The following feedback controller is implemented

$$u(t) = -ky(t) = -k\boldsymbol{C}\boldsymbol{x}(t) \tag{1.1}$$

where k is the scalar feedback controller gain and $y(t)$ is the measurement signal from combining two accelerometer signals as shown in figure 1.21a. The accelerometers are located in point C and above point B shown in figure 1.21b.

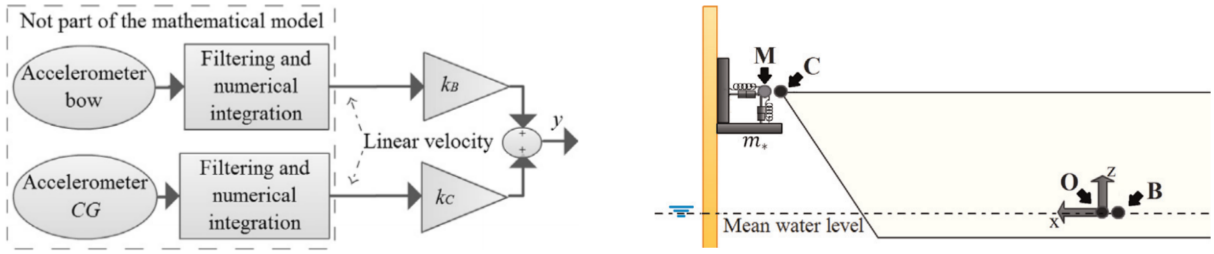

(a) Measurement signal y. (b) Vessel with no turbine contact.

Figure 1.21: Feedback signals for the BCS (Auestad, 2015).

This control law injects damping into the system as it is proportional to the vertical motion rate, and will manipulate the cushion pressure by adjusting the leakage areas to counteract and reduce vertical motions. Model test results indicate safer turbine access in up to 3.2 meter wave height for regular waves and 2.5 meter significant wave height for irregular waves.

1.3.4 The Wave Craft Series

This chapter is based on information from Umoe (2017) and gives an overview of the current state of Umoe Mandals Wave Craft series. One of these vessels is shown in Figure 1.22.

Figure 1.22: A Wave Craft vessel operating on an offshore windfarm. (Courtesy of Umoe Mandal)

The Wave Craft series currently offers vessels for renewables, oil & gas and defense. The following sections will give an overview of the current vessels for these operating areas.

Renewable

There are currently two types of crafts for the offshore wind industry in the Wave Craft series; the Commander and the Sprinter series. The Commander vessel series shown in Figure 1.23, is a highly-sophisticated class of composite vessels specifically designed for the medium to long-range transportation of personnel to offshore wind farms. Commander crafts are designed to operate at almost twice the speed and wave height of other equivalent vessels on the market.

Figure 1.23: Commander (Courtesy of Umoe Mandal)

The Sprinter vessel series shown in Figure 1.24 is designed to be a lightweight and cheaper vessel compared to Commander but has slightly less performance.

Figure 1.24: Sprinter (Courtesy of Umoe Mandal)

Both series are equipped with a vertical motion damping system that consists of two fully-automatic sub-modes: Boarding Control System (BCS) and Ride Control System (RCS) which are described in Section 1.3.3. The two modes are easily switched between on the operator interface touchscreen according to required operating mode, either Transit or Boarding.

Oil & Gas

For the oil & gas sector Umoe has designed the Voyager series, shown in Figure 1.25. This is a new generation service vessel, ideally designed for high-speed transfer of crew for the oil & gas industry. It is referred to as the seaborne helicopter, due to its ability to replace a helicopter in a lot of scenarios. These vessels can deliver offshore personnel to their installations safely and comfortably with a maximum speed of up to 58 knots. These vessels utilize the RCS for comfortable transit.

Figure 1.25: Voyager (Courtesy of Umoe Mandal)

Defense

There are two vessels of the defense series, the first being the Defender SOI (Special Operations Interceptor) shown in Figure 1.26. This vessel is designed to provide mission support with high-speed insertion and extraction in mind.

Figure 1.26: Defender SOI (Courtesy of Umoe Mandal)

The second is currently a concept, the Defender MCMV(Mine Counter-Measure) Drone shown in Figure 1.27. It would be constructed to lower risk and increase efficiency for unmanned naval missions.
Compared to a similar sized traditional mono-hull vessel, the protective air-cushion layer around the hulls, would enable the vessel to withstand significantly more shockwave impact from underwater explosions.

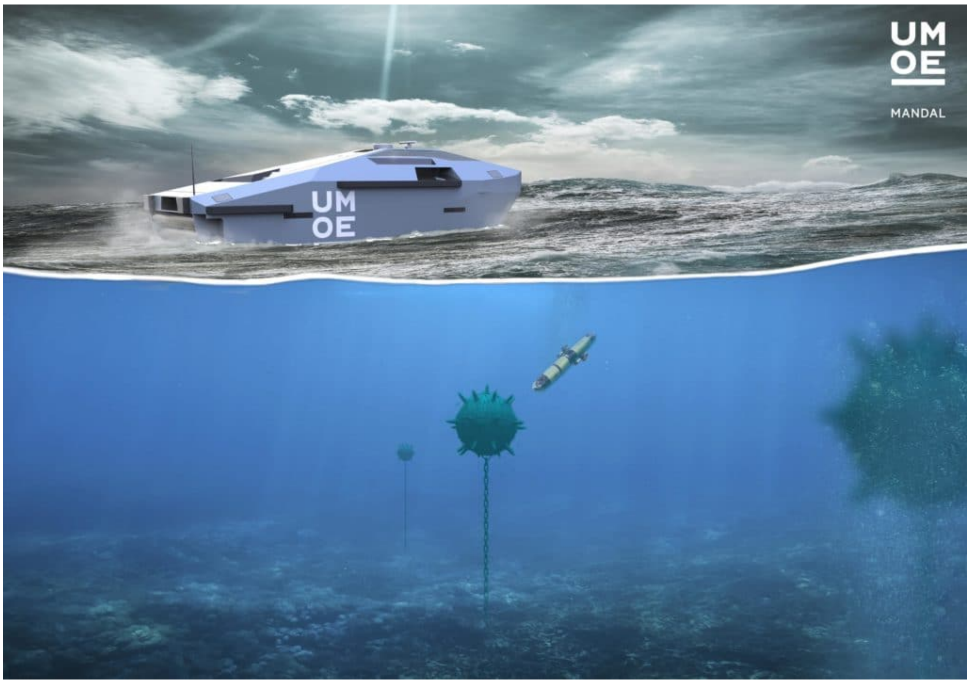

Figure 1.27: Defender MCMV Drone (Courtesy of Umoe Mandal)

Chapter 2

Mathematical Model

In mathematical modeling of marine craft dynamics it is common to divide the total motion into one low-frequency (LF) component and one wave-frequency (WF) component, where the LF component represents the dynamics of the vessel when exposed to second-order wave loads and other environmental forces and the WF component represents the dynamics of the vessel due to the first-order wave load (Sørensen, 2013). Hence, the total motion is the sum of the LF and WF components as shown in Figure 2.1.

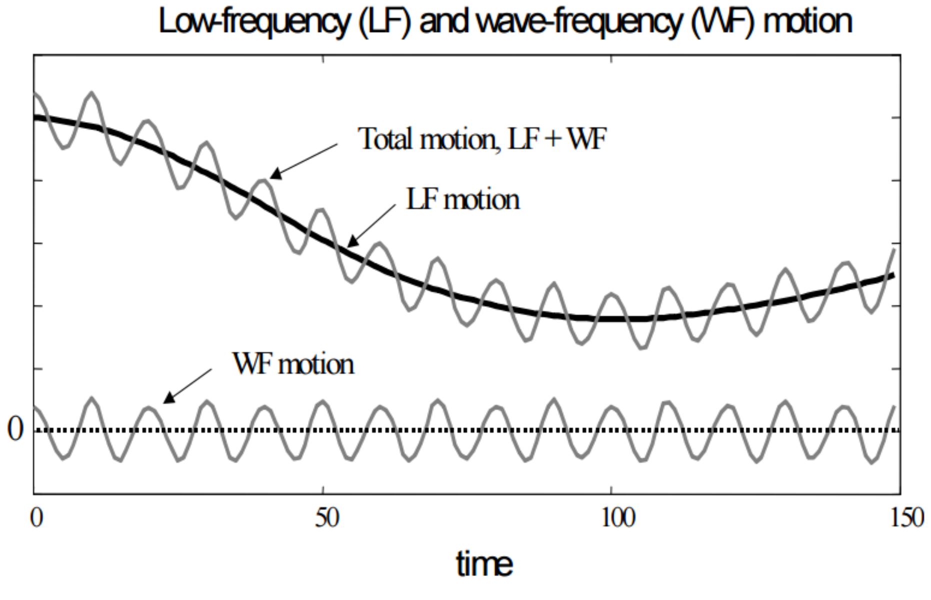

Figure 2.1: Low and wave frequency motions of a marine craft (Sørensen, 2013)

In Dynamic Position (DP) applications, only the LF component is fed back to the controller, since the high frequency WF component will lead to wear and tear on the actuators of the vessel. However, when designing a control system for a SES, damping of vessel motions due to first-order loads are of interest, hence the WF components are fed back to the controller. In the control plant model (CPM), which is a simplified model of the process plant model (PPM) used for control purposes, only the WF component is used (Sørensen, 2013).
The WF component can be well represented by a linear model when assuming small waves

and amplitudes of motion. For vessels that operate around zero speed, Coriolis and centrifugal terms are neglected. The motion of the vessel when exposed to first-order wave loads can be formulated as a frequency dependent mass damper spring system according to Fossen (2011)

$$[\mathbf{M}_{RB} + \mathbf{A}(\omega)]\ddot{\boldsymbol{\xi}} + \mathbf{B}(\omega)\dot{\boldsymbol{\xi}} + \mathbf{C}\boldsymbol{\xi} = \mathbf{f}cos(\omega t), \tag{2.1}$$

where $\mathbf{M}_{RB} \in \mathbb{R}^{6x6}$ is the inertia matrix, $\mathbf{A}(\omega) \in \mathbb{R}^{6x6}$ is the frequency dependent added mass matrix, $\mathbf{B}(\omega) \in \mathbb{R}^{6x6}$ is the potential damping matrix, $\mathbf{C} \in \mathbb{R}^{6x6}$ is the linearized restoring coefficient matrix due to gravity and buoyancy and $\mathbf{f} \in \mathbb{R}^{6x1}$ is the wave excitation amplitude vector. $\boldsymbol{\xi} \in \mathbb{R}^{6x1}$ is the WF state vector in the hydrodynamic frame, containing position and orientation. The hydrodynamic frame is illustrated in Figure 2.2.

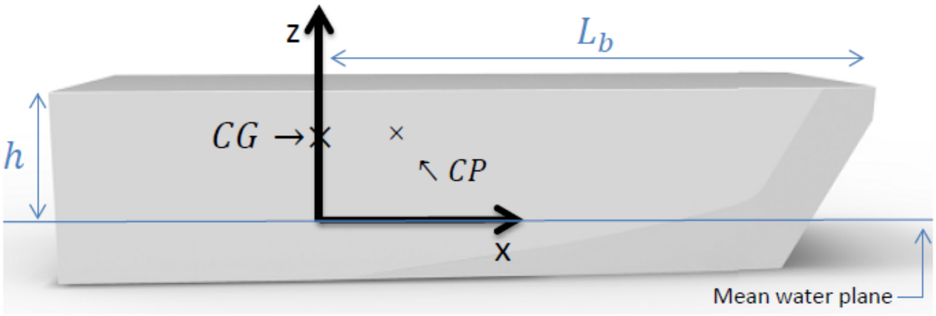

Figure 2.2: Hydrodynamic frame (Auestad, 2015)

The origin of the hydrodynamic frame is located at the mean water plane below the center of gravity (CG), and thereby follows the path of the vessel. The figure implies that the x, y and z axes are defined positive forward, to the port and upwards, respectively. Note that the y and z axes are usually defined positive to the starboard and downwards, respectively, for the hydrodynamic frame (Sørensen, 2013). The center of pressure (CP) denotes the attacking point for the pressure and is located a transverse and longitudinally distance from CG, enabling motion control for roll and pitch, respectively. $\eta_1(t)$, $\eta_2(t)$ and $\eta_3(t)$ represent the surge, sway and heave displacement which respectively is the translation along the x, y and z axis. $\eta_4(t)$, $\eta_5(t)$ and $\eta_6(t)$ denote the roll, pitch and yaw angle which is rotation around the x, y and z axis, respectively. $\dot{\eta}_i(t)$ for $i = 1, 2, .., 6$ denotes the corresponding rates for these DOFs. Positive translation and rotation are defined according to the right hand rule. The equations of motion (EOMs) for the control plant model is expressed in the hydrodynamic frame.

As discussed in Tønnessen (2016), the air cushion is split longitudinally along the center-line by exploiting a flexible separating wall design as shown in Figure 2.3. This is done in order to actively damp roll motions, exclusively by using the starboard and port air cushion pressure. The wall is flexible and pressurized by the aft bag fan, and thereby able to move to some extent, inducing time-varying cushion variables. These variables highly affect the maximum achievable roll control moment, which is used to counteract roll motions induced by waves. The air cushion variables are shown in figure 2.3 and defined in the next section.

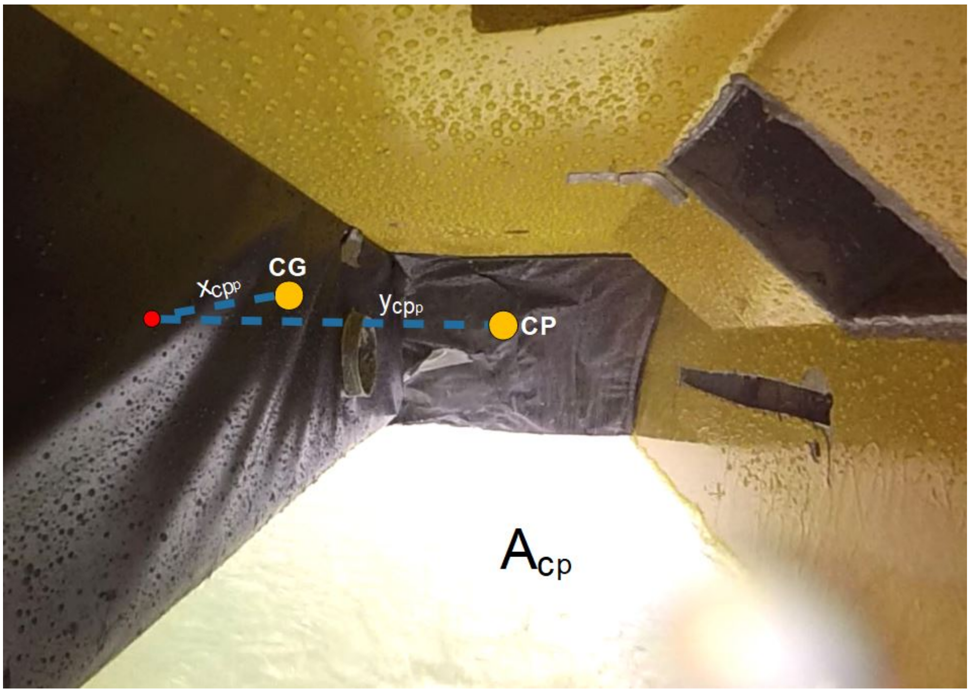

Figure 2.3: Port air cushion from Garmin camera view

2.1 Control Plant Model

A linear 3 DOF control plant model (CPM), including the starboard and port pressure dynamics, is developed for the Wave Craft. It is a simplified mathematical model, containing less dynamics than the more sophisticated process plant model (PPM). The CPM is exploited for control purposes, observer design and stability investigation. Each model form the basis for a simulator, which is able to supply simulations of the Wave Craft behaviour for multiple environmental conditions. In order to validate their accuracy, their response is compared to the corresponding model test response in Section 6. The CPM developed in this section is based on Tønnessen (2016).

2.1.1 Linearized Pressure Dynamics

For the CPM the starboard and port air cushion pressures are assumed uniform, while the air cushion areas are assumed to be constant. Hence, the center of pressure (CP) for both cushions will be located a longitudinally and transverse distance from the center of gravity (CG). Therefore, the longitudinally lever arms between CG and CP will coincide for both cushions, while the transverse lever arms will be opposite with same magnitude. These lever arms enable motion control of pitch and roll, respectively. The air cushion areas and the lever arms denote the air cushion variables for the CPM.

In the following, differential equations for the uniform cushion pressures are derived. The modeling is based on Auestad (2015). The starboard and port air cushion pressures are denoted $p_i(t) = p_a + p_{u_i}(t)$ for $i = \{s, p\}$, where p_a and $p_{u_i}(t)$ are the atmospheric pressure and the excess air cushion pressures, respectively. s and p denote starboard and port, respectively. The air cushion pressure dynamics are linearized about an equilibrium pressure, p_0, which occurs for constant lift fan frequencies, constant vent valve leakage areas and in absence of waves. p_0 is assumed equal for both cushions, i.e. two identical lift fans and vent valves are implemented. A uniform, non-dimensional cushion pressure variation parameter is defined according to

$$\mu_{u_i}(t) = \frac{p_{u_i}(t) - p_0}{p_0} \quad \text{for} \quad i = \{s, p\}. \tag{2.2}$$

The volumetric air flows into the air cushions, Q_{in_i}, are approximated by the fan characteristic curve which is a function of air cushion pressure, while the volumetric air flow outs of the cushions are written

$$Q_{out_i}(t) = c_n A_{L_i}(t) \sqrt{\frac{2p_i(t)}{\rho_a}} \quad \text{for} \quad i = \{s, p\}, \tag{2.3}$$

where c_n is a vent valve coefficient determining the local shape of the vent valve. $A_{L_s}(t)$ and $A_{L_p}(t)$ denote the total starboard and port cushion leakage area, respectively. These parameters include leakages under the side hulls, separating wall, seals and also through the controllable vent valves. The total leakage areas are written

$$A_{L_i}(t) = A_i^{hull}(t) + A_i^{wall}(t) + A_i^{seals}(t) + A_i^{ctrl}(t) \quad \text{for} \quad i = \{s, p\}, \tag{2.4}$$

where $A_s^{ctrl}(t)$ and $A_p^{ctrl}(t)$ are the variable leakage areas for the starboard and port vent valve, respectively. These variables are defined as

$$A_i^{ctrl}(t) = A_0^{ctrl} + \Delta A_i^{ctrl}(t) \quad \text{for} \quad i = \{s, p\}, \tag{2.5}$$

where A_0^{ctrl} represents a mean operating value or bias opening, that allows two sided control. $\Delta A_s^{ctrl}(t)$ and $\Delta A_p^{ctrl}(t)$ denote controllable leakage area for the starboard and port air cushion, respectively.

The uniform pressure equations are inspired by the work of Sørensen and Egeland (1995) and Auestad (2015). A model for the starboard and port air cushion pressure dynamics are expressed in the hydrodynamic frame according to

$$\begin{aligned} &K_1 \dot{\mu}_{u_i}(t) + K_3 \mu_{u_i}(t) + \rho_{c0} A_c \dot{\eta}_3(t) \mp \rho_{c0} A_c y_{cp} \dot{\eta}_4(t) - \rho_{c0} A_c x_{cp} \dot{\eta}_5(t) \\ &= K_2 \Delta A_i^{ctrl}(t) + \rho_{c0} \dot{V}_{0_i}(t) \quad \text{for} \quad i = \{s, p\}, \end{aligned} \tag{2.6}$$

where

$$
\begin{aligned}
K_1 &= \frac{\rho_{c0} h_0 A_c}{\gamma\left(1 + \frac{p_a}{p_0}\right)} \\
K_2 &= \rho_{c0} c_n \sqrt{\frac{2p_0}{\rho_a}} \\
K_3 &= \frac{\rho_{c0}}{2}\left(Q_0 - 2p_0 q \frac{\partial Q_{in}}{\partial P} \mid_0 \right).
\end{aligned}
\tag{2.7}
$$

ρ_a and ρ_{c0} denote the air densities at the atmospheric pressure p_a and equilibrium pressure p_0, respectively. A_c is the air cushion area and x_{cp} and y_{cp} are the longitudinal and transverse distances between CG and CP, respectively. Q_0 is the equilibrium air flow for the equilibrium pressure and $\frac{\partial Q_{in}}{\partial P} \mid_0$ is the linearized lift fan characteristic slope at the equilibrium point, (p_0, Q_0). γ is the ratio of specific heat for air. The parameter q denotes the number of lift fans that are running at same frequency. h_0 is the height of the air cushion. $\dot{V}_{0_i}(t)$ is denoted wave volume pumping in the literature and represents the rate of change of volume inside the cushion due to waves (Faltinsen, 2005). This parameter is defined later. Note that $\mp$ in equation (2.6) and for the remaining equations denotes minus for starboard and plus for port.

The equation implies that growing air cushion pressures will induce positive heave motion along the body-fixed z-axis and negative pitch motion (CW) around the body-fixed y-axis. This holds for both pressures. The starboard and port air cushion pressure will affect roll motion opposite; an increase in port pressure will induce positive roll motion (CCW), while an increase in starboard cushion pressure will induce negative roll motion (CW).

2.1.2 Wave Craft Control Plant Model

A differential equation for roll, dependent on the starboard and port cushion pressures, is written

$$
(I_{44} + A_{44})\ddot{\eta}_4(t) + B_{44}\dot{\eta}_4(t) + C_{44}\eta_4(t) + y_{cp}A_c p_0 \mu_{u_s}(t) - y_{cp}A_c p_0 \mu_{u_p}(t) = F_4^e(t). \tag{2.8}
$$

The heave (2.9) and pitch (2.10) dynamics when utilizing a split cushion design is modeled as follows

$$
(m + A_{33})\ddot{\eta}_3(t) + B_{33}\dot{\eta}_3(t) + C_{33}\eta_3(t) - A_c p_0 \mu_{u_s}(t) - A_c p_0 \mu_{u_p}(t) = F_3^e(t) \tag{2.9}
$$

$$
(I_{55} + A_{55})\ddot{\eta}_5(t) + B_{55}\dot{\eta}_5(t) + C_{55}\eta_5(t) + x_{cp}A_c p_0 \mu_{u_s}(t) + x_{cp}A_c p_0 \mu_{u_p}(t) = F_5^e(t), \tag{2.10}
$$

where A_{ii}, B_{ii} and C_{ii} represent the hydrodynamic added mass, potential damping and restoring coefficients for motion ii where $i = 3, 4, 5$ denote heave, roll and pitch, respectively. $F_e^i(t)$ is the hydrodynamic wave excitation forces for these DOFs. m is the mass of the vessel, while I_{44} and I_{55} represent the moment of inertia for roll and pitch, respectively. $\ddot{\eta}_i(t)$ and $\eta_i(t)$ are the

linear/angular acceleration and linear/angular displacement, respectively, for the DOFs. The hydrodynamics parameters were obtained from ShipX and Veres.
The control plant model is written as a LTI state-space model

$$\begin{aligned} \dot{\boldsymbol{x}}(t) &= \boldsymbol{A}\boldsymbol{x}(t) + \boldsymbol{B}\boldsymbol{u}(t) + \boldsymbol{E}\boldsymbol{w}(t) \\ \boldsymbol{y}(t) &= \boldsymbol{C}\boldsymbol{x}(t), \end{aligned} \tag{2.11}$$

where the state vector, $\boldsymbol{x}(t)$, is defined in Table 2.1. $\boldsymbol{u}(t) = \begin{bmatrix} \Delta A_s^{ctrl}(t) & \Delta A_p^{ctrl}(t) \end{bmatrix}^\top$, $\boldsymbol{w}(t) = \begin{bmatrix} F_3^e(t) & F_4^e(t) & F_5^e(t) & \dot{V}_{0_s}(t) & \dot{V}_{0_p}(t) \end{bmatrix}^\top$ and
$\boldsymbol{y}(t) = \begin{bmatrix} \eta_4(t) & \eta_5(t) & \dot{\eta}_3(t) & \dot{\eta}_4(t) & \dot{\eta}_5(t) & p_s(t) & p_p(t) \end{bmatrix}^\top$ are the input, disturbance and measurement vector, respectively.

Table 2.1: Control plant model states

State	Description	Notation
$x_1(t)$	Heave displacement	$\eta_3(t)$
$x_2(t)$	Roll angle	$\eta_4(t)$
$x_3(t)$	Pitch angle	$\eta_5(t)$
$x_4(t)$	Heave linear momentum	$(m + A_{33})\dot{\eta}_3(t)$
$x_5(t)$	Roll angular momentum	$(I_{44} + A_{44})\dot{\eta}_4(t)$
$x_6(t)$	Pitch angular momentum	$(I_{55} + A_{55})\dot{\eta}_5(t)$
$x_7(t)$	Dynamic starboard cushion pressure	$\mu_{u_s}(t)$
$x_8(t)$	Dynamic port cushion pressure	$\mu_{u_p}(t)$

The starboard and port pressure dynamics in (2.6) and the heave, roll and pitch dynamics in (2.9), (2.8) and (2.10), respectively, are included in the control plant model. The system is written in state-space form according to (2.11) where the system matrix, $\boldsymbol{A}$, the input matrix, $\boldsymbol{B}$, the measurement matrix, $\boldsymbol{C}$, and disturbance matrix, $\boldsymbol{E}$, are included in Appendix A.

2.2 Process Plant Model

A nonlinear 6 DOF process plant model for the Wave Craft is developed, both to validate the linear control plant model and to achieve more realistic simulation of the behaviour of the Wave Craft. This model is an extension to the work of Øyvind Auestad and Jørgen Rørvik at Umoe Mandal.

2.2.1 Nonlinear Pressure Dynamics

A nonlinear equation for the cushion pressures is developed. It is based on the continuity equation for air mass

$$\rho_a Q_{in_i}(t) - \rho_a Q_{out_i}(t) = \frac{d}{dt}\big(\rho_{c_i}(t)\Omega_i(t)\big) \quad \text{for} \quad i = \{s, p\} \tag{2.12}$$

and the relation between pressure and density, assuming ideal gas and adiabatic conditions

$$\frac{p_a + p_{u_i}(t)}{p_a + p_0} = \left(\frac{\rho_{c_i}(t)}{\rho_a}\right)^{\gamma} \quad \text{for} \quad i = \{s, p\}. \tag{2.13}$$

Here, $\Omega_i(t)$ and $\rho_{c_i}(t)$ are time-varying air cushion volumes and air densities inside the cushions, respectively. By using the chain rule, (2.12) is written

$$\rho_a Q_{in_i}(t) - \rho_a Q_{out_i}(t) = \dot{\rho}_{c_i}(t)\Omega_i(t) + \rho_{c_i}(t)\dot{\Omega}_i(t) \quad \text{for} \quad i = \{s, p\}. \tag{2.14}$$

According to Auestad (2015) the enclosed air cushion volumes, $\Omega_i(t)$, which are numerically calculated using a 3D model of the vessel, are expressed

$$\Omega_i(t) = \iint_{A_{c_i}} \Big(h_{c_i}(x, y) + \eta_3(t) + y_{cp_i}\eta_4(t) + x_{cp_i}\eta_5(t) - T_i(t) - \zeta_i(x, y, t)\Big)\, dA \quad \text{for} \quad i = \{s, p\}, \tag{2.15}$$

where $h_{c_i}(x, y)$ are the spatial varying heights from the baseline to the wet deck, $T_i(t)$ are the draughts and $\zeta_i(x, y, t)$ denotes the spatial and time varying wave elevations. Inspired by Sørensen (2013), the rate of change of the air cushion volumes is written

$$\dot{\Omega}_i(t) = A_{c_i}(t)\Big(\dot{\eta}_3(t) + y_{cp_i}\dot{\eta}_4(t) - x_{cp_i}\dot{\eta}_5(t)\Big) - \dot{V}_{0_i}(t) \quad \text{for} \quad i = \{s, p\}. \tag{2.16}$$

An equation for wave volume pumping, $\dot{V}_{0_i}(t)$, is developed for the general case of various headings. $\dot{V}_{0_i}(t)$ denotes the rate of change of the air cushion volumes due to waves. $V_{0_i}(t)$, represents the volume occupied by waves inside the air cushions. These parameters are calculated by integrating the wave elevation, $\zeta(x, y, t)$, and rate of change of the wave elevation, $\dot{\zeta}(x, y, t)$, longitudinally and transversely along the air cushions according to

$$V_{0_i}(t) = \int_{-W_i(t)/2}^{W_i(t)/2} \int_{-L_i(t)/2}^{L_i(t)/2} \zeta_i(x, y, t)\, dx\, dy \quad \text{for} \quad i = \{s, p\} \tag{2.17}$$

and

$$\dot{V}_{0_i}(t) = \int_{-W_i(t)/2}^{W_i(t)/2} \int_{-L_i(t)/2}^{L_i(t)/2} \dot{\zeta}_i(x, y, t)\, dx\, dy \quad \text{for} \quad i = \{s, p\}, \tag{2.18}$$

where $L_i(t)$ and $W_i(t)$ are the length and width of the air cushions, respectively. The wave elevation is defined by Perez (2005) according to

$$\zeta_i(x, y, t) = \bar{\zeta} \sin\Big(\omega t + \epsilon - k\big(x\cos(\chi) + y\sin(\chi)\big)\Big), \tag{2.19}$$

where $\bar{\zeta}$ is the constant wave amplitude, ω is the circular wave frequency, ϵ is the phase and χ is the direction the waves propagate with respect to the body frame, which makes the wave volume pumping valid for various wave directions. By differentiating the wave elevation with respect to time, the rate of change is found from

$$\dot{\zeta}(x,y,t) = \bar{\zeta}\omega\cos\Big(\omega t + \epsilon - k\big(x\cos(\chi) + y\sin(\chi)\big)\Big). \tag{2.20}$$

By solving (2.13) with respect to $\rho_c(t)$, an expression for the air densities inside the cushions is found to be

$$\rho_{c_i}(t) = \rho_a\left(\frac{p_a + p_{u_i}(t)}{p_a + p_0}\right)^{\frac{1}{\gamma}} \quad \text{for} \ \ i = \{s,p\}. \tag{2.21}$$

The rate of change of air mass densities inside the cushions, $\dot{\rho}_{c_i}(t)$, is calculated by differentiating (2.21) with respect to time

$$\dot{\rho}_{c_i}(t) = \frac{\rho_a}{\gamma(p_a + p_0)^{\frac{1}{\gamma}}}(p_a + p_{u_i}(t))^{\frac{1-\gamma}{\gamma}}\dot{p}_{u_i}(t) \quad \text{for} \ \ i = \{s,p\}. \tag{2.22}$$

The nonlinear air cushion pressure equation is derived by combining (2.14), (2.21) and (2.22)

$$\dot{p}_{u_i}(t) = \frac{\gamma}{\Omega_i(t)}\Big[(p_a + p_0)^{\frac{1}{\gamma}}\big(Q_{in_i}(t) - Q_{out_i}(t)\big)\big(p_a + p_{u_i}(t)\big)^{\frac{\gamma-1}{\gamma}} - \big(p_a + p_{u_i}(t)\big)\dot{\Omega}_i(t)\Big] \quad \text{for} \ \ i = \{s,p\} \tag{2.23}$$

2.2.2 Air Cushion Variables

In order to model the behaviour of the Wave Craft with greater accuracy when exposed to waves, the air cushion variables are modeled to vary with time for the Process Plant Model. The achievable pressure-induced control force and moments for heave, roll and pitch are highly dependent on air cushion areas and longitudinally and transverse lever arms, A_{c_i}, x_{cp_i} and y_{cp_i}, respectively. Hence, it is important that these variables are modeled as accurate as possible to obtain realistic simulations.

Air Cushion Areas

The area of the water line inside the starboard and port air cushion, A_{c_s} and A_{c_p}, respectively, are assumed rectangular for all heave displacements and roll and pitch angles. These areas are defined according to

$$A_{c_i}(t) = L_i(t) \cdot W_i(t) \quad \text{for} \ \ i = \{s,p\}. \tag{2.24}$$

The finger skirt and aft bag are located in positive and negative longitudinally distance, respectively, relative to CG. Hence, the length of the air cushions are modeled as

$$L_i(t) = x_{bow/CG_i}(t) - x_{bag/CG_i}(t) \quad \text{for} \ \ i = \{s,p\}. \tag{2.25}$$

The width of the air cushions, $W_i(t)$, is the distance from the separating wall to the side hulls. The separating wall is assumed to be vertical at all times, even when the hull is rolling, i.e. the width of the cushions are dependent on the roll angle. The width of the starboard and port air cushion, $W_s(t)$ and $W_p(t)$, respectively, are expressed in the hydrodynamic frame according to

$$W_i(t) = \mp y_{c_0} \mp \big(h_h - T_i(t)\big)\sin(\eta_4(t)) \ \text{ for } \ i = \{s, p\}, \tag{2.26}$$

where y_{c_0} is the width for $\eta_4(t) = 0$ and h_h is the distance from the baseline to the wet deck. The x-coordinate of the point the bow seal and aft bag coincide with the water line is modeled relative to CG in the hydrodynamic frame as follows

$$x_{bow/CG_i}(t) = x_{FP/CG} + \frac{T_i(t)}{\tan(\alpha)} \ \text{ for } \ i = \{s, p\} \tag{2.27}$$

$$x_{bag/CG_i}(t) = x_{AP/CG} + \frac{x_{bag}}{z_{bag}}T_i(t) \ \text{ for } \ i = \{s, p\}. \tag{2.28}$$

$x_{FP/CG}$ and $x_{AP/CG}$ are the longitudinally distance between FP and CG and AP and CG, respectively. $T_i(t)$ is the draught for the starboard and port cushion and $\alpha = 51°$ is the angle of the bow skirt. x_{bag} and z_{bag} represent the length and height of the aft bag, respectively. In order to derive an expression dependent on draught, the aft bag profile is approximated to be a triangle, and similarity forms are exploited to obtain the term $\frac{x_{bag}}{z_{bag}}T_i(t)$.

Draught

The time-varying draughts denote the part of the side hulls, inside the cushions, that are submerged. Since the starboard and port cushion are subject to different pressures, the draught is modeled individually for each chamber. It is oscillating around some mean operating value, $T_0(x)$, which appears for the static equilibrium pressure, p_0, and in absence of waves. Note that this parameter varies depending on longitudinally distance from CG. The reason for this is that the height of the hull increases towards the bow. Pitch motions may also be present, inducing different draught contributions which depend on the longitudinally distance to CG. The time-varying draughts, $T_i(t)$, are expressed according to

$$T_i(x,t) = T_0(x) - \left(\eta_3(t) - \frac{p_0 A_{c_i}(t)}{C_{33}}\right) - W_i(t)\sin\eta_4(t) + x\sin\eta_5(t) \ \text{ for } \ i = \{s, p\}, \tag{2.29}$$

where $\frac{p_0 A_{c_i}(t)}{C_{33}}$ is heave displacement compensation due to $T_0(x)$.

Longitudinally Lever Arm

The pressure inside the two chambers are assumed uniform, i.e. the center of pressure in both cushions are assumed to be located in their respective volume centers. In the hydrodynamic frame the longitudinally CP coordinate is located halfway between the bow skirt and stern bag for both cushions, i.e. the longitudinally lever arms are dependent on the positions of the bow seal and aft bag and thereby dependent on draught and pitch angle. Therefore, the longitudinally lever arms for the cushions are written

$$x_{cp_i}(t) = \frac{x_{bow/CG_i}(t) - x_{bag/CG_i}(t)}{2} \quad \text{for} \;\; i = \{s, p\}. \tag{2.30}$$

Transverse Lever Arm

In the hydrodynamic frame the transverse CP coordinate are located halfway between the separating wall and the side hull for both cushions, i.e. the transverse lever arms are defined in the hydrodynamic frame according to

$$y_{cp_i}(t) = \frac{W_i(t)}{2} \quad \text{for} \;\; i = \{s, p\}. \tag{2.31}$$

2.2.3 Wave Craft Process Plant Model

A process plant model including the pressure dynamics and cushion variables is developed for the Wave Craft. It is based on seakeeping theory, where it is assumed that the motion of a marine craft can be expressed as a superposition of an equilibrium state of motion plus perturbations. The equilibrium is determined by an constant heading and speed, $\bar{\psi}$ and U, respectively, and the perturbations are zero-mean oscillatory components induced by first-order wave excitations (Fossen, 2011). The PPM could be expressed in both the seakeeping frame and the body frame, where the seakeeping frame is not fixed to the marine craft, but to an equilibrium state. The body frame is fixed to the marine craft, the perturbations around the equilibrium state are therefore expressed by the position of the body frame relative to the seakeeping frame. Since it is intuitive to understand how forces and moments induce motion in the body frame, the PPM is expressed here. Most motion control systems are formulated in the body frame (Fossen, 2011). According to Fossen (2011), a 6 DOF seakeeping model for a marine craft expressed in the body frame, $\{b\}$, can be written

$$\dot{\boldsymbol{\eta}} = \mathbf{J}_{\Theta}(\boldsymbol{\eta})\boldsymbol{\nu} \tag{2.32}$$

$$\boldsymbol{M}\dot{\boldsymbol{\nu}} + \boldsymbol{C}_{RB}^{\star}\boldsymbol{\nu} + \boldsymbol{C}_{A}^{\star}\boldsymbol{\nu}_r + \boldsymbol{D}\boldsymbol{\nu}_r + \int_0^t \boldsymbol{K}(t-\tau)\delta\boldsymbol{\nu}\, d\tau + \boldsymbol{G}\boldsymbol{\eta} = \boldsymbol{\tau}_{exc}, \tag{2.33}$$

where $\boldsymbol{\eta}$ and $\boldsymbol{\nu}$ are the generalized position and velocity vectors used to describe motions in 6 DOF, respectively. $\boldsymbol{\nu}_r$ is the the relative velocity vector, taking ocean current into account. Equation (2.32) is the kinematics, where the transformation matrix, $\boldsymbol{J}_{\Theta}(\boldsymbol{\eta})$, which is dependent on the Euler angles, $\boldsymbol{\Theta}$, transforms the velocity vector in the body frame, $\boldsymbol{\nu}$, into the corresponding position derivative vector in the NED frame, $\dot{\boldsymbol{\eta}}$.

Equation (2.33) is the kinetics. Here, $\boldsymbol{M} = \boldsymbol{M}_{RB} + \boldsymbol{M}_A$, is the mass matrix. $\boldsymbol{M}_{RB}$ is the rigid-body matrix and $\boldsymbol{M}_A = \boldsymbol{A}(\infty)$ is the constant infinite-frequency added mass matrix. The linearized Coriolis-centripetal matrices due to rigid-body mass and hydrodynamic added mass, $\boldsymbol{C}^{\star}_{RB}$ and $\boldsymbol{C}^{\star}_{A}$, respectively, appear due to the transformation of the equations of motion from the seakeeping frame, $\{s\}$, which is considered inertial, to the rotating body frame, $\{b\}$. The total linear damping is written $\boldsymbol{D} = \boldsymbol{B}_{total}(\infty) = \boldsymbol{B}(\infty) + \boldsymbol{B}_V(\infty)$, where $\boldsymbol{B}(\infty)$ and $\boldsymbol{B}_V(\infty)$ are the potential and viscous damping matrices, respectively. The Wave Craft is operating at zero forward speed, hence the Coriolis-centripetal forces vanish.

> *"Due to the motion of the ship, waves are generated in the free surface. These waves will, in principle, persist in all subsequent times, affecting the motion of the ship. This is known as fluid memory effects."*
>
> ---
>
> Fossen (2011)

The fluid memory effects are caught in the convolution integral in (2.33) and is written

$$\boldsymbol{\mu} = \int_0^t \boldsymbol{K}(t-\tau)\delta\boldsymbol{\nu}\, d\tau. \tag{2.34}$$

Here, $\boldsymbol{K}(t)$ is a matrix of retardation functions and $\delta\boldsymbol{\nu} = \begin{bmatrix} \boldsymbol{v}^b_{b/s} \\ \boldsymbol{w}^b_{b/s} \end{bmatrix}$ is the seakeeping or perturbation velocity coordinates, representing the velocity perturbations of the body frame around the seekeaping frame. The matrix of retardation functions is according to Fossen (2011) written

$$\boldsymbol{K}(t) = \frac{2}{\pi}\int_0^\infty [\boldsymbol{B}_{total}(\omega) - \boldsymbol{B}_{total}(\infty)]\cos(\omega t)\, d\omega. \tag{2.35}$$

Equation (2.34), which contains the fluid memory effects, is derived from the work of Cummins (1962). Here, the radiation-induced hydrodynamic forces, $\boldsymbol{\tau}_{hyd}$, in an ideal fluid are related to frequency-dependent added mass and potential damping according to

$$\boldsymbol{\tau}_{hyd} = -\boldsymbol{A}(\infty)\ddot{\boldsymbol{\xi}} - \int_0^t \bar{\boldsymbol{K}}(t-\tau)\dot{\boldsymbol{\xi}}(\tau)\, d\tau. \tag{2.36}$$

This is known as Cummins equation. $\boldsymbol{\xi} = \delta\boldsymbol{\eta}$ and $\dot{\boldsymbol{\xi}} = \boldsymbol{\delta\nu}$ are seakeeping coordinates and $\bar{\boldsymbol{K}}(t)$ is a matrix of retardation functions given by

$$\bar{\boldsymbol{K}}(t) = \frac{2}{\pi}\int_0^\infty \boldsymbol{B}(\omega)\cos(\omega t)\, d\omega. \tag{2.37}$$

It makes sense to utilize (2.35) instead of (2.37) to represent the retardation function matrix. According to Fossen (2011) it is better to integrate the difference, since $\boldsymbol{B}_{total}(\omega) - \boldsymbol{B}_{total}(\infty)$

will be exact zero at $\omega = \infty$, and thereby not oscillate around some steady-state value, which (2.37) may do. When using (2.35) instead of (2.37), the additional damping term $\boldsymbol{B}_{total}(\infty)\boldsymbol{\nu}_r$ must be added to the equations of motion expressed in the body frame.

Kristiansen and Egeland (2003) and Kristiansen et al. (2005) have developed a state-space approximation for $\boldsymbol{\mu}$ using realization theory. If $\delta\boldsymbol{\nu}$ is a unit impulse, then (2.34) will be an impulse response function. Hence, $\boldsymbol{\mu}$ can be represented by a linear state-space model according to

$$\begin{aligned} \dot{\boldsymbol{\zeta}} &= \boldsymbol{A}_r\boldsymbol{\zeta} + \boldsymbol{B}_r\delta\boldsymbol{\nu} \\ \boldsymbol{\mu} &= \boldsymbol{C}_r\boldsymbol{\zeta} + \boldsymbol{D}_r\delta\boldsymbol{\nu}, \end{aligned} \tag{2.38}$$

where the matrices $\boldsymbol{A}_r$, $\boldsymbol{B}_r$, $\boldsymbol{C}_r$ and $\boldsymbol{D}_r$ are determined experimentally by Umoe Mandal and not included in this thesis.

$\boldsymbol{G} = \boldsymbol{C}$ is the hydrostatic gravity and buoyancy forces matrix, which tend to bring the ship to its equilibrium position. The external forces vector, $\boldsymbol{\tau}_{exc}$, may consist of several contributions like first- and second-order wave forces, wind forces, mooring forces, thruster forces and other kinds of control forces. The air cushion forces will also enter this vector and is in the body frame written

$$\boldsymbol{\tau}_{cushion} = \begin{bmatrix} 0 \\ 0 \\ -(A_{c_s}p_{u_s} + A_{c_p}p_{u_p}) \\ y_{cp_s}A_{c_s}p_{u_s} + y_{cp_p}A_{c_p}p_{u_p} \\ x_{cp_s}A_{c_s}p_{u_s} + x_{cp_p}A_{c_p}p_{u_p} \\ 0 \end{bmatrix}. \tag{2.39}$$

It is assumed that the cushion pressures only induce forces in the vertical plane. Forces for surge and sway and a yaw moment occur for various vent valves openings. This is not considered here. The process plant model expressed in the body frame for simulations of the Wave Craft behaviour is given by

$$\dot{\boldsymbol{\eta}} = \mathbf{J}_{\Theta}(\boldsymbol{\eta})\boldsymbol{\nu} \tag{2.40}$$

$$\big(\boldsymbol{M}_{RB} + \boldsymbol{A}(\infty)\big)\dot{\boldsymbol{\nu}} + \boldsymbol{B}_{total}(\infty)\boldsymbol{\nu}_r + \boldsymbol{\mu} + \boldsymbol{C}\boldsymbol{\eta} + \boldsymbol{\tau}_{cushion} = \boldsymbol{\tau}_{exc} \tag{2.41}$$

$$\dot{\boldsymbol{\zeta}} = \boldsymbol{A}_r\boldsymbol{\zeta} + \boldsymbol{B}_r\delta\boldsymbol{\nu} \tag{2.42}$$

$$\boldsymbol{\mu} = \boldsymbol{C}_r\boldsymbol{\zeta} + \boldsymbol{D}_r\delta\boldsymbol{\nu}, \tag{2.43}$$

where the equations of motion (EOMs) of the Wave Craft are represented by (2.41). In absence of cushion forces, $\boldsymbol{\tau}_{cushion}$, the EOMs exclusively contain linear terms, assuming that all external forces, $\boldsymbol{\tau}_{exc}$, are linear. The model is valid for any excitation, provided that the linear assumption is not violated, meaning that the wave excitation induces small displacements from a state of equilibrium (Fossen, 2011). The cushion forces, $\boldsymbol{\tau}_{cushion}$, contain multiple terms which are varying with respect to time, making the cushion forces nonlinear. Consequently, in presence of motion damping, i.e. cushion forces, equation (2.41), becomes nonlinear. However, these forces and moments are not considered to violate the linear assumption required for the seakeeping model to hold. This is due to the achievable magnitudes of the cushion forces and moments, and the ship motion they are able to induce.

The matrices that enter the kinetics in (2.41) are obtained from ShipX and Veres. They are included in Appendix A.

Chapter 3

Instrumentation

This section is based on Bryn (2016) and will deal with creating suitable signals for vent valve feedback control. This includes choosing appropriate sensors and filtering and discussing kinematic relationships.

3.1 Sensors

The choice of sensors for this project depends on the measurements needed in the feedback control system. By investigating other systems for roll damping, companies such as Vetus (Netherlands), NAIAD (US), Rolls Royce, Island Engineering (US), etc, have developed systems using fins for roll damping. According to Vetus (2011), roll angular velocity is exploited in their feedback control system, measured by a rate gyro.

From simulations, it was discovered that no significant damping was obtained by adding the roll angle as feedback around shorter wave periods (4-5 s). For these periods, which are in the area of the natural period for roll, the greatest roll damping percentages achievable are expected. However, it is supposed that for longer wave periods ($8s+$), roll angle feedback will enhance damping performance. This can be seen from Figure 3.1, which is obtained by simulation. This is showing the roll angle and roll rate response with and without roll angle utilized for feedback. In addition to increasing the damping percentage, two peaks can be seen in the pressure dynamics, which are 90 degrees phase shifted with respect to each other. This is expected as the phase between the roll angle and roll rate is 90 degrees.

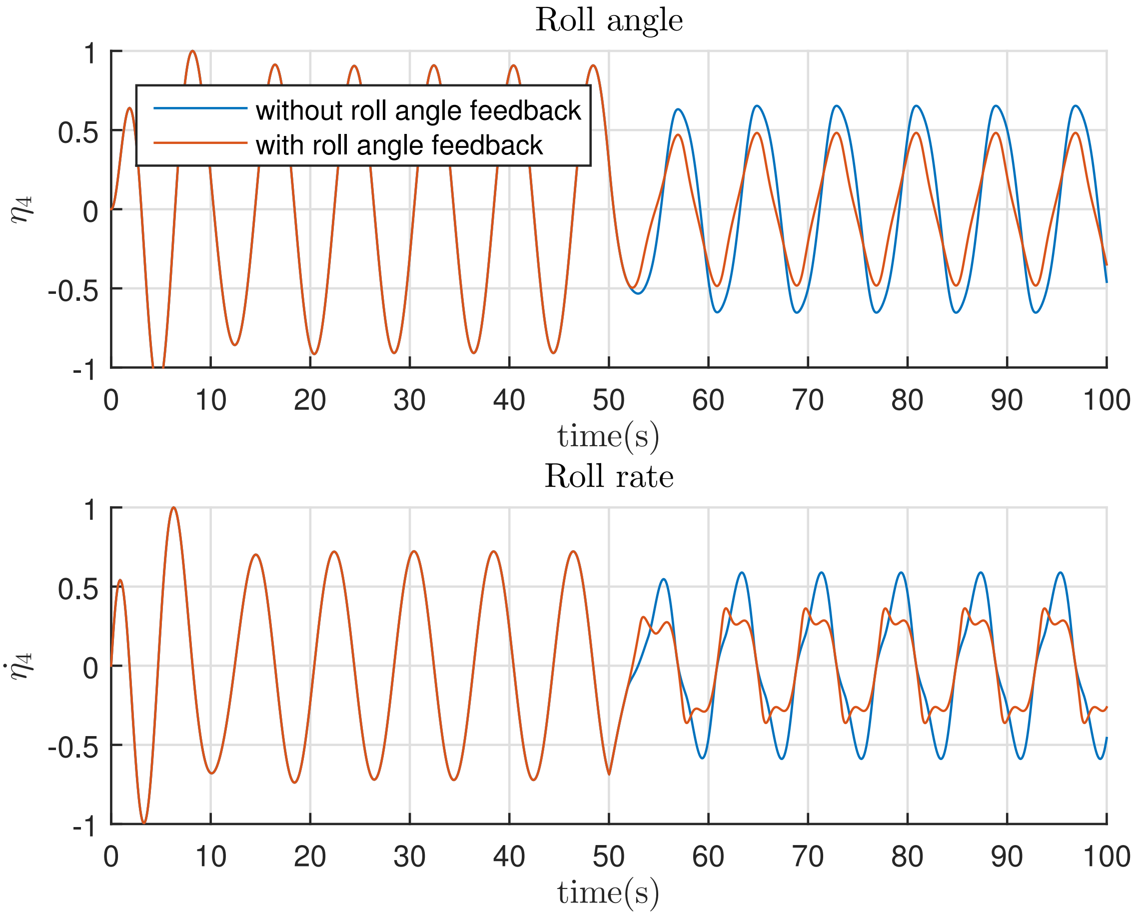

Figure 3.1: Simulated response for wave period of 8s, with and without roll angle as feedback. (Bryn, 2016)

It is assumed that roll rate is sufficient for creating a suitable signal for vent valve feedback control around shorter wave periods in beam seas. However, for longer wave periods, a combination of angle and rate will be investigated as feedback. An inertial measurement unit consisting of a 3-axis gyroscope and a 3-axis accelerometer suffices to measure all the states necessary for the feedback control system for all scenarios during the model test period. Note that yaw angular velocity was never used for feedback.

There are two types of rate gyros that dominate the market for strapdown applications, fiber optic gyros (FOGs) and micro-electro-mechanical-system (MEMS) gyros. According to (Fossen, 2011), MEMS gyros are expected to be dominant for low and medium cost applications. FOGs are expensive, but offers low error characteristics, and are used in high precision navigation (Inc., 2014). For the purpose of roll damping, which does not require very high precision, a MEMS gyro is considered sufficient. They offer low cost and less size and weight. At the other side the error characteristics increase. These errors are discussed further in 3.2.

In order to measure the angles accurately over time, a three axis accelerometer will be implemented in order to calculate absolute angles from the gravity vector. This is assumed to offer sufficient precision if the sway and surge accelerations are small, because the heave acceleration

will then be divided along the three accelerometer axes proportional to the angle, and will not affect the angular measurement.
The pressures in the cushions, aft bag and separating wall are of great interest to verify that system behaves as expected. Three pressure sensors will be implemented since the bag and separating wall pressure are assumed equal and uniform.

3.1.1 Kinematics

Angles from acceleration

The roll and pitch angle, ϕ and θ, respectively, are calculated from the gravity and heave acceleration components along the body axes. These angles are computed according to (Fossen, 2011)

$$\begin{aligned} \phi &= \tan \frac{a_y}{a_z} \\ \theta &= \tan \frac{a_x}{\sqrt{a_y^2 + a_z^2}}, \end{aligned} \tag{3.1}$$

where a_x, a_y and a_z are the body-fixed surge, sway and heave linear acceleration, respectively.

Euler angle transformation

In order to obtain the actual angular coordinates, the body-fixed angular velocity vector, $\boldsymbol{\omega}_{b/n}^b = [p,\ q,\ r]^\top$, from the 3-axis gyro must be transformed to the Euler rate vector, $\dot{\boldsymbol{\Theta}}_{nb} = [\dot{\phi},\ \dot{\theta},\ \dot{\psi}]^\top$, Fossen (2011). The body-fixed angular velocity vector, $\boldsymbol{\omega}_{b/n}^b$, and the Euler rate vector, $\dot{\boldsymbol{\Theta}}_{nb}$, are related through a transformation matrix, $\boldsymbol{T}_\Theta(\boldsymbol{\Theta}_{nb})$, according to

$$\dot{\boldsymbol{\Theta}}_{nb} = \boldsymbol{T}_\Theta(\boldsymbol{\Theta}_{nb})\boldsymbol{\omega}_{b/n}^b \tag{3.2}$$

where

$$\boldsymbol{T}_\Theta(\boldsymbol{\Theta}_{nb}) = \begin{bmatrix} 1 & \sin\phi\tan\theta & \cos\phi\tan\theta \\ 0 & \cos\phi & -\sin\phi \\ 0 & \sin\phi/\cos\theta & \cos\phi/\cos\theta \end{bmatrix}. \tag{3.3}$$

The yaw angular velocity is considered to be equal to zero, i.e. $\boldsymbol{\omega}_{b/n}^b = [p,\ q,\ 0]^\top$. The roll, pitch and yaw rate are expressed according to

$$\begin{aligned} \dot{\phi} &= p + q\sin\phi\tan\theta \\ \dot{\theta} &= q\cos\phi \\ \dot{\psi} &= q\frac{\sin\phi}{\cos\theta} \end{aligned} \tag{3.4}$$

It is seen from (3.4) that the roll rate, $\dot{\phi}$, is equal to the roll angular velocity, p, in absence of pitch motions, $q = 0$.

3.2 Signal Processing

This section deals with creating suitable signals for vent valve feedback control. Since this is a low-speed application where a marine craft is moving on the surface of the earth, it is assumed that the NED frame, {n}, is non-rotating and thereby inertial. With this assumption, the 3-axis gyroscope measurements of the angular velocities $\boldsymbol{\omega}^b_{m/n} = [p,\ q,\ r]$ can be expressed by Equation (11.220) in Fossen (2011) as follows

$$\boldsymbol{\omega}^b_{imu} = \boldsymbol{\omega}^b_{m/n} + \boldsymbol{b}^b_{gyro} + \boldsymbol{w}^b_{gyro} \tag{3.5}$$

From this equation it is seen that the angular velocity is measured in frame {m} relative to {n}. This occurs since the gyro is strapped to the craft and the measurements are compensated by a lever arm. The lever arm vector, r^b_m, moves the measurements from the origin of {m} to the origin of {b}.

In a perfect world, the frame {m} will be aligned with {b}, exploiting lever arm compensation only along the z-axis. When mounting the gyro, small misalignment errors will be present. In (3.5) such errors, and also scale factor errors, can be neglected for low-speed applications according to Fossen (2011).

The two error sources in (3.5), bias and noise, are often referred to as bias instability and angular random walk (ARW), respectively. The term ARW is used as the noise will have random walk characteristics for the angle when the noise is integrated (Freescale, 2015). The bias instability is a random walk for the bias due to mechanical and electrical characteristics of the MEMS gyro (Freescale, 2015).

The dominant error source of the accelerometer is the noise. Accelerometers are very sensitive to vibrations, hence sources of vibrations such as the lift fans will induce large amount of noise in the calculated angles.

3.2.1 Low-pass Filter

If only roll rate is considered for feedback, a low-pass filter would be sufficient, as the high frequency measurement noise will dominate the bias instability. The bandwidth of the low-pass filter must be chosen in such a way that as much as possible of the high frequency noise, w^b_{gyro}, due to vibrations and other noise sources, is cancelled. It is undesirable that the low-pass filter induces phase lag and damping of the roll rate response. Therefore, the choice of the bandwidth of the filter is a trade-off between noise suppression and sensing the vital dynamics of the system. The implemented first order low-pass filter has the transfer function

$$H(s) = \frac{1}{\tau s + 1}, \tag{3.6}$$

where $\tau = \frac{1}{f_{cutoff}}$ is the time constant, which is adjusted until satisfactory results are achieved. The bandwidth of the system, which is the frequency of the wave interval of interest, occurs

for $0.125 - 0.25\ Hz$ full scale. These wave period intervals are gathered from actual offshore wind farm ocean data. If the period is below 4 seconds, then the wave height is so small that vessel motions are below the requirement for motion control. If the periods are higher, which they rarely are, sailing will not be relevant regardless since motions on the turbines will be to great for operation and maintenance work.
The time constant must be chosen greater than these periods in order to retain the interesting dynamics. Figure 3.2 shows a normalized plot of the raw and filtered roll rate measurement. There will be a trade-off between phase lag and noise suppression for the filtered output. As seen from the plot, the filtered output is smooth, since almost all of the high frequency noise is filtered out. It is following the raw signal with a slight phase lag, which is acceptable for this application.

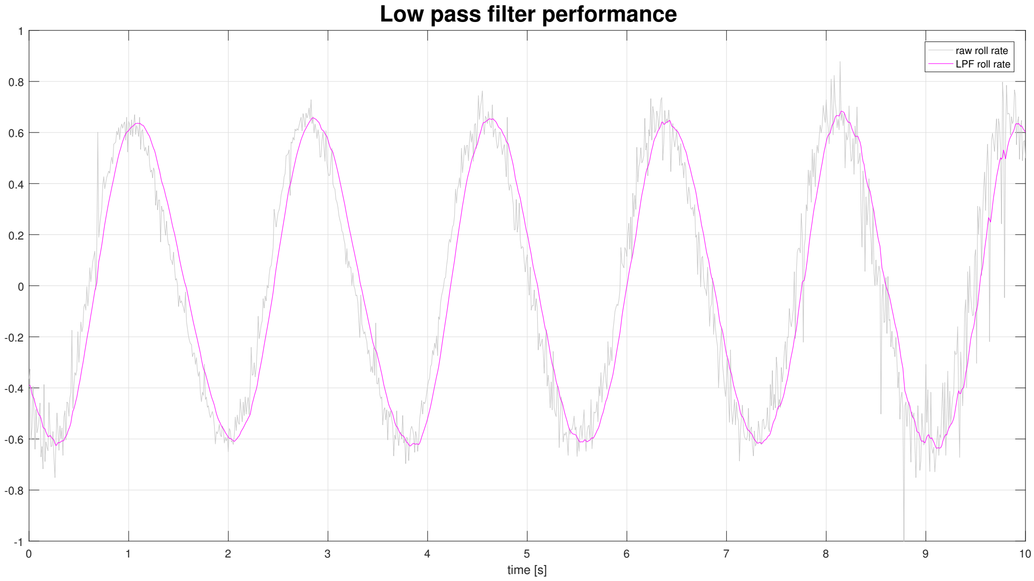

Figure 3.2: Low-pass filter performance in beam seas with wave height of 2 meters and period of 5 seconds.

As it is of interest to exploit the roll and pitch angle for feedback, estimation of these will be investigated in Chapter 4.

Chapter 4

Control System and Observer Design

Figure 4.1 illustrates the control hierarchy. The control system is implemented on a CompactRIO controller, which is presented in Section 5.2.1.

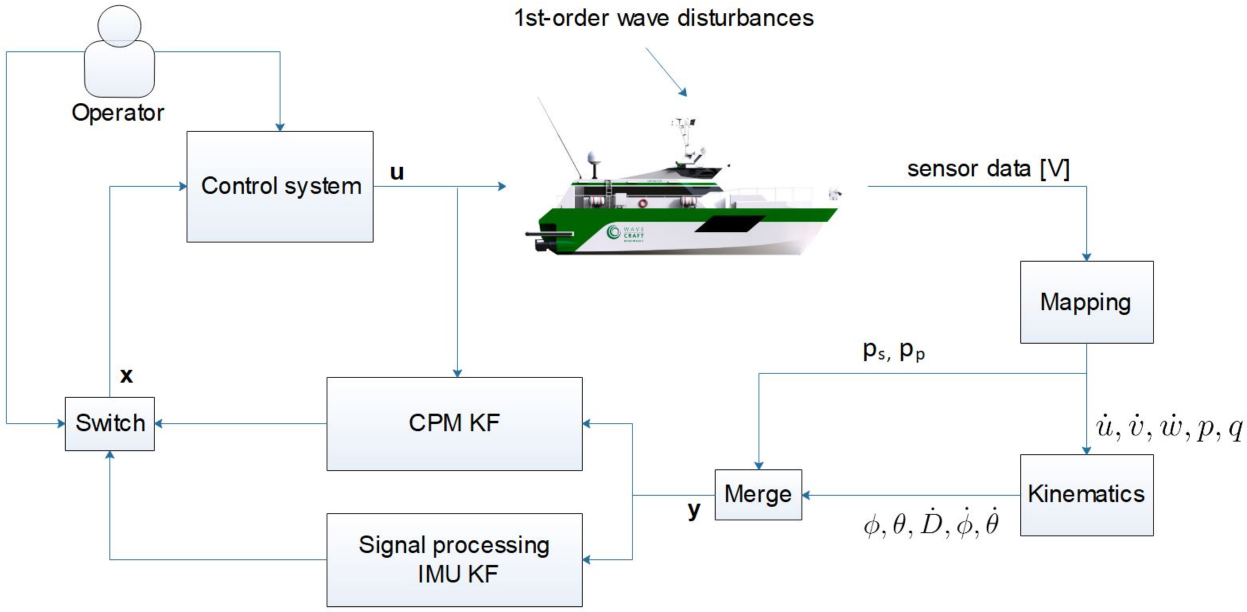

Figure 4.1: Control system overview.

The vessel is subject to 1st-order wave induced motions. The behaviour of the model scale vessel is caught by multiple sensors, where their raw data is measured in voltage. Consequently, all sensor data is mapped to dimensions that have physical meaning. The body-fixed mapped angular velocities for roll and pitch, p and q, respectively, and linear accelerations for surge, sway and heave, $\dot{u}$, $\dot{v}$ and $\dot{w}$, respectively, are exploited in the kinematics block to provide the roll and pitch angle, ϕ and θ, respectively, and also the heave, roll and pitch rate, $\dot{D}$, $\dot{\phi}$ and $\dot{\theta}$, respectively, expressed in the NED-frame. The measurement vector is fed forward to the Kalman filter (KF) blocks and signal processing, $\boldsymbol{y}$, consists of these NED-variables and the starboard and port air cushion pressures, p_s and p_p, respectively. Two Kalman filters are designed. CPM KF exploits the linear CPM, while IMU KF exclusively utilizes gyro and accelerometer data for sensor fusion. Signal processing, like low-pass filtering, is also performed to generate smooth feedback signals. A switching mechanism is used to provide the controller with the most suitable feedback signals vector, $\boldsymbol{x}$. Two controllers are designed; a PID controller that is possible to tune real-time in VeriStand by an operator, and a hybrid controller which utilizes gain scheduling dependent on environmental conditions. The control system provides the vent valves with desired position commands, $\boldsymbol{u}$.

The control objective is to damp roll motions. This is obtained by exclusively exploiting the vent valves for counteracting these motions. The control objectives are formulated in the NED-frame according to

$$\dot{\phi}(t) - \dot{\phi}_d = 0 \tag{4.1}$$

$$\phi(t) - \phi_d = 0 \tag{4.2}$$

where $\dot{\phi}_d = \phi_d = 0$. Additionally, cases where it make sense to compensate for both roll and heave motions, simultaneously, are investigated. Then, heave rate expressed in the NED-frame is also forced to zero, i.e.

$$\dot{D}(t) - \dot{D}_d = 0 \tag{4.3}$$

where $\dot{D}_d = 0$. Typically, when the Wave Craft is exposed to head seas the wave influence is greater for heave and pitch than roll. The Boarding Control System (BCS) is designed for damping of vertical motion at the bow, which is a combination of heave and pitch motions. Hence, when the BCS is exploited for vertical bow motion damping the control objective is defined as

$$\ddot{D}_{bow} - \ddot{D}_{bow_d} = 0 \tag{4.4}$$

where $\ddot{D}_{bow_d} = 0$.

4.1 Observer Design

It is considered advantageous to exploit estimated states from an observer (state estimator) as input to the control systems for multiple reasons.

- The state estimator is able to reconstruct non-measured data, meaning it estimates process states that are not measured. This is a huge advantage, the CompactRIO has limited numbers of analog inputs and proper sensors for all process states are not available.
- The input to the observer is sensor data from a three-axis gyro, a three-axis accelerometer and two pressure sensors. An observer computes unbiased estimates and also performs filtering before the signals are used in feedback control systems.

- All kind of equipment, like sensors, will fail according to a certain failure rate. Experience from industrial applications has shown that one of the most frequent control system failure are caused by sensor failures (Sørensen, 2013). State estimators make dead reckoning possible. That is in the case of sensor drop out, the state estimator exploits the mathematical model of the Wave Craft and predict its behaviour, independent of sensor measurements. In the case of dead reckoning, the control signals exclusively exist of model prediction.
- An observer is also able to perform wave filtering, dividing the motion of the marine vessel into one low-frequent (LF) and one wave-frequent (WF) component. Typically, in DP applications the WF component is not compensated for, due to the wear and tear it will induce on actuators and other control system components. However, for the Wave Craft the objective is to damp WF motions due to first-order wave loads.

Both the Kalman filter and the nonlinear passive observer were considered appropriate for the state estimation objectives for this project. The Kalman filter is suited to exploit the linear control plant model in (2.11), while the nonlinear passive observer can utilize the nonlinear process plant model in (2.40)-(2.43). The Kalman filter was preferred. It make sense to exploit the linear CPM model instead of the more complex nonlinear PPM for the observer design. It is also desired that the fluid memory effect terms in (2.41)-(2.43) and also the nonlinear pressure dynamics in 2.23 do not enter the observer model. It is also possible to add additional states of interest like pressures to the state vector for the Kalman filter.

4.1.1 CPM KF

This section is based on Vik (2014). A mathematical model and state estimation propagation that runs real-time on the CompactRIO are developed. Additionally, a wave estimator is established to feed estimated wave excitation forces and moments forward to the observer, and thereby obtain more realistic state estimates.

Model

The CompactRIO operates in discrete time, while the physical process plant, the behaviour of Wave Craft, operates in continuous time. Hence, the mathematical model of the motion for the Wave Craft is discretized and utilized in a discrete observer. By using forward Euler discretization, the process equation in (2.11) is written

$$\frac{1}{h}\big(\boldsymbol{x}(k+1)-\boldsymbol{x}(k)\big) = \boldsymbol{A}\boldsymbol{x}(k)+\boldsymbol{B}\boldsymbol{u}(k)+\bar{\boldsymbol{E}}\bar{\boldsymbol{w}}(k). \tag{4.5}$$

h is the sampling time and $\bar{\boldsymbol{E}}$ and $\boldsymbol{w}(t) = \begin{bmatrix} F_3^e(t) & F_4^e(t) & F_5^e(t) \end{bmatrix}^\top$ are the reduced disturbance matrix and vector, respectively. The wave volume pumping for both cushions are not included in the mathematical model for the Kalman filter. It is expected that the uncertainties concerning these parameters will induce inaccurate state estimations. $\bar{\boldsymbol{E}}$ is included in Appendix A. Solving for the state vector propagation at time $k+1$, $\boldsymbol{x}(k+1)$, leads to

$$\boldsymbol{x}(k+1) = \big(\boldsymbol{I} + h\boldsymbol{A}\big)\boldsymbol{x}(k) + h\boldsymbol{B}\boldsymbol{u}(k) + h\bar{\boldsymbol{E}}\bar{\boldsymbol{w}}(k), \tag{4.6}$$

where

$$\boldsymbol{\Phi} = \boldsymbol{I} + h\boldsymbol{A} \tag{4.7}$$

$$\boldsymbol{\Delta} = h\boldsymbol{B} \tag{4.8}$$

$$\boldsymbol{\Gamma} = h\bar{\boldsymbol{E}}. \tag{4.9}$$

The measurement equation in (2.11) is written

$$\boldsymbol{y}(k) = \boldsymbol{H}\boldsymbol{x}(k) + \boldsymbol{v}(k), \tag{4.10}$$

where

$$\boldsymbol{H} = \boldsymbol{C}. \tag{4.11}$$

Hence, the discretization of the CPM in (2.11) can be written

$$\boldsymbol{x}(k+1) = \boldsymbol{\Phi}\boldsymbol{x}(k) + \boldsymbol{\Delta}\boldsymbol{u}(k) + \boldsymbol{\Gamma}\bar{\boldsymbol{w}}(k) \tag{4.12}$$

$$\boldsymbol{y}(k) = \boldsymbol{H}\boldsymbol{x}(k) + \boldsymbol{v}(k). \tag{4.13}$$

Propagation

In order to utilize an observer like the Kalman filter, the pair (Φ,H) must be observable. This is the case when it is possible to reconstruct any unknown initial state vector, $\boldsymbol{x}(0)$, uniquely, by exploiting the known input sequence vector, $\boldsymbol{u}(k)$, and measurement sequence vector, $\boldsymbol{y}(k)$ (Sørensen, 2013). The observability criteria is satisfied when the matrix

$$O = [\boldsymbol{H}^\top, \boldsymbol{\Phi}^\top\boldsymbol{H}^\top, ..., (\boldsymbol{\Phi}^\top)^{n-1}\boldsymbol{H}^\top], \tag{4.14}$$

has full column rank. Here, $n = 8$ is the number of states. The MATLAB function `obsv` is used to compute the observability matrix, O. $\text{rank}(O) = n = 8$ proves that the matrix has full column rank, i.e. the Kalman filter can be utilized for state estimation.

The process noise vector and measurement noise vector, $\boldsymbol{w}(k)$ and $\boldsymbol{v}(k)$, respectively, are zero mean Gaussian white noise processes. The second moment, $E[(x-\mu)^2]$, the variance, of the process noise vector and measurement noise vector form the covariance matrices $\boldsymbol{Q}_d(k)$ and $\boldsymbol{R}_d(k)$, respectively, according to

$$E[\boldsymbol{w}(k)\boldsymbol{w}^\top(j)] = \begin{cases} \boldsymbol{Q}_d(k) = \boldsymbol{Q}_d^\top(k) > 0 & \text{if } j = k \\ 0 & \text{if } j \neq k \end{cases} \tag{4.15}$$

$$E[\boldsymbol{v}(k)\boldsymbol{v}^\top(j)] = \begin{cases} \boldsymbol{R}_d(k) = \boldsymbol{R}_d^\top(k) > 0 & \text{if } j = k \\ 0 & \text{if } j \neq k \end{cases} \tag{4.16}$$

$$E[\boldsymbol{w}(k)\boldsymbol{v}^\top(j)] = 0 \quad \text{for all } k \text{ and } j. \tag{4.17}$$

The variances of the sensor measurements were found when calibrating the sensors. This formed the measurement noise covariance matrix, $\boldsymbol{R}_d(k)$, according to

$$\boldsymbol{R}_d(k) = \begin{bmatrix} var\big(\eta_4(k)\big) & 0 & 0 & 0 & 0 & 0 & 0 \\ 0 & var\big(\eta_5(k)\big) & 0 & 0 & 0 & 0 & 0 \\ 0 & 0 & var\big(\dot{\eta}_3(k)\big) & 0 & 0 & 0 & 0 \\ 0 & 0 & 0 & var\big(\dot{\eta}_4(k)\big) & 0 & 0 & 0 \\ 0 & 0 & 0 & 0 & var\big(\dot{\eta}_5(k)\big) & 0 & 0 \\ 0 & 0 & 0 & 0 & 0 & var(p_s) & 0 \\ 0 & 0 & 0 & 0 & 0 & 0 & var(p_p) \end{bmatrix}. \tag{4.18}$$

The diagonal elements of the process noise covariance matrix, $q_{ii}(k)$ for $i = 1 \ldots 8$, represent the variances of the process states, $x_1(k) \ldots x_8(k)$. The process noise covariance matrix, $\boldsymbol{Q}_d(k)$, is written

$$\boldsymbol{Q}_d(k) = \begin{bmatrix} var(x_1(k)) & 0 & 0 & 0 & 0 & 0 & 0 & 0 \\ 0 & var(x_2(k)) & 0 & 0 & 0 & 0 & 0 & 0 \\ 0 & 0 & var(x_3(k)) & 0 & 0 & 0 & 0 & 0 \\ 0 & 0 & 0 & var(x_4(k)) & 0 & 0 & 0 & 0 \\ 0 & 0 & 0 & 0 & var(x_5(k)) & 0 & 0 & 0 \\ 0 & 0 & 0 & 0 & 0 & var(x_6(k)) & 0 & 0 \\ 0 & 0 & 0 & 0 & 0 & 0 & var(x_7(k)) & 0 \\ 0 & 0 & 0 & 0 & 0 & 0 & 0 & var(x_8(k)) \end{bmatrix}. \tag{4.19}$$

While the diagonal elements of the measurement noise covariance matrix, $r_{ii}(k)$, are determined by the variances of the sensors and are thereby fixed, the diagonal elements of the process noise covariance matrix are tunable. The relationship $\frac{q_{i+1,i+1}(k)}{r_{ii}(k)}$ for $i = 1 \ldots 7$ determines how much trust the Kalman filter gives to the mathematical model versus the measurements when propagating further. If the numerical value for this relationship is large for a given state, the variance of this process state is set high. Then, the Kalman filter trusts the measurement more than the mathematical model for this state.

The Kalman filter is basically a predict-update loop. In the prediction phase the filter exploits the mathematical model of the Wave Craft and estimates the process states and error covariances at the next time sample. When measurements from the sensors are available, the filter updates the state estimates and the error covariances from the prediction phase. The Kalman filter is initialized by setting an initial state vector, $\boldsymbol{x_0}$, and an initial error covariance matrix, $\boldsymbol{P_0}$, according to

$$\boldsymbol{x_0} = \bar{\boldsymbol{x}}(0) = \mathbf{0}_{8x1} \tag{4.20}$$

$$\boldsymbol{P_0} = \bar{\boldsymbol{P}}(0) = E[\big(\boldsymbol{x}(0) - \hat{\boldsymbol{x}}(0)\big)\big(\boldsymbol{x}(0) - \hat{\boldsymbol{x}}(0)\big)^\top] = \mathbf{0}_{8x8}. \tag{4.21}$$

In the update phase, the Kalman gain matrix, $\boldsymbol{K}(k)$, the state estimation update vector, $\hat{\boldsymbol{x}}(k)$, and the error covariance update matrix, $\hat{\boldsymbol{P}}(k)$, are computed at sample k according to

$$\boldsymbol{K}(k) = \bar{\boldsymbol{P}}(k)\boldsymbol{H}^\top[\boldsymbol{H}\bar{\boldsymbol{P}}(k)\boldsymbol{H}^\top + \boldsymbol{R}_d(k)]^{-1} \tag{4.22}$$

$$\hat{\boldsymbol{x}}(k) = \bar{\boldsymbol{x}}(k) + \boldsymbol{K}(k)[\boldsymbol{y}(k) - \boldsymbol{H}\bar{\boldsymbol{x}}(k)] \tag{4.23}$$

$$\hat{\boldsymbol{P}}(k) = [\boldsymbol{I} - \boldsymbol{K}(k)\boldsymbol{H}]\bar{\boldsymbol{P}}(k)[\boldsymbol{I} - \boldsymbol{K}(k)\boldsymbol{H}]^\top + \boldsymbol{K}(k)\boldsymbol{R}_d(k)\boldsymbol{K}^\top(k). \tag{4.24}$$

In the prediction phase, the the state estimation propagation vector, $\bar{\boldsymbol{x}}(k+1)$, and the error covariance propagation matrix, $\bar{\boldsymbol{P}}(k+1)$, are calculated at sample $k+1$ according to

$$\bar{\boldsymbol{x}}(k+1) = \boldsymbol{\Phi}\hat{\boldsymbol{x}}(k) + \boldsymbol{\Delta u}(k) \tag{4.25}$$

$$\bar{\boldsymbol{P}}(k+1) = \boldsymbol{\Phi}\hat{\boldsymbol{P}}(k)\boldsymbol{\Phi}^\top + \boldsymbol{\Gamma}\boldsymbol{Q}_d(k)\boldsymbol{\Gamma}^\top. \tag{4.26}$$

The a posteriori estimate vector, $\hat{\boldsymbol{x}}(k)$, is fed forward to the controller. Equation (4.23) contains the injection term, $\boldsymbol{y}(k) - \boldsymbol{H}\bar{\boldsymbol{x}}(k)$. This is where the sensor measurements, $\boldsymbol{y}(k)$, are compared to the corresponding process state estimates, $\boldsymbol{H}\bar{\boldsymbol{x}}(k)$. In the case of dead reckoning or low-frequent measurement updates $\boldsymbol{y}(k) = \mathbf{0}_{5x1}$.

Wave Estimation

Motion response amplitude operators (motion RAOs) are exploited to estimate the wave-induced motion of the Wave Craft. This is done by capturing the total motion of the craft, which may be both pressure- and wave-induced. The linear model of the Wave Craft can be written

$$[\mathbf{M}_{RB} + \mathbf{A}(\omega)]\ddot{\boldsymbol{\xi}} + \mathbf{B}(\omega)\dot{\boldsymbol{\xi}} + \mathbf{C}\boldsymbol{\xi} = \boldsymbol{\tau}_{we} + \boldsymbol{\tau}_{cushion}. \tag{4.27}$$

By assuming harmonic motions

$$\boldsymbol{\xi} = \bar{\boldsymbol{\xi}}\cos(\omega t), \tag{4.28}$$

where $\bar{\boldsymbol{\xi}}$ is a vector of amplitudes (Fossen, 2011), equation (4.27) is written

$$-\omega^2[\boldsymbol{M}_{RB} + \boldsymbol{A}(\omega)]\bar{\boldsymbol{\xi}} - j\omega\boldsymbol{B}(\omega)\bar{\boldsymbol{\xi}} + \boldsymbol{C}\bar{\boldsymbol{\xi}} = \bar{\boldsymbol{\tau}}_{tot}, \tag{4.29}$$

where $\bar{\boldsymbol{\tau}}_{tot} = \boldsymbol{\tau}_{we} + \boldsymbol{\tau}_{cushion}$ and the wave excitation vector is $\boldsymbol{\tau}_{we} = \begin{bmatrix} F_3^e(k) & F_4^e(k) & F_5^e(k) \end{bmatrix}^\top$. Hence, the responses can be written

$$\bar{\boldsymbol{\xi}} = \boldsymbol{H}_v(j\omega)\bar{\boldsymbol{\tau}}_{tot}, \tag{4.30}$$

where the force-to-motion transfer function

$$\boldsymbol{H}_v(j\omega) = [-\omega^2[\boldsymbol{M}_{RB} + \boldsymbol{A}(\omega)] - j\omega\boldsymbol{B}(\omega) + \boldsymbol{C}]^{-1}, \tag{4.31}$$

is a low-pass filter, representing the vessel dynamics. Since the Kalman filter is estimating heave displacement, roll and pitch angle, and also heave, roll and pitch rate it is possible to utilize (4.27) to estimate the total force vector, $\bar{\boldsymbol{\tau}}_{tot}$. Since the air cushion pressures are estimated and the air cushion areas and the longitudinally and transverse lever arms are considered constant for both cushions, the cushion forces, $\boldsymbol{\tau}_{cushion}$, can be estimated. When assuming that the vessels motion is induced by either first-order wave loads or air cushion pressures, the wave excitation forces are estimated by utilizing the estimated total force vector, $\boldsymbol{\tau}_{tot}$, and the estimated cushion forces, $\boldsymbol{\tau}_{cushion}$.

4.1.2 IMU KF

As an alternative solution to the CPM KF, a simpler approach is investigated. A Kalman filter based exclusively on sensor measurements, the IMU KF, is established. This focuses on obtaining estimates of the roll and pitch angles without using a mathematical model of the system. Instead, information about the error characteristics of the sensors is exploited.

By performing sensor fusion, one are able to utilize the "best of both worlds". This is done by combining the noisy roll and pitch angle estimates, which utilize the gravitational vector as described in Chapter 3, and the integrated gyro rate measurements. The later measurements are smoother but suffer from drift. The gyro biases are estimated in order to compensate for the roll rate measurement. The IMU KF is designed under the assumptions that

- All noise processes can be assumed Gaussian white noise processes.
- The angles calculated from the accelerometer is accurate, but not precise.
- The angles calculated from the gyro are precise but not accurate.

When the assumptions above are valid, the estimated angles will be both accurate and precise, and also unbiased with minimum variance.

The bias instability in equation (3.5), referred to as $\boldsymbol{b}^b_{gyro}$, can according to Vik (2014) be modelled as a 1st order Gauss-Markov process, which is described by letting white noise travel through a low-pass filter.

$$\dot{b}(t) = -\frac{1}{T}b(t) + w(t), \tag{4.32}$$

where $v(t)$ is zero mean white noise and T is the Markov time constant. In the frequency plane it can be expressed as

$$b(s) = \frac{1}{s + \frac{1}{T}} w(s). \tag{4.33}$$

The gyro rates will work as inputs to the filter, while the angles from the accelerometer will be used to update the filter. The state, input and disturbance vector for the Kalman filter can then be described by

$$\boldsymbol{x}_{IMU}(t) = \begin{bmatrix} \theta(t) \\ \phi(t) \\ b_1(t) \\ b_2(t) \end{bmatrix} \quad \boldsymbol{u}_{IMU}(t) = \begin{bmatrix} \omega_{gyro}^{roll}(t) \\ \omega_{gyro}^{pitch}(t) \end{bmatrix} \quad \boldsymbol{w}_{IMU}(t) = \begin{bmatrix} w_1(t) \\ w_2(t) \\ w_3(t) \\ w_4(t) \end{bmatrix}. \tag{4.34}$$

The differential equations describing the sensor dynamics can be expressed as

$$\begin{aligned} \dot{\theta}(t) &= \omega_{gyro}^{roll}(t) + b_1(t) + w_1(t) \\ \dot{\phi}(t) &= \omega_{gyro}^{pitch}(t) + b_2(t) + w_2(t) \\ \dot{b_1}(t) &= -\frac{1}{T_1} b_1(t) + w_3(t) \\ \dot{b_2}(t) &= -\frac{1}{T_2} b_2(t) + w_4(t). \end{aligned} \tag{4.35}$$

With the measurement equations

$$\begin{aligned} y_1(t) &= \theta(t) + v_1(t) \\ y_2(t) &= \phi(t) + v_2(t). \end{aligned} \tag{4.36}$$

In order to implement this in a kalman filter, the equations are expressed on state-space form according to

$$\dot{\boldsymbol{x}}_{IMU}(t) = \boldsymbol{A}_{IMU}\boldsymbol{x}_{IMU}(t) + \boldsymbol{B}_{IMU}\boldsymbol{u}_{IMU}(t) + \boldsymbol{E}_{IMU}\boldsymbol{w}_{IMU}(t), \tag{4.37}$$

where

$$\boldsymbol{A}_{IMU} = \begin{bmatrix} 0 & 0 & 1 & 0 \\ 0 & 0 & 0 & 1 \\ 0 & 0 & -\frac{1}{T_1} & 0 \\ 0 & 0 & 0 & -\frac{1}{T_2} \end{bmatrix} \quad \boldsymbol{B}_{IMU} = \begin{bmatrix} 1 & 0 \\ 0 & 1 \\ 0 & 0 \\ 0 & 0 \end{bmatrix} \quad \boldsymbol{E}_{IMU} = \boldsymbol{I}_{4x4}. \tag{4.38}$$

4.2 Observer Verification

4.2.1 Simulations

The CPM varies dependent on wave frequency. This is a problem when utilizing the CPM for observer design. The rigid-mass matrix, $\boldsymbol{M}_{RB}$, and the restoring matrix, $\boldsymbol{C}$, are constant, but the added mass matrix, $\boldsymbol{A}(\omega)$, and the added damping matrix, $\boldsymbol{B}(\omega)$, are wave frequency dependent. Added mass and added damping are utilized to estimate the total force, $\boldsymbol{\tau}_{tot}$, in (4.27). Therefore, the wave estimation may not hold for different wave frequencies. Consequently, the Kalman filter is valid for all wave heights and directions, but not necessarily for all wave frequencies. Two approaches were considered to solve this problem

- Exploit multiple Kalman filters valid for different wave frequencies. An adaptive switching mechanism dependent on wave frequency could have been used.
- Design a Kalman filter for one frequency. Then tune the process noise covariance matrix, $\boldsymbol{Q}_d(k)$, dependent on how much the wave frequency deviates from the design frequency.

It is considered beneficial to use only one observer, instead of switching between multiple observers. Therefore, approach 2 is investigated further. The idea is to assign greater numerical values for the diagonal elements of $\boldsymbol{Q}_d(k)$, and thereby greater variance, when the wave frequency deviates from the design frequency. Then the Kalman filter prioritizes the measurements. Table 4.1 shows how added mass, $\boldsymbol{A}(\omega)$, and added damping, $\boldsymbol{B}(\omega)$, for chosen DOFs vary dependent on wave frequency. These parameters are obtained from ShipX and VERES. It is desirable to damp motion that is induced by waves with period of approximately 5-8 seconds. Table 4.1 illustrates that the parameters exploited in the Kalman filter and wave estimation vary significantly dependent on wave frequency.

Table 4.1: Added mass and added damping parameters

Parameter	Description	Frequency $[\frac{rad}{s}]$		
		0.7854 (8s)	0.9520 (6.5s)	1.2566 (5s)
$A_{33}(\omega)$	Added mass heave	$0.260 \cdot 10^5$	$0.225 \cdot 10^5$	$0.183 \cdot 10^5$
$A_{44}(\omega)$	Added mass roll	$0.569 \cdot 10^6$	$0.505 \cdot 10^6$	$0.426 \cdot 10^6$
$A_{55}(\omega)$	Added mass pitch	$0.774 \cdot 10^6$	$0.673 \cdot 10^6$	$0.554 \cdot 10^6$
$B_{33}(\omega)$	Added damping heave	$0.187 \cdot 10^5$	$0.201 \cdot 10^5$	$0.207 \cdot 10^5$
$B_{44}(\omega)$	Added damping roll	$0.382 \cdot 10^6$	$0.421 \cdot 10^6$	$0.485 \cdot 10^6$
$B_{55}(\omega)$	Added damping pitch	$0.545 \cdot 10^6$	$0.590 \cdot 10^6$	$0.621 \cdot 10^6$

However, simulations indicate that this is not a problem. The observer is tested extensively for head, bow, beam, quartering and following seas with wave height of 2 meters and periods of 5 - 8 seconds. Even by exploiting a fixed process noise covariance matrix, $\boldsymbol{Q}_d(k)$, the observer works as intended. It is designed for 5 seconds wave period, i.e. the added mass and damping parameters in the right column of Table 4.1 are utilized for both the Kalman filter and the wave estimation. Two simulations of the observer response is presented here; beam seas with period of 5 and 8 seconds.

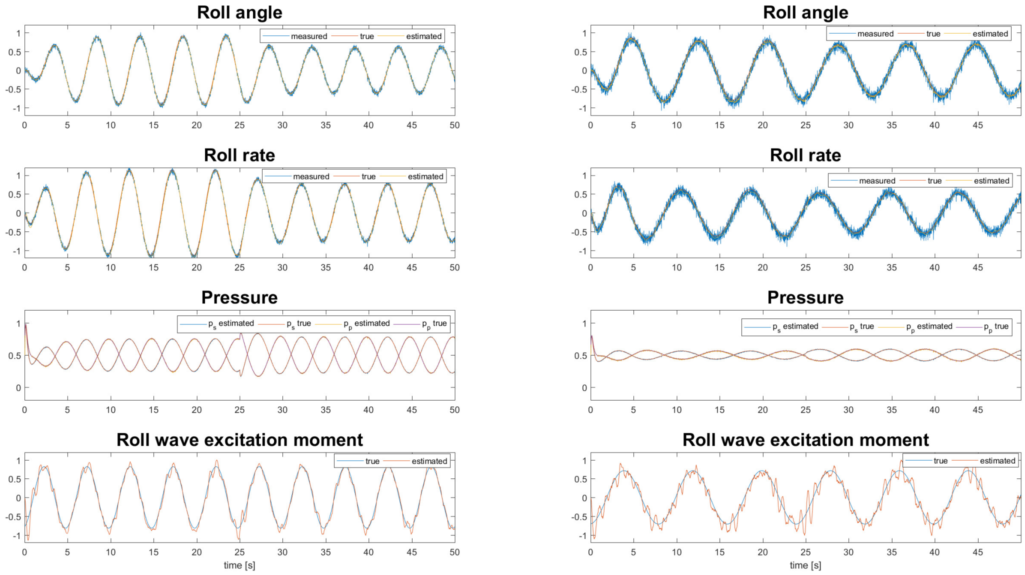

Figure 4.2: Kalman filter response for beam seas with wave height of 2 meters and period of 5 and 8 seconds, left and right figure, respectively.

Figure 4.2 illustrates the estimation performance of the observer for beam seas with 5 and 8 seconds period, shown in the left and right figure, respectively. It is seen that the estimated roll angle and roll rate obtained from the Kalman filter for both cases have excellent accuracy when comparing to the actual states. The observer provides great noise suppression, on the other side phase lag may be present for the estimates. This is expected since the Kalman filter has low-pass filter capabilities. By trusting the model, and put less trust in the measurements, the estimates contain less measurement noise and bias but phase lag may occur.

From (2.11) it is seen that the heave displacement and the roll and pitch angles are computed by pure integration of their respective rates. The estimated rates are not perfect, i.e. they are not identical to the true rates and they may contain noise, bias and phase lag. Therefore, it is expected that the integrated states, the heave displacement and the roll and pitch angles, will drift with random walk characteristics. The Kalman filter utilizes the roll and pitch estimates from the accelerometer data to correct for the random walk drift, therefore their estimates are unbiased when choosing proper roll and pitch angle weights, q_{22} and q_{33}, respectively.

The roll wave excitation moment estimate is accurate but not necessarily precise when compared to the actual roll wave excitation moment. This occurs since the estimated roll angle, roll rate and the rate of change of the roll rate are multiplied with the restoring, added damping, and added mass and inertia coefficients for roll, respectively. These parameters have great numerical value, as indicated in Table 4.1, meaning that a small deviation between e.g. estimated and true roll rate, will induce a large deviation for the true and estimated roll wave excitation moment. From the pressure time series for both cases it is seen that the cushion pressure estimates are noisy. This occurs since the starboard and port process noise covariance parameters, q_{77} and q_{88}, respectively, have great numerical value, implying that the cushion pressures for the mathematical model are not trusted. This is indented, since the wave volume pumping affecting the pressures is not included in CPM KF. The noisy pressure estimates do not cause problems since they are not utilized for feedback and do not induce noisy roll angle and roll rate estimates.

4.2.2 Model Tests

In order to ensure that appropriate signals were fed forward to the controller, the different KFs were tested and compared initially during the model test period. Noise suppression and minimum phase lag for the feedback signals were emphasized. It was considered crucial to obtain smooth control signals, and thereby reducing the wear and tear for the vent valves. Obviously, it was of great importance that the feedback signals were as close to their true states as possible.
The response for the IMU KF is shown in Figure 4.3. The estimated angle is both precise and accurate as expected, which can be seen from the top and bottom left plot. The bottom right plot shows the estimated bias together with the bias component for the roll rate. The bias is a low-frequent component of the roll rate signal and can hence be obtained by low pass filtering the roll rate with a sufficiently large time constant such that all dynamics are filtered out.

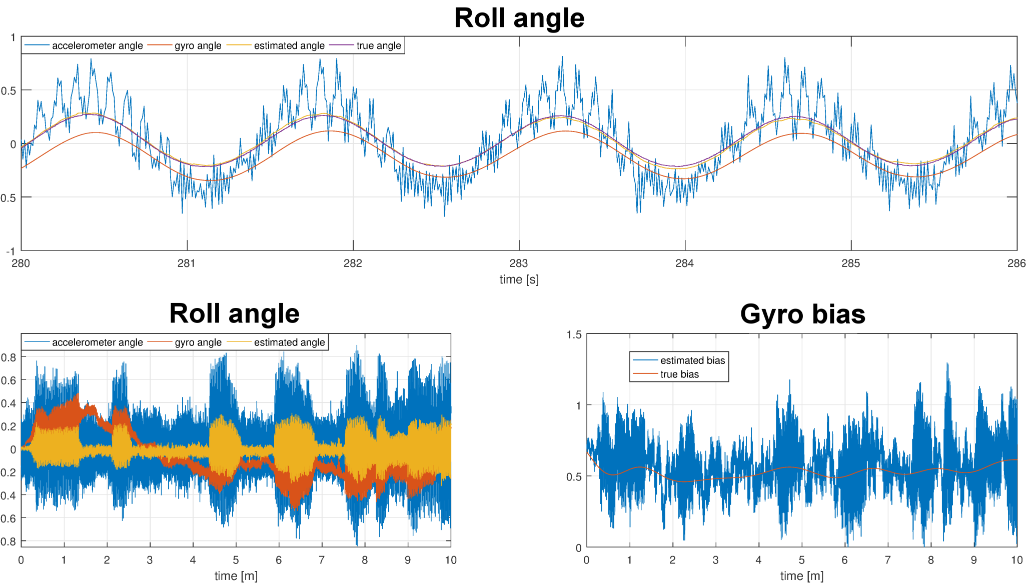

Figure 4.3: IMU KF response. The top plot shows a segment of the time series in the bottom left plot. The bottom right plot shows the bias.

Figure 4.4 illustrates the performance of the CPM KF for beam seas. The roll angle estimate for both cases is compared to the corresponding response for the IMU KF, while the roll rate estimates are compared to the raw roll rates from the gyro. The figure indicates that the roll angle and roll rate estimates obtained for the 5 second case are suitable for control, while the signals achieved for the 8 second case must not enter the feedback loop. It is seen that the roll angle and roll rate estimate in the left time series are smooth and not subject to phase lag, while the roll angle estimate in the right time series experience both offset and noise. Phase lag is also present for the roll rate estimate.

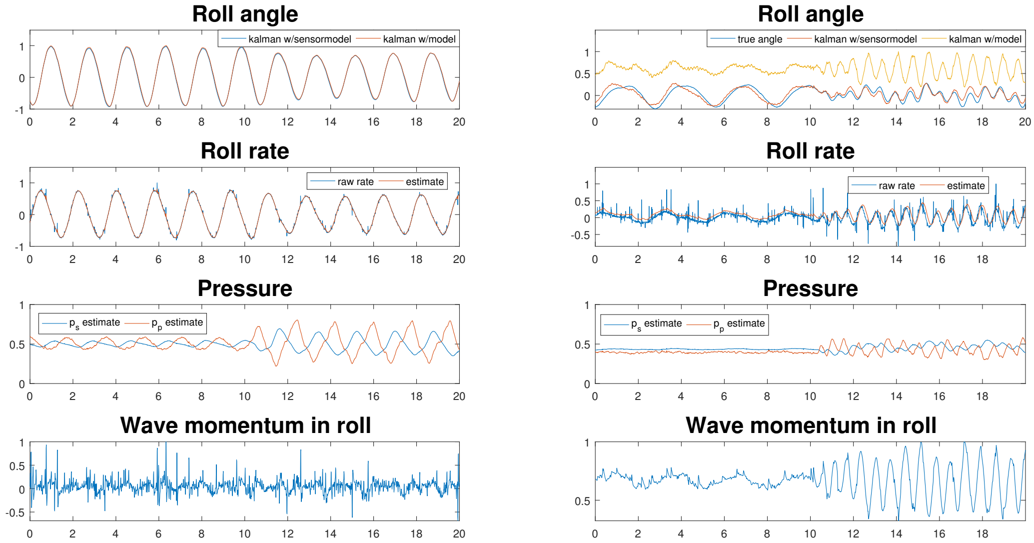

Figure 4.4: CPM KF response for beam seas with wave height 2 meter and period of 5 and 8 seconds, left and right figure, respectively.

The roll wave excitation moment estimates demonstrate that the wave estimation does not work as intended. The signal to noise ratio is to high, which implies that the wave dynamics are not caught. The right time series also illustrates that the wave excitation moment and pressure-induced moment for roll are not separated in a great manner. Both parameters have high-frequent dynamics which makes moment separation harder. For control on ($t > 10$), the peak-to-peak value of the excitation moment increases significantly compared to control off ($t < 10$). This does not make sense. The waves generated by the the wavemaker have constant wave height. Hence, the peak-to-peak value for the roll wave excitation moment should have been constant. Consequently, the mathematical model in the Kalman filter can not be trusted, meaning the diagonal elements of $\boldsymbol{Q}_d(k)$ must be reduced to obtain sensible estimates.
The effect by trusting the measurements more is shown in the Figure 4.4. For the 5 second case less trust is put in the model than for the 8 second case. As seen from the figure this leads to suitable feedback signals. Since the mathematical model is inaccurate, it was not considered beneficial to use the CPM KF further. Instead, the roll angle was obtained from the IMU KF and the roll rate was achieved by low-pass filtering the raw rate from the gyro.

From equation (2.11) it is seen that roll rate is coupled with wave excitation moment for roll, meaning that this parameter must be estimated accurate for the estimated roll rate to be valid. This can only be obtained when great separation between the pressure-induced roll moment and wave-induced roll moment is present. It is expected that the cushion forces, $\boldsymbol{\tau}_{cushion}$, cause problems. The observer exploits constant cushions areas and longitudinally and transverse lever arms which are not realistic. It was observed by eye during the model test period that these variables varies, heavily. Therefore, the estimated pressure-induced roll moment is not valid, inducing wrong wave excitation moment for roll.

4.3 Control System Design

A PID controller that is possible to tune real-time and an hybrid PID controller are designed in this section. The two controllers are able to damp motion induced from waves with various heights, periods and directions.

4.3.1 PID controller

The control law for the PID controller is written

$$\boldsymbol{u}(t) = -\boldsymbol{K}\hat{\boldsymbol{x}}(t), \tag{4.39}$$

where the input vector, $\boldsymbol{u}(t)$, the gain matrix, $\boldsymbol{K}$, and the a posteriori state estimate vector, $\hat{\boldsymbol{x}}(t)$, are written

$$\boldsymbol{u}(t) = \begin{bmatrix} \Delta A_s^{ctrl}(t) \\ \Delta A_p^{ctrl}(t) \end{bmatrix} \tag{4.40}$$

$$\boldsymbol{K} = \begin{bmatrix} k_{I_h} & k_{I_r} & 0 & k_{P_{hr}} & k_{P_{rr}} & 0 & 0 & 0 \\ k_{I_h} & -k_{I_r} & 0 & k_{P_{hr}} & -k_{P_{rr}} & 0 & 0 & 0 \end{bmatrix} \tag{4.41}$$

$$\hat{\boldsymbol{x}}(t) = \begin{bmatrix} \hat{x}_1(t) & \hat{x}_2(t) & \hat{x}_3(t) & \hat{x}_4(t) & \hat{x}_5(t) & \hat{x}_6(t) & \hat{x}_7(t) & \hat{x}_8(t) \end{bmatrix}^\top, \tag{4.42}$$

where the process states, $\boldsymbol{x}(t)$, are defined in Table 2.1. Here, the state estimations from the CPM KF are fed back to the controller. Note that the feedback signals which are used for control vary according to Figure 4.1. From (4.39)-(4.42) it is seen that a positive estimated roll momentum, $\hat{x}_5(t)$ will decrease the starboard commanded leakage area, $\Delta A_s^{ctrl}(t)$, and thereby increase the starboard air cushion pressure, $p_s(t)$, and vice versa for the port commanded leakage area, $\Delta A_p^{ctrl}(t)$, and the port cushion pressure, $p_p(t)$. Hence, the pressures will counteract roll motions, which is the purpose.

4.3.2 Hybrid PID Controller

Gains scheduling is applied for the hybrid PID controller. The controller structure is shown in equation (4.39). Multiple gain matrices, K_i for $i = 0°, 45°, 90°, 135°, 180°$, are utilized to damp motion induced from different wave directions. This is to increase roll damping in various headings. Initially, the idea was to estimate the wave direction, $\hat{\psi}_{wave}$, in the CPM KF and use a magnetometer to determine the heading of the Wave Craft, ψ_{vessel}. By exploiting the difference between these two angles, $\hat{\psi}_{wave} - \psi_{vessel}$, one of the gain matrices, K_i, would have been applied automatically dependent on the difference. The wave direction was surprisingly hard to estimate and no relevant literature was found regarding this subject. Therefore, and due to time constraints, the difference angle is set manually. This idea is also possible to utilize in full scale. Instead of setting the difference angle, the wave direction could be determined periodically. By measuring the wave heading, the difference angle can be computed. The wave direction is generally slowly-varying, meaning that this parameter does not need to be altered frequently. By utilizing online sea prognosis from e.g. DMI (Danmarks Meteorologiske Institut) convenient wave direction values can be determined. Their prognosis are propagated on an hour-to-hour basis and updated four times a day.

4.4 Stability Analysis

A stability investigation is performed to demonstrate that the air cushion pressures can not cause unstable vessel behaviour when choosing correct controller gain matrix, K. Thereafter, the stability of the system is analyzed when the vessel is exposed to waves. The stability analysis is based on Khalil (2002).

A reduced form of the control plant model expressed in equation (2.11) is exploited for the stability analysis. Only Roll and pressure dynamics are included, since damping of heave and pitch motions are not an objective for this project. A proportional controller is evaluated in the stability analysis. The nominal unperturbed system, which does not include disturbances, is expressed as

$$\dot{\tilde{\boldsymbol{x}}}(t) = \tilde{\boldsymbol{A}}\tilde{\boldsymbol{x}}(t) + \tilde{\boldsymbol{B}}\boldsymbol{u}(t), \tag{4.43}$$

where

Table 4.2: Reduced control plant model states, $\tilde{\boldsymbol{x}}(t)$

State	Description	Notation
$x_1(t)$	Roll angle	$\eta_4(t)$
$x_2(t)$	Roll angular momentum	$(I_{44} + A_{44})\dot{\eta}_4(t)$
$x_3(t)$	Dynamic starboard cushion pressure	$\mu_{u_s}(t)$
$x_4(t)$	Dynamic port cushion pressure	$\mu_{u_p}(t)$

$$\tilde{\boldsymbol{A}} = \begin{bmatrix} 0 & \frac{1}{I_{44}+A_{44}} & 0 & 0 \\ -C_{44} & -\frac{B_{44}}{I_{44}+A_{44}} & -y_{cp}A_c p_0 & y_{cp}A_c p_0 \\ 0 & \frac{y_{cp}\rho_{c0}A_c}{K1(I_{44}+A_{44})} & -\frac{K3}{K1} & 0 \\ 0 & -\frac{y_{cp}\rho_{c0}A_c}{K1(I_{44}+A_{44})} & 0 & -\frac{K3}{K1} \end{bmatrix} \tag{4.44}$$

$$\tilde{\boldsymbol{B}} = \begin{bmatrix} 0 & 0 \\ 0 & 0 \\ \frac{K2}{K1} & 0 \\ 0 & \frac{K2}{K1} \end{bmatrix}. \tag{4.45}$$

By choosing the control law

$$\boldsymbol{u}(t) = -\tilde{\boldsymbol{K}}\dot{\tilde{\boldsymbol{x}}}(t), \tag{4.46}$$

where

$$\tilde{\boldsymbol{K}} = \begin{bmatrix} 0 & k_{p_s} & 0 & 0 \\ 0 & -k_{p_p} & 0 & 0 \end{bmatrix}, \tag{4.47}$$

the closed-loop system can be written according to

$$\dot{\tilde{\boldsymbol{x}}}(t) = (\tilde{\boldsymbol{A}} - \tilde{\boldsymbol{B}}\tilde{\boldsymbol{K}})\tilde{\boldsymbol{x}}(t) = \boldsymbol{A}_{cl}\tilde{\boldsymbol{x}}(t), \tag{4.48}$$

where the closed-loop matrix is written

$$\boldsymbol{A}_{cl} = \begin{bmatrix} 0 & \frac{1}{I_{44}+A_{44}} & 0 & 0 \\ -C_{44} & -\frac{B_{44}}{I_{44}+A_{44}} & -y_{cp}A_c p_0 & y_{cp}A_c p_0 \\ 0 & \frac{y_{cp}\rho_{c0}A_c - K2k_{p_s}(A44+I_{44})}{K1(A_{44}+I_{44})} & -\frac{K3}{K1} & 0 \\ 0 & -\frac{y_{cp}\rho_{c0}A_c - K2k_{p_p}(A44+I_{44})}{K1(A44+I_{44})} & 0 & -\frac{K3}{K1} \end{bmatrix}. \tag{4.49}$$

The system will converge to its equilibrium states, $\boldsymbol{x}_0$, exponential fast, when the closed-loop matrix, $\boldsymbol{A}_{cl}$, is Hurwitz. This occurs when all eigenvalues of $\boldsymbol{A}_{cl}$ have negative real part, i.e. $\Re(\lambda_i) < 0$. When the closed-loop matrix is Hurwitz, asymptotically stability of the origin is guaranteed. However, since the system is linear, the origin of (4.43) is globally exponential stable (GES). This can be proofed by considering the quadratic Lyapunov candidate

$$V(\tilde{\boldsymbol{x}}) = \tilde{\boldsymbol{x}}^\top \boldsymbol{P}\tilde{\boldsymbol{x}}, \tag{4.50}$$

where $\boldsymbol{P}$ is a real symmetric positive definite matrix, $\boldsymbol{P} = \boldsymbol{P}^\top > 0$. The derivative of V along the trajectories of the linear system (4.43) is given by

$$\dot{V}(\tilde{\boldsymbol{x}}) = \tilde{\boldsymbol{x}}^\top \boldsymbol{P}\dot{\tilde{\boldsymbol{x}}} + \dot{\tilde{\boldsymbol{x}}}^\top \boldsymbol{P}\tilde{\boldsymbol{x}} = \tilde{\boldsymbol{x}}^\top(\boldsymbol{P}\boldsymbol{A}_{cl} + \boldsymbol{A}_{cl}^\top\boldsymbol{P})\tilde{\boldsymbol{x}} = -\tilde{\boldsymbol{x}}^\top\boldsymbol{Q}\tilde{\boldsymbol{x}}, \tag{4.51}$$

where $\boldsymbol{Q}$ is a symmetric matrix defined by

$$\boldsymbol{P}\boldsymbol{A}_{cl} + \boldsymbol{A}_{cl}^\top\boldsymbol{P} = -\boldsymbol{Q}. \tag{4.52}$$

Equation (4.52) is known the Lyapunov equation. According to Khalil (2002), $\boldsymbol{A}_{cl}$ is Hurwitz if and only if for any positive definite symmetric matrix $\boldsymbol{Q} = \boldsymbol{Q}^\top > 0$, there exist a positive definite symmetric matrix $\boldsymbol{P}$ that satisfies the Lyapunov equation (4.52). In addition, $\boldsymbol{P}$ is a unique solution of (4.52). $\boldsymbol{P}$ and $\boldsymbol{Q}$ are chosen to be diagonal matrices with (p_1, p_2, p_3, p_4) and (q_1, q_2, q_3, q_4), respectively, on the main diagonal. A solution of (4.52) was found to be

$$p_1 = 1 \tag{4.53}$$

$$p_2 = C_{44}(A_{44} + I_{44}) \tag{4.54}$$

$$p_3 = \frac{a_{cl_{32}} C_{44}(A_{44} + I_{44})}{y_{cp} A_c p_0} \tag{4.55}$$

$$p_4 = \frac{a_{cl_{42}} C_{44}(A_{44} + I_{44})}{y_{cp} A_c p_0} \tag{4.56}$$

$$q_1 = 0 \tag{4.57}$$

$$q_2 = 2B_{44}C_{44} \tag{4.58}$$

$$q_3 = \frac{2p_3 K3}{K1} \tag{4.59}$$

$$q_4 = \frac{2p_4 K3}{K1}. \tag{4.60}$$

Since all of the terms have positive interpretation, $\boldsymbol{P} = \boldsymbol{P}^\top > 0$ and $\boldsymbol{Q} = \boldsymbol{Q}^\top \geq 0$ when $a_{cl_{32}} > 0$ and $a_{cl_{42}} > 0$, which occurs for

$$k_{p_s} < \frac{y_{cp} \rho_{c0} A_c}{K2(A_{44} + I_{44})} \approx 0 \tag{4.61}$$

$$k_{p_p} > \frac{y_{cp} \rho_{c0} A_c}{K2(A_{44} + I_{44})} \approx 0. \tag{4.62}$$

$\boldsymbol{Q}$ is not a positive definite matrix, therefore exponential stability of the origin can not be claimed. However, by utilizing LaSalle's invariance principle, it can be proved that the origin is GES. From (4.57) it is seen that $q_1 = 0$, which implies that it can not be guaranteed that the roll angle approaches its origin when time goes to infinity. Hence, the reduced state vector can be written $\tilde{\boldsymbol{x}} = \begin{bmatrix} x_1 & 0 & 0 & 0 \end{bmatrix}^\top$ when time approaches infinity. From (4.48) it is seen that $\dot{x}_2 = 0$ only if $x_1 = 0$. Therefore, $\boldsymbol{A}_{cl}$ is Hurwitz, and all states converge exponential fast to their origins. Hence, it is proved that by choosing the proportional gains for the commanded starboard and port vent valve positions according to (4.61) and (4.62), respectively, the roll angle, roll rate and air cushion pressures can not be driven unstable.

In order to validate that the wave-induced disturbances do not lead to an unstable system, a stability analysis of the perturbed closed-loop system is performed. The perturbed system, which include disturbances, can be written

$$\dot{\tilde{\boldsymbol{x}}}(t) = \boldsymbol{A}_{cl}\tilde{\boldsymbol{x}}(t) + \tilde{\boldsymbol{E}}\tilde{\boldsymbol{v}}(t), \tag{4.63}$$

where

$$\tilde{\boldsymbol{E}} = \begin{bmatrix} 0 & 0 & 0 \\ 1 & 0 & 0 \\ 0 & \frac{\rho_{c0}}{K1} & 0 \\ 0 & 0 & \frac{\rho_{c0}}{K1} \end{bmatrix}, \tag{4.64}$$

and the disturbance vector is defined $\tilde{\boldsymbol{v}} = \begin{bmatrix} F_4^e(t) & \dot{V}_{0_s}(t) & \dot{V}_{0_p}(t) \end{bmatrix}^\top$. Since the perturbations are non-vanishing, it is not expected that the states converge to their origin when time goes to infinity. However, it can be shown that the solution, $\tilde{\boldsymbol{x}}(t)$, will be ultimately bounded by a small bound, b, if the perturbation term, $\tilde{\boldsymbol{E}}\tilde{\boldsymbol{v}}$, is small in some sense (Khalil, 2002). By utilizing (4.50) and (4.63), equation (4.51) is written

$$\dot{V}(\tilde{\boldsymbol{x}}) = -\tilde{\boldsymbol{x}}^\top \boldsymbol{Q}\tilde{\boldsymbol{x}} + 2\tilde{\boldsymbol{x}}^\top \boldsymbol{P}\tilde{\boldsymbol{E}}\tilde{\boldsymbol{v}} < 0. \tag{4.65}$$

The inequality in equation (4.65) holds if the disturbance term is chosen according to

$$\|\tilde{\boldsymbol{E}}\tilde{\boldsymbol{v}}\| < \|\boldsymbol{T}\tilde{\boldsymbol{x}}\|, \tag{4.66}$$

where

$$2\boldsymbol{P}\boldsymbol{T} < \boldsymbol{Q}. \tag{4.67}$$

Then the perturbation term is bounded. The diagonal matrix $\boldsymbol{T}$ is determined according to

$$\boldsymbol{T} = \begin{bmatrix} 0 & 0 & 0 & 0 \\ 0 & \frac{B_{44}}{A_{44}+I_{44}} & 0 & 0 \\ 0 & 0 & \frac{K3}{K1} & 0 \\ 0 & 0 & 0 & \frac{K3}{K1} \end{bmatrix}. \tag{4.68}$$

From Lemma 9.2 in Khalil (2002) it follows that the solution of the perturbed system (4.63) is ultimately bounded by b, i.e. $\|\tilde{\boldsymbol{x}}(t)\| < b$.

Hence, when choosing appropriate controller gains and the vessel is subject to a roll wave excitation moment below a certain limit, the system states are ultimately bounded.

Chapter 5

Implementation

5.1 Software

MATLAB and Simulink are used for creating simulation models, control system models and also plotting results. VeriStand is acting as an interface between the host PC and the controller.

5.1.1 MATLAB and Simulink

Simulink is exploited to simulate the control plant model and the process plant model in order to create and verify the control system and observer design. Simulations of the behaviour of the Wave Craft are also obtained from Simulink. It utilizes a graphical block based approach in order to visualize and hence simplifying the implementation of the differential equations describing the dynamics. MATLAB is used for generating plots and creating scripts for specifying parameters and calculating variables.

Figure 5.1 shows the control hierarchy that is used for real-time control in VeriStand.

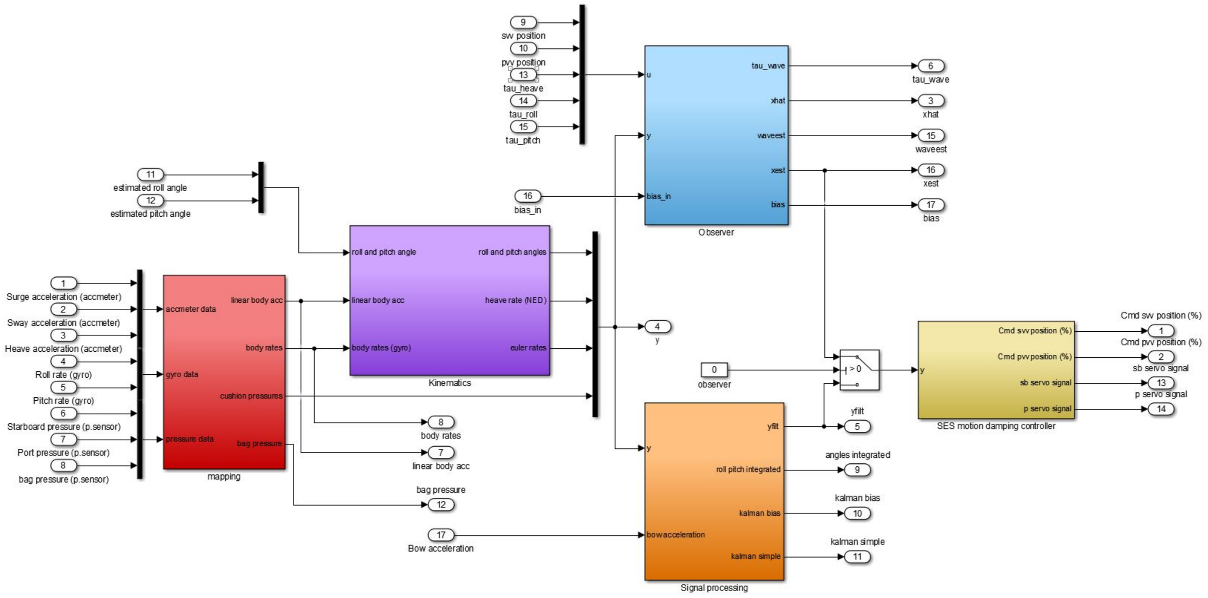

Figure 5.1: Implemented control system

- The Mapping block contains the mapping from sensor voltages to the physical quantities and the calibration routine.
- The Kinematics block includes the kinematic transformations from the BODY frame, where the measurements take place, to the NED frame.
- The Observer block implements the CPM KF.
- The Signal Processing block contains high-pass and low-pass filters, and also the IMU KF.
- The SES motion damping controller block implements the two control systems, where it is possible to switch between the hybrid and the tunable controller.

For the implemented control system design it was highly emphasized that switching between different feedback signals and controllers should be possible. VeriStand does not accept algebraic loops, meaning that signals can not be fed back in the Simulink diagram. Hence, mappings must be executed in VeriStand. The subsystem for each block in Figure 5.1 is found in Appendix C, followed by a brief description.

5.1.2 VeriStand

VeriStand is a tool developed by National Instruments providing an interface for communication between a host PC and real-time embedded hardware. The main reason for choosing VeriStand is the possibility of implementing third party simulation models on the controller, thus making it possible to use a control system model developed in Simulink in order to simplify the implementation.

Setup

When a project is created in Veristand, the workspace is displayed. This is where the project is executed on the CompactRIO and where the different project files can be accessed. The *system definition file* includes and connects all the elements used for a specific setup. Three items in this file has to be created; FPGA configuration file, a simulation model and a connection mapping:

- The *FPGA configuration file* describes the setup of the CompactRIO with a specific configuration of installed I/O modules. This file was set up with LabVIEW FPGA by assistance from Sintef Ocean personnel.
- The *simulation model* could be any compiled model supported by VeriStand, a compiled simulink model of the controller for this project.

- The *connection mapping* is a module in the system definition file that creates mappings between the I/Os described in the FPGA Configuration File and the simulation model.

Real-time control and logging is implemented in a user interface shown in Figure 5.2. VeriStand provides a module for logging data real-time, which outputs a .tdms log file. In order to plot this data in MATLAB, a transformation script is utilized to convert the .tdms file to a .mat file.

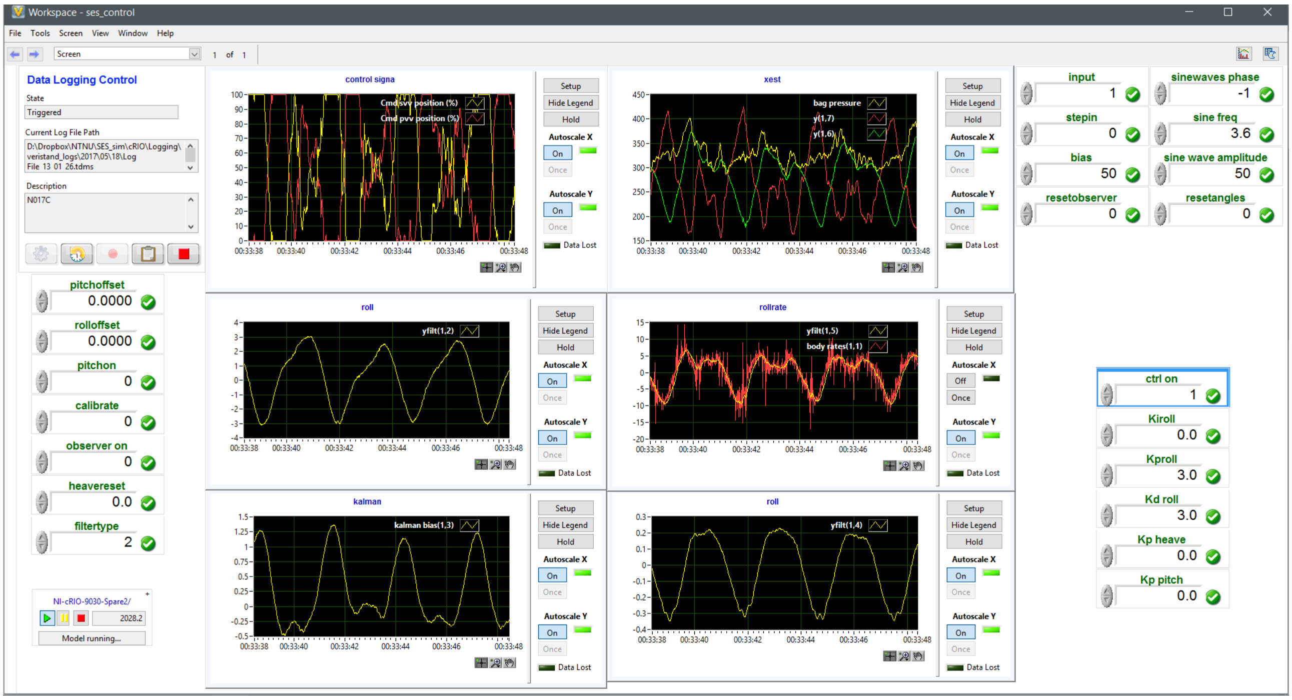

State: Triggered

Current Log File Path: D:\Dropbox\NTNU\SES_sim\cRIO\Logging\veristand_logs\2017\05\18\Log File 13 01 26.tdms

Description: N017C

pitchoffset 0.0000

rolloffset 0.0000

pitchon 0

calibrate 0

observer on 0

heavereset 0.0

filtertype 2

NI-cRIO-9030-Spare2/ 2028.2

Model running...

input 1

sinewaves phase -1

stepin 0

sine freq 3.6

bias 50

sine wave amplitude 50

resetobserver 0

resetangles 0

ctrl on 1

Kiroll 0.0

Kproll 3.0

Kd roll 3.0

Kp heave 0.0

Kp pitch 0.0

Figure 5.2: VeriStand user interface for real-time control.

5.2 Hardware

The main hardware components and their communication flow are illustrated in Figure 5.3. The implemented instrumentation is shown in Figure 5.4.

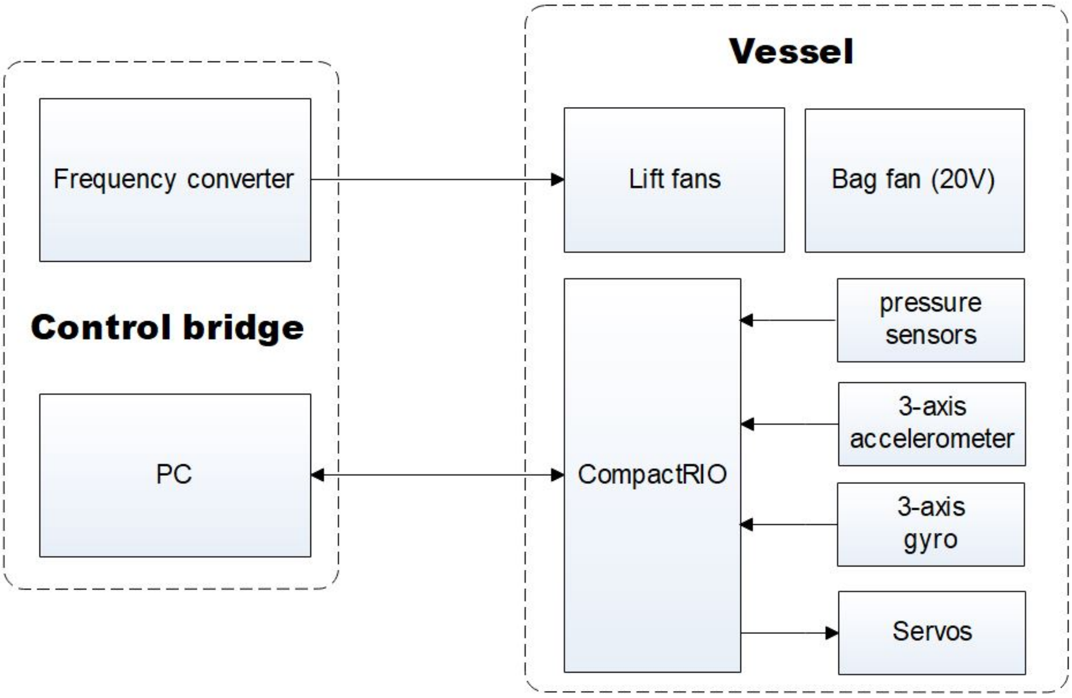

Figure 5.3: Communication diagram for the hardware components.

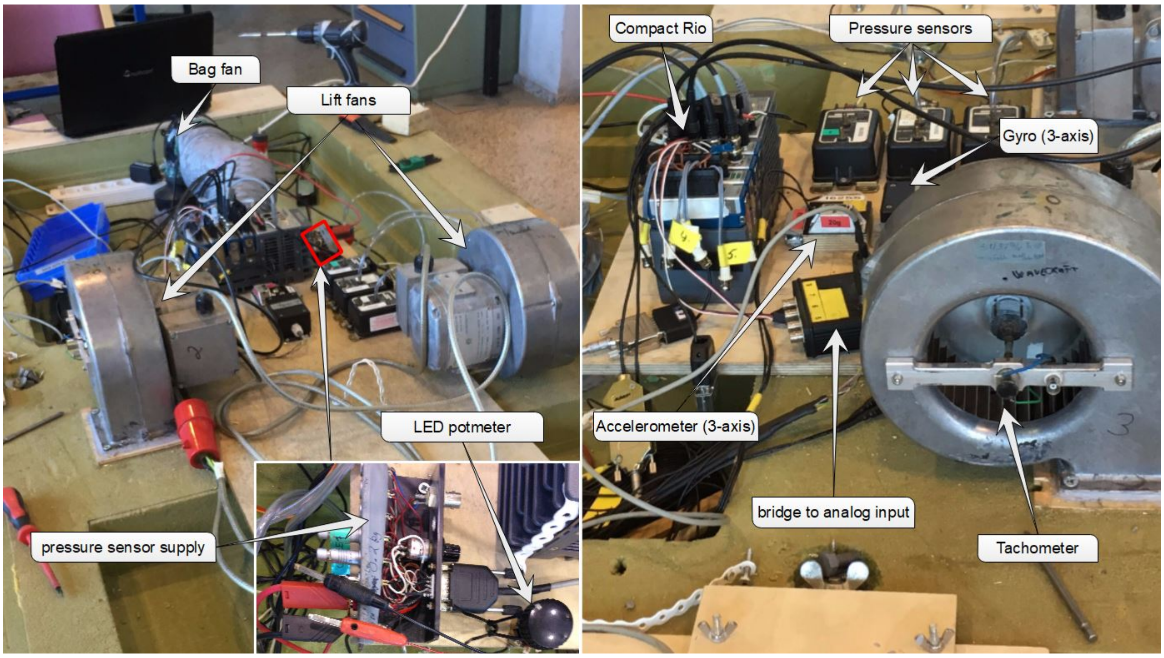

Figure 5.4: Hardware implementation.

5.2.1 CompactRIO

The control system is implemented on the CompactRIO from National Instruments shown in Figure 5.5. The main reason for choosing this controller, is to ease the implementation, especially when it comes to real-time control, and data logging. The CompactRIO is connected to a PC over ethernet (5). The analog gyro and pressure sensors are connected to the analog input (2), while the accelerometer is connected to the analog bridge input (1). The servos are connected to the digital output (3) and controlled by using a pulse width modulated (PWM) signal.

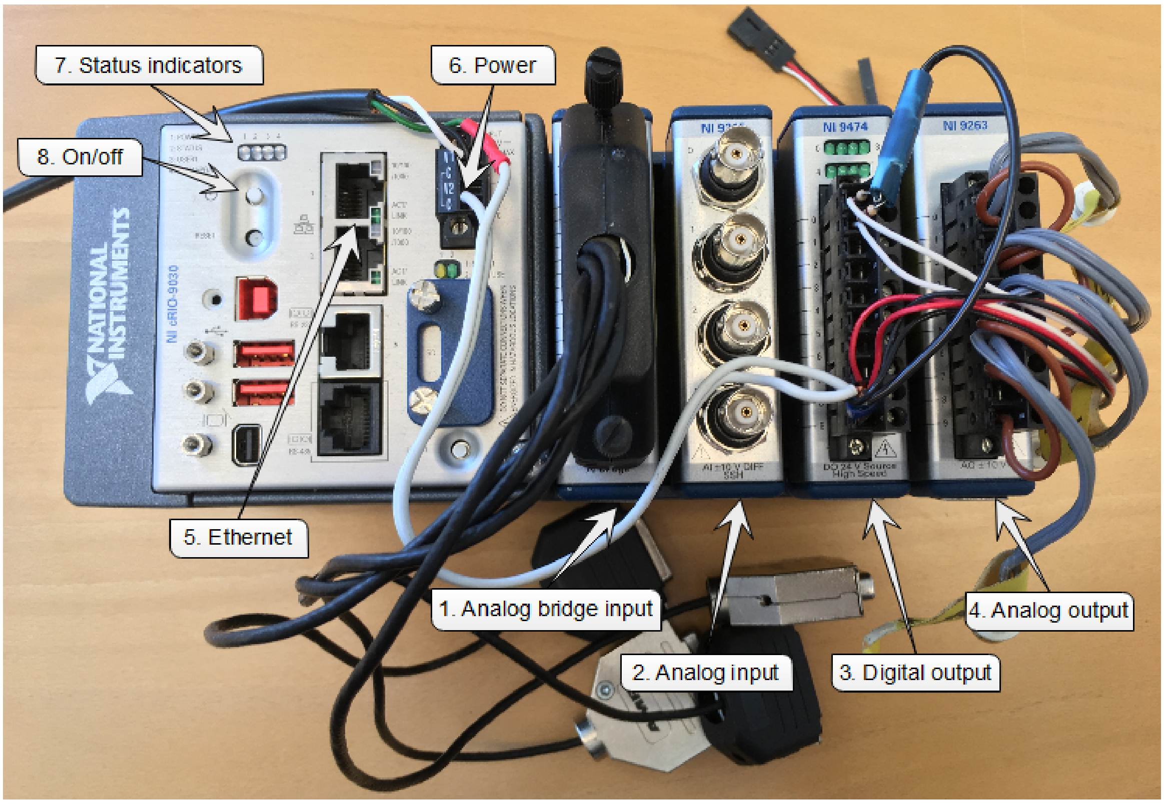

Figure 5.5: CompactRIO setup.

5.2.2 Sensor Calibration

Exclusively, analog sensors have been implemented. A linear relationships between the raw output voltage, V_{out}, and its corresponding physical measurement have been established for every sensor. This relationship is given by

$$measurement = slope * V_{out} + bias, \tag{5.1}$$

where the *bias* is removed by using a calibration routine in Simulink. This is done by averaging the sensor output over a fixed number of samples. The *slope*, which is the mapping from voltage to measurement, is identified for each sensor by using different calibration strategies. These are described in detail below. All of these strategies has shown that a linear relationship is sufficient to describe the characteristics of the sensors for the limited domain the vessel is operating. The slopes are computed by using the MATLAB command `regression` on a fixed number of measurements.

Gyro

The calibration of the gyro was done by exploiting a ship roll bench. For this mechanism, a roll amplitude and frequency are chosen in a UI. By differentiating the input signal from the UI, the roll angle propagation, and comparing it to the output voltage of the gyro, the gyro scaling factors are determined. The input is chosen as low frequency sine waves according to

$$\phi_{in} = 10\sin(\frac{2\pi}{T}t) \ \text{ for } \ T = \{3,\ 5,\ 8,\ 10\}. \tag{5.2}$$

This method was utilized to determine the roll and pitch angular velocity for the gyro. The slopes is seen in Figure 5.6.

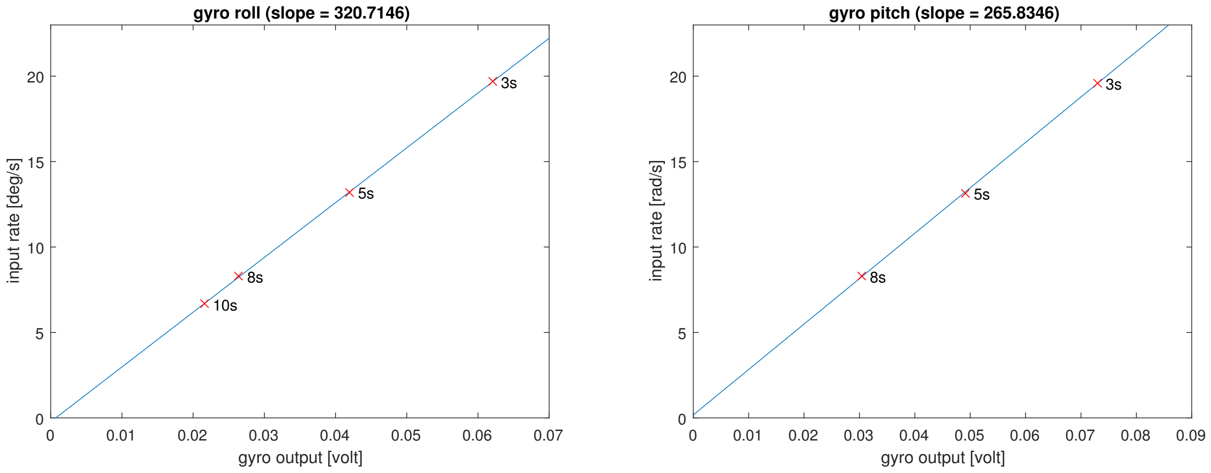

Figure 5.6: Gyro calibration.

Tachometer

The slope of the tachometer is found by measuring the RPS at different frequencies and plotting this versus the output voltage as shown in Figure 5.7.

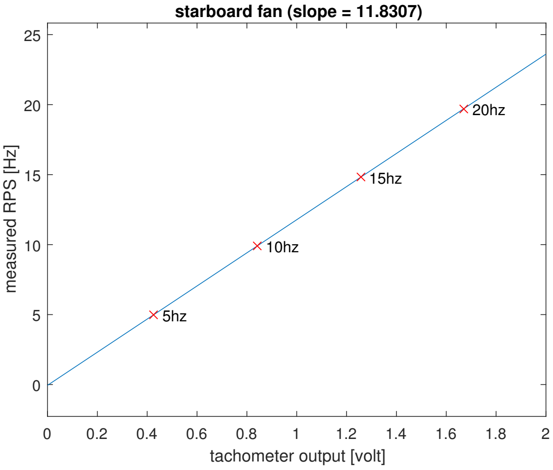

Figure 5.7: Tachometer calibration.

Accelerometer

The 3-axis accelerometer is calibrated by inspecting the output values of each of the accelerometer axis for two different scenarios. When one axis is horizontally aligned with the north-east plane, the output should be zero. The actual reading in this scenario will thus be the accelerometer bias. In order to find the linear relationship between voltage and acceleration, the accelerometer axis is vertically aligned with the down axis. This ensures that all the gravitational acceleration is red along this axis. Therefore, the acceleration measurement for this axis is scaled to equal $-9.81\ m/s^2$.

Pressure sensors

The pressure sensors have two detectors, where a measured pressure is compared with a reference pressure, typically the atmospheric pressure. The bias is found by using both detectors to measure the atmospheric pressure. To find the scale factor to form a linear relationship between pressure and voltage, the sensors are calibrated using a tank of water and a tube as shown in Figure 5.8. The pressure is calculated at various heights according to $p = \rho g h$. The pressure responses are compared to the corresponding output voltages of the pressure sensors shown in Figure 5.9a - 5.9c.

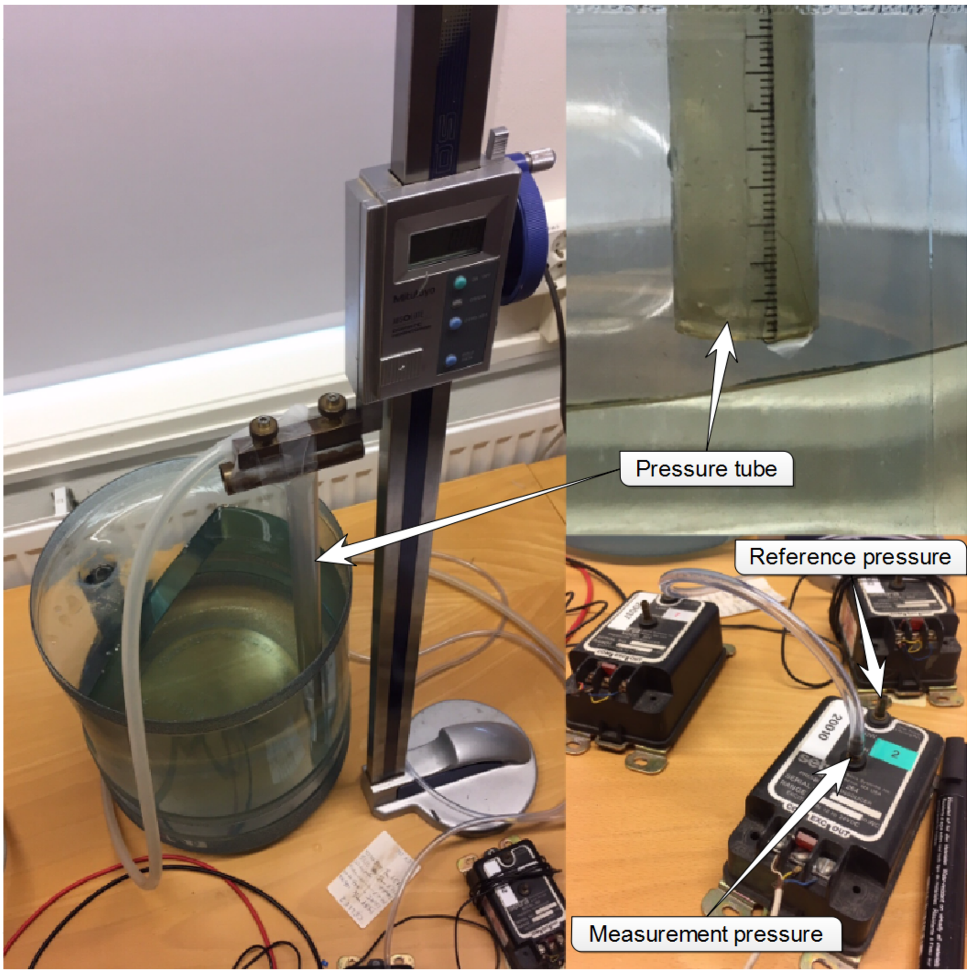

Figure 5.8: Pressure sensor calibration setup.

5.2.3 Servo setup

As described in Bua and Vamråk (2016), servo communicating problems occurred since the servos are not able to apply a big enough load on the CompactRIO. This was solved by connecting a pull-down resistor to the servo signal lines, hence increasing the load. The servos were scaled in VeriStand to operate according to 0-100% duty cycle corresponding to 0-100% vent valve opening. The servo shafts implemented at project take over were made of brass. One of them was broken, while the other one experienced a torsion fracture during the model tests. Currently, the port and starboard servo shaft is made of steel and brass, respectively. The port servo setup is shown in Figure 5.10.

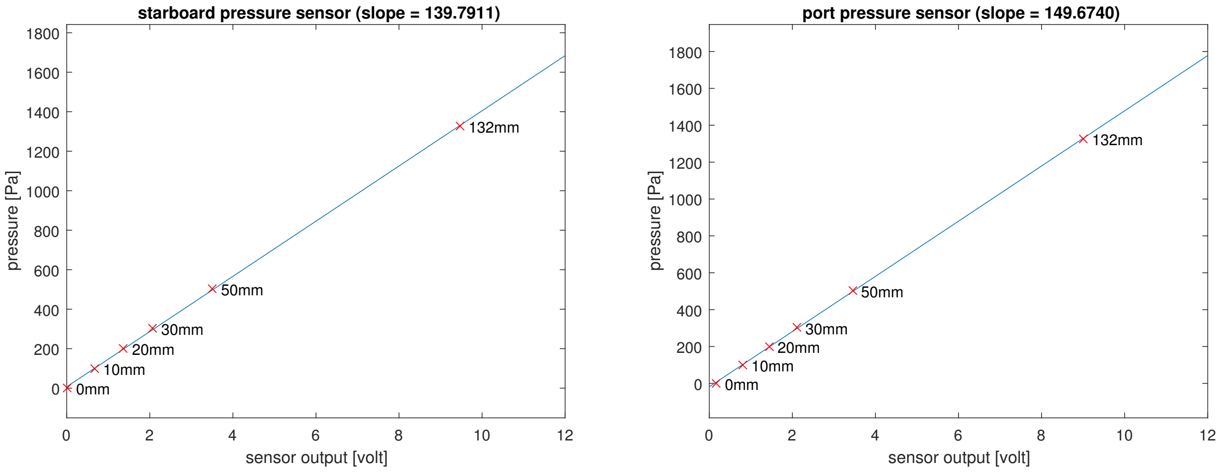

(a) Starboard pressure calibration.

(b) Port pressure calibration.

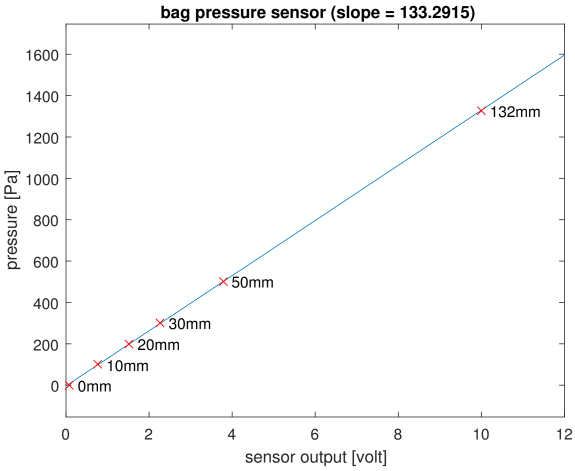

(c) Bag pressure calibration.

Figure 5.9: Pressure sensor calibration.

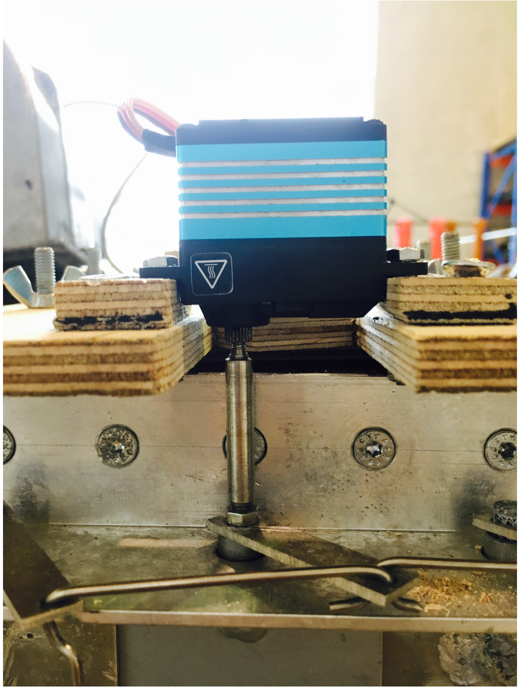

Figure 5.10: Port servo setup. A steel shaft is exploited to connect the middle vent valve blade and the servo.

In order to verify that the vent valves are able to operate across the full bandwidth of the system, a servo response test was carried out. The position of the vent valves is measured using a pull cord displacement sensor as shown in Figure 5.11.

Figure 5.11: Servo test setup with pull cord displacement sensor.

The commanded vent valve signal was a chirp signal, a sine sweep with amplitude and bias of 50 %, i.e. the vent valve utilized its entire operating area, 0-100 %. The chirp signal covers the frequency range $0.1 - 10$ Hz over 2 minutes. Figure 5.12 shows the comparison of the commanded and actual vent valve position.

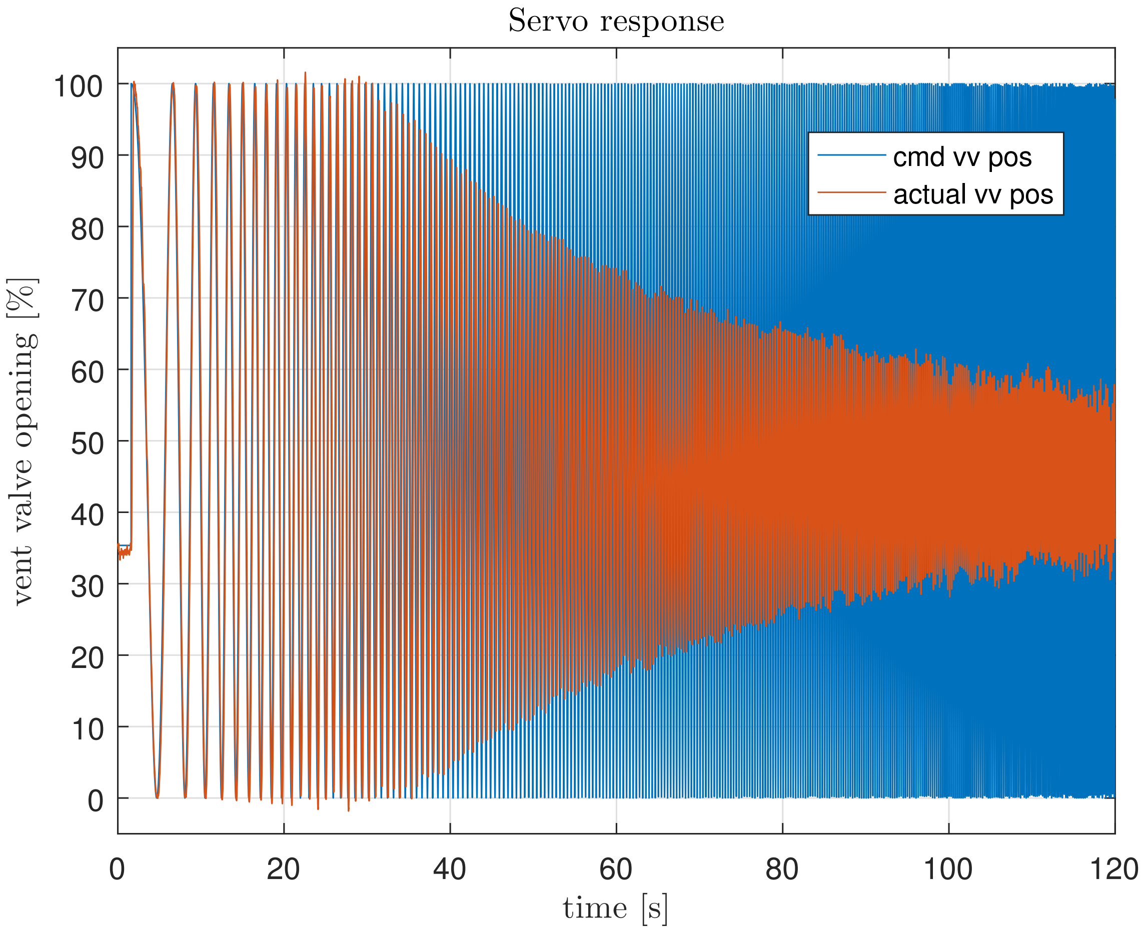

Figure 5.12: Servo response.

The frequency response of the servo system was determined by using the system identification toolbox in MATLAB. A transfer function from the commanded to the measured vent valve position is written according to

$$H(s) = \frac{1.205s + 163.1}{s^2 + 16.3s + 175.4}. \tag{5.3}$$

The frequency response of the transfer function is shown in Figure 5.13. The cut-off frequency of the system occurs at -3 dB. This corresponds to a frequency of 2.28 Hz, which is outside the bandwidth of the system. However, at 0.7 Hz, which correspond to a period of 4 seconds full scale, the servo system experience a phase lag of approximately 23 degrees, meaning that major phase lag may occur when damping high-frequent wave-induced motion. Note that the pull cord displacement sensor adds some resistance to the servo system, i.e. the actual cut-off frequency may be higher than the experienced one.

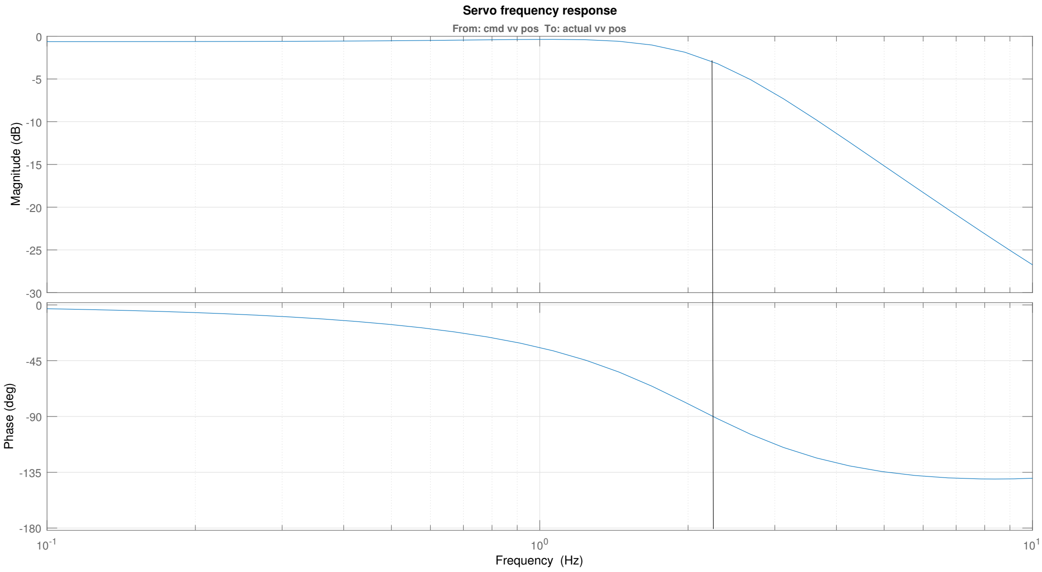

Figure 5.13: Frequency response for the port servo system.

5.3 Separating wall

The implemented separating wall is shown in Figure 5.14. It is seen from the figure that the wall is fixed to the wet deck, aft bag and the middle finger shirt. From the upper left picture it is seen that a camera was mounted near the bow to catch the behaviour of the middle wall when the vessel is subject to waves. The upper right picture illustrates the bag fan inlet, while the lower left and right picture show where the middle wall is fixed to the aft bag and middle finger shirt, respectively.

Figure 5.14: Current separating wall implementation

5.3.1 Design

In order to minimize the tear and wear on the separating wall, height calculations were done. It is desirable to damp roll motions when the vessel is at zero speed, meaning that a part of the middle wall must be under the water line at all times when the pressures are in anti-phase. If not, air leakages will occur between the starboard and port chamber. This will lead to less pressure potential between the cushion pressures, which will reduce the maximum roll moment the pressures are able to induce. Consequently, the roll damping percentages achievable will decrease.

However, due to wear and tear, it is required that the separating wall is over the water line during transit, where both vent valves are fully closed. According to the general arrangements for the Wave Craft included in Appendix B, the draught of the hull is 0.8 meter for maximum pressure on-cushion and 3.0 meter off-cushion.

Simulations imply that the maximum heave displacement only can be obtained when the vent valves operate in phase. Then the pressures and cushion areas in both chambers are assumed equal. By these assumptions, the pressure-induced heave forces in both chambers are equivalent. When the pressures increase, the entire middle wall will, at some point in time, be located above the water line. Then a gap between the bottom of the middle wall and the water line occurs, which leads to a cushion pressure, P_u, that is present in both chambers. This pressure works on the total air cushion area.

During roll damping, the vent valves, and thereby also the pressures, operate in anti-phase around some bias value. A typical roll damping operation exploits 50 % bias opening, where the vent valves are commanded ±50 % in anti-phase around the bias opening to compensate for wave-induced motions. Hence, the starboard and port pressure-induced forces, F_s and F_p, respectively, differ. Since the Wave Craft response from the cushion pressures to positions can be expressed linearly, it is assumed that some part of the middle wall is always located below the water line during roll damping.

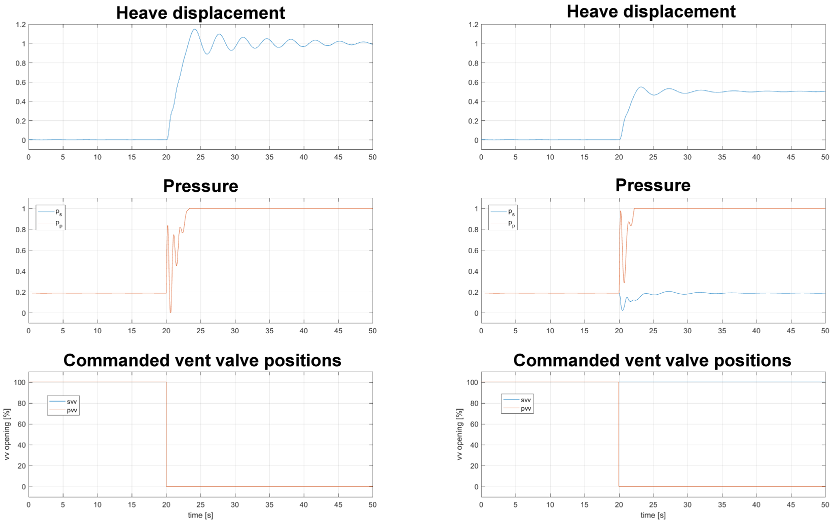

Figure 5.15: Heave displacement response for both vv fully closed (left figure) and *svv* fully closed and *pvv* fully open (right figure)

Figure 5.15 is obtained by simulating the nonlinear process plant model. The heave displacement achieved by commanding the starboard and port vent valves in phase and anti-phase are shown. The time series confirms that the heave displacement can be expressed linearly subject to air cushion pressure. By commanding the vent valves in anti-phase, *svv* fully closed and *pvv* fully open, it is seen that the heave displacement obtained is approximately half of the displacement achieved for both vent valves fully closed, i.e. vent valves in phase.

5.3.2 Implementation

The bottom of the middle wall was implemented 13.8 cm above the bottom of the side hulls for the vertical direction. This corresponds to 1.1 meter full scale. From the general arrangements it is seen that the height of the air cushion is approximately 3.5 meter at the aft bag location and 5.0 meter at the bow location. By measuring the height of the side hulls inside the air cushions with 20 cm intervals for the model vessel, the air cushion height was found to increase linearly towards the bow. Consequently, the height of the middle wall was designed proportional to the longitudinally position.

Figure 5.16: Separating wall parts.

In order to fix the separating wall to the wet deck a wooden beam was utilized as a fastener to provide better grip for the screws. This is seen in Figure 5.16. Another wooden beam with equal width, seen in the right picture in Figure 5.16, was fixed inside the middle wall. This beam is located along the bottom of the separating wall in longitudinally direction. It is exploited to keep the lower and upper width off the wall equal. When some part of the separating wall is located below the water line, the buoyancy force acting on the wooden beam from the water will try to push the wall up. This is a downside. However, the separating wall is fixed to the aft bag and middle finger shirt by using double-sided and duct tape. This will work against the buoyancy force and thereby maintain its desired location. A heavier material could have been used to keep the width of the lower part of the wall and also contribute to retain it below the water line. This would have led to a vertical force downwards from the separating wall, meaning that less heave displacement could have been generated.

The purpose of the T-duct shown in the left picture in Figure 5.16 is to ensure that the bag fan exploits the highest air cushion pressure to pressurize the aft bag and separating wall. The wooden plate located inside the duct separates the starboard and port air cushion pressure. Silicon and sealing compound were used to ensure that no leakages along and below the plate occur. The plate is present through the entire T-duct. The upper part of the plate is located some centimeters into the hull.

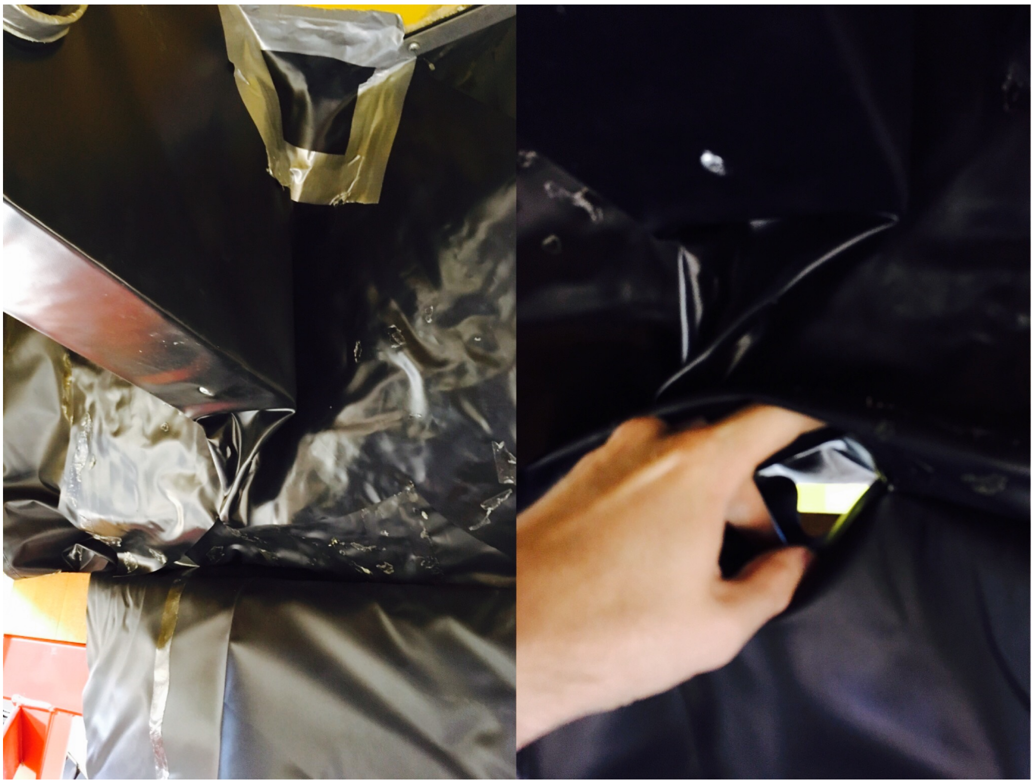

Figure 5.17: Separating wall modifications

5.3.3 Modifications

During the model test period multiple modifications were done related to the separating wall. Initially, some of its material was taped to the aft bag on the left and right hand side and below the wall as illustrated in Figure 5.14. It was considered to be of great importance to obtain a completely airtight connection between the wall and aft bag. It was desirable to prevent both air and water leakages. When the model vessel was beached, a major hole between the separating wall and aft bag connection was discovered. It was located below the wall. Due to its location and size, water leakages were expected to have caused it.
Initially, the separating wall was designed to not drain any water. This was a mistake. Water always choose the easiest way to escape, meaning that the double-sided tape was not strong enough to prevent leakage. It is considered disadvantageous to not drain the wall due to wear and tear. If the water is prevented from escaping from the separating wall, this will lead to greater stress at the wet deck connection for fully closed vent valves, i.e. when the entire separating wall is above the water line. Therefore, the connection between the separating wall and the aft bag was modified to tolerate drainage of water. Figure 5.17 illustrates the actions that were done. An additional material flap was fixed beneath the aft bag as seen in the left

picture. A hole was implemented at the center of the connection line meant for water leakage as illustrated in the right picture. This hole was located near the holes in the aft bag, meaning that by draining the aft bag, the separating wall will also be drained. This is done by commanding the vent valves fully closed, without running the bag fan. Then the pressures will lift the vessel up from the water, while the aft bag is laying on the water line, unpressurized. The flap was also fixed both on the right and left hand side of the separating wall to prevent water leakages in multiple directions. A water channel was implemented along the center of the flap to lead the water from the separating wall to the hole.

The wooden plate located inside the T-duct was extended. This was due to pressure differences that occurred during the model test phase. A volumetric air flow from the air cushion with the higher pressure to the chamber with the lower pressure was suspected to be present above the plate. By extending the wooden plate, the starboard and port air cushions pressures were separated closer to the bag fan. Due to the suck from the fan, it was expected that this would decrease the possibility of air flows between the chambers over the wooden plate. However, this modification did not lead to that any significant pressure differences were discovered.

5.4 Normalization and Scaling

The response obtained from model tests and simulations are normalized between 1 and -1. The first and latter represent the maximum and minimum experienced value, respectively, for a given state during a time series. This is done due to commercial purposes and does not affect the performance identification of the roll damping control system, which is determined by relative roll damping percentages. This is done by comparing the angular displacement for the roll angle for control off, $ctrl_{off}$, and control on, $ctrl_{on}$. Then the relative damping percentage is given by (Fossen, 2011)

$$\text{Roll reduction} = \frac{\sigma_{ctrl_{off}} - \sigma_{ctrl_{on}}}{\sigma_{ctrl_{off}}} \times 100\ \%, \tag{5.4}$$

where $\sigma_{ctrl_{on}}$ and $\sigma_{ctrl_{off}}$ are the standard deviation for the roll angle for control on and off, respectively.

The scaling factor for the model vessel is 8. Various parameters for the model scale vessel are compared to the full scale vessel in Table 5.1. Some of these parameters were utilized when comparing the model test response to the full scale simulation response in Section 6.3. Additionally, the CPM KF was initially designed for the full scale vessel. Later, the observer was constructed to perform state estimation for the model scale vessel. This was done by scaling all the terms of the control plant model in equation (2.11). The force and moment scaling presented in Table 5.1 were exploited.

Table 5.1: Scaled parameters

Parameter	Full scale	Model scale
Length [m]	1	$\frac{1}{8}$
Time [s]	1	$\frac{1}{\sqrt{8}}$
Mass [kg]	1	$\frac{1}{8^3}$
Force [N]	1	$\frac{1}{8^3}$
Moment [Nm]	1	$\frac{1}{8^4}$

Chapter 6

Results

In this chapter, simulations of the linear control plant model (CPM) and the nonlinear process plant model (PPM) are presented and analyzed. The model tests performed on the 1:8 model of the Wave Craft is included in this chapter. In order to validate both simulators, their response is compared to the model tests time series.

6.1 Simulation

Both the control plant model and the process plant model that are used in the simulations are based on already existing simulators. The CPM utilizes known equations for heave and pitch motion, but differs from earlier simulators since the equation for roll motion is introduced together with the equations for starboard and port air cushion pressure. The process plant model established at Umoe Mandal is further developed to include the separating wall and roll motion dynamics.

Initially, roll motions were generated in the absence of waves. This was done to identify the maximum roll angle the Wave Craft can theoretically generate using the split cushion pressure control regime. Thereafter, roll motion was damped for different seas states. It was also investigated if it is possible to damp roll and heave motions for beam and quartering seas, simultaneously.

6.1.1 Roll Generation

In order to verify that the simulation models are correct, one would expect the craft to roll when the vent valves are commanded in anti-phase, i. e. starboard vent valve, *svv*, fully closed and port vent valve, *pvv*, fully open, or vice versa. The roll generation tests were performed in absence of waves, to validate that the pressures are able to induce roll motions. The following generation tests were executed

- Case 1 - step commanded vent valve signals: *svv* fully closed, *pvv* fully open, then vice versa.

- Case 2 - sine commanded vent valve signals: svv in anti-phase with pvv. 50 % bias vv opening, 50 % amplitude and 5 seconds period for both.

Case 1 and 2 are shown in Figure 6.1. The roll angle response obtained from using commanded step signals is normalized relative to the maximum roll angle achieved when exploiting sine commanded signals. This was done to illustrate for which case most roll motion was generated. It is seen that the roll angle and pressure response for both models have the same characteristics. For the commanded step signals it is seen that the corresponding pressure response for both models have step characteristics, which is unrealistic. It is expected that there exist inertia in the pressure propagation inside the cushions due to inflow and outflow inertia and also leakages.

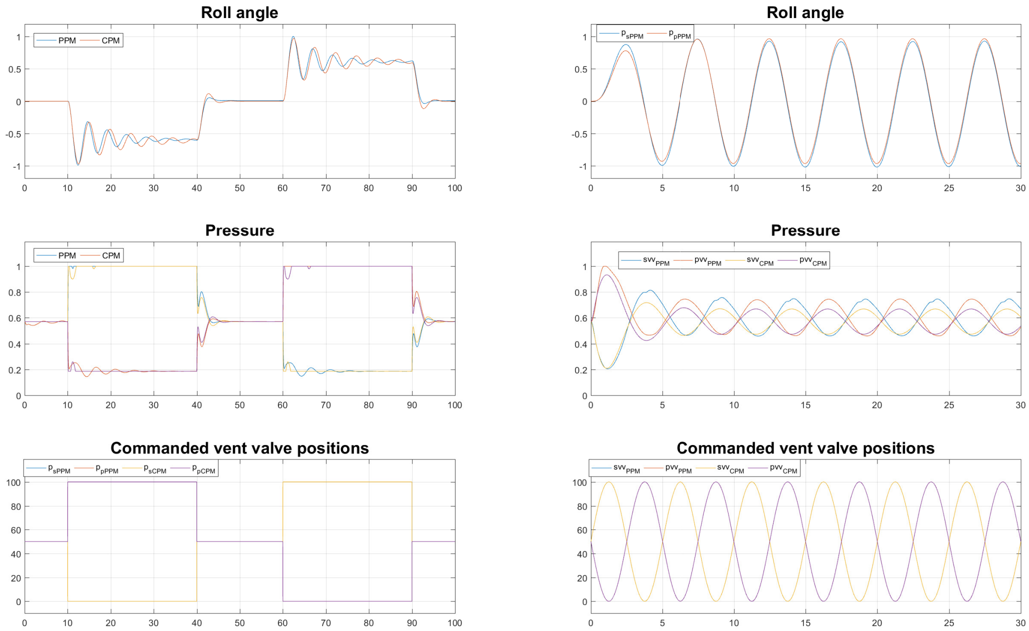

Figure 6.1: Step (left figure) and sine (right figure) commanded vent valve signals (% opening), pressure and roll angle response.

The pressure response for the CPM and PPM experience oscillations when the they are subject to step characteristics, which induce oscillations for the roll rate and roll angle. Since roll rate is coupled to the air cushion pressures, an implicit loop occurs. This is seen from (2.16) and (2.23) for the PPM and (2.6) for the CPM. The pressures are also saturated by an upper and lower bound corresponding to the maximum and minimum achievable pressure, respectively. This was done instead of modeling the leakages. By utilizing saturation, the pressures steady-state values are correct but the inertia for the pressure propagation is not present.

It is seen that greater roll motions are generated for the commanded sine vent valve signals. This is expected since the sine wave frequency is close to the natural resonance frequency for roll and it is also anticipated that greater roll motions will be generated for dynamic control signals than static. It is seen that the roll angle response for the models is close to identical even though the pressure response differs. The pressure potential between the starboard and port air cushion pressure for the PPM, $P_{s_{PPM}}$ and $P_{p_{PPM}}$, respectively, is greater than the potential for the CPM. Since the vent valves are subject to identical commanded signals, the pressure propagation is slower for the CPM. This makes sense since the PPM utilizes a nonlinear pressure model which depends on multiple variables, while the CPM exploits linearized pressures. It is expected that the PPM will experience greater roll motions than the CPM due to its larger pressure potential. This is not the case. This is probably caused by the additional damping which is present in the PPM. Couplings between sway, roll and yaw also exist for the nonlinear model, which leads to more complex behaviour.

6.1.2 Roll damping

Figure 6.2 illustrates the roll angle, pressure response and commanded vent valve signals for beam seas with wave height 2 meters and periods of 5 and 8 seconds. For the 5 second case, shown in the left figure, roll rate is utilized as feedback for the controller, while both roll angle and rate are fed back to the controller for the 8 second case. It is seen that the roll angle is damped significantly for both periods when control is turned on, which occurs at $t = 30$. The proportional and integral term of the PID controller, k_p and k_i, respectively, are kept constant during the entire control on sequence. The roll angle and rate, which are exploited for feedback, are immediately damped when control is turned on. Consequently, the vent valves, and thereby also the pressures, experience spikes in their response for $t = 30$, before their response settle and propagate smoother. It is seen that the commanded vent valve signals vary with greater frequency when damping motion induced by waves with period of 5 seconds than 8 seconds, as expected. The peak-to-peak value between svv and pvv for the PPM and CPM varies slightly. This is due to differences in the feedback signals. The roll angle and roll rate response for the two models differ due to inertia and damping.

Before the controller is turned on, i.e. $t < 30\ s$, both air cushions experience varying pressures, indicating that the wave volume pumping, $\dot{V}_0$, is affecting the pressures. The port pressure for both models, p_p, has greater peak-to-peak value than the starboard pressure, p_s. It is anticipated that this occurs due to the wave direction. The vessel is subject to beam seas attacking port side.

6.1.3 Roll and Heave Damping

Figure 6.3 indicates that it is possible to damp roll and heave motions, simultaneously. The left and right figure illustrates damping in quartering seas with wave height 2 meters and period of 5 and 8 seconds, respectively. It is seen that the roll angle, heave displacement and pressure response for the CPM and PPM are close to identical for both cases, when the vent valves are subject to similar commanded signals. Note that the vent valve signals are almost operating

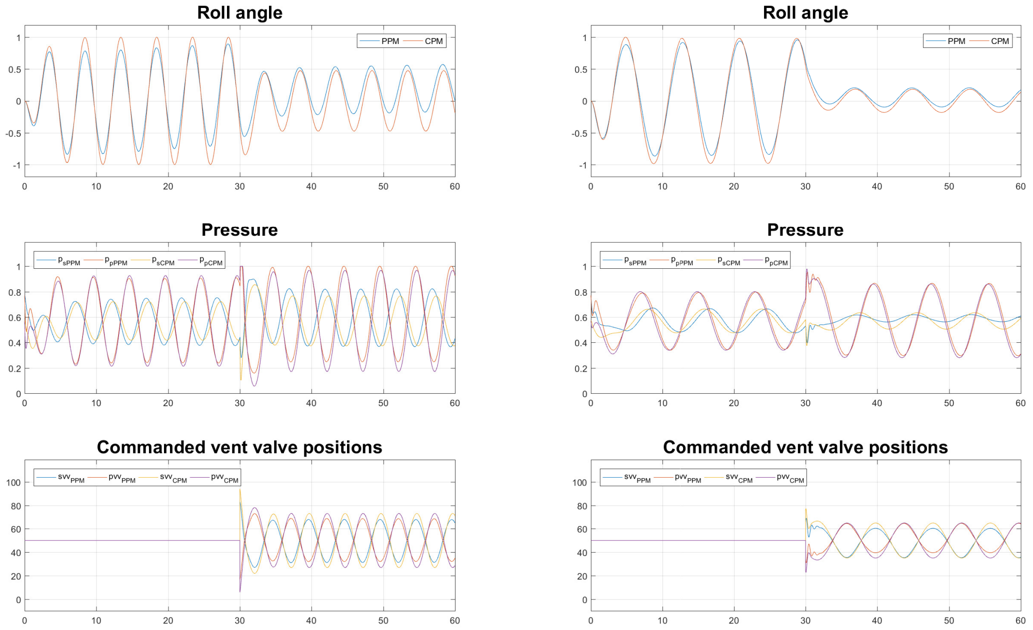

Figure 6.2: Roll damping in beam seas with wave height of 2 meters and period of 5 and 8 seconds, left and right figure, respectively.

in phase, reducing the pressure potential and thereby the roll damping achievable. Therefore, damping of multiple motions is a trade-off between the damping percentages obtainable for the different DOFs.

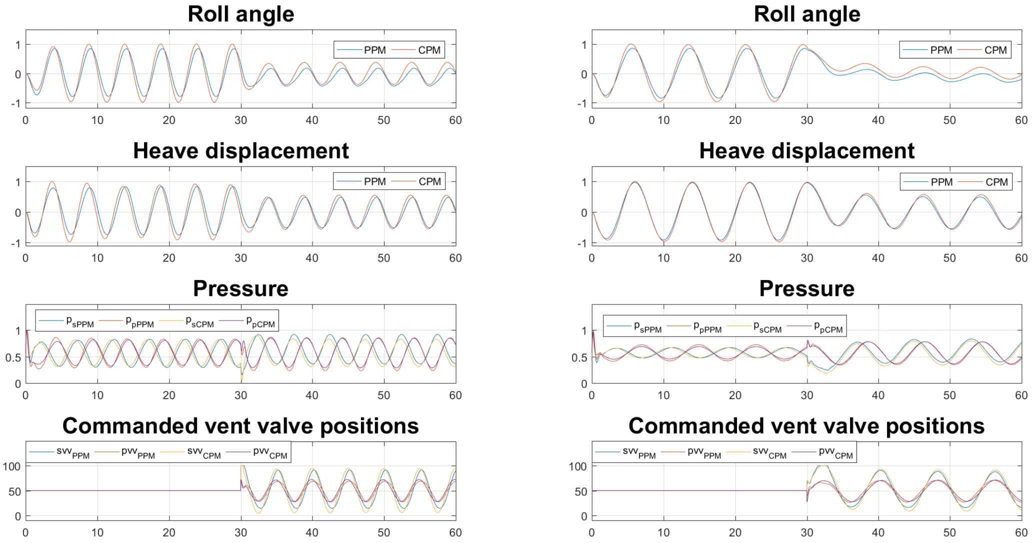

Figure 6.3: Roll and heave damping in quartering seas with wave height of 2 meters and period of 5 and 8 seconds, left and right figure, respectively.

6.2 Model Tests

Multiple tests were accomplished in order to validate the functionality of the longitudinally divided air cushion design. The objective for most of the tests was to damp roll motions as much as possible. Cases where it is desirable to damp both roll and heave motions were also investigated. Finally, the Boarding Control System (BCS) was implemented to check if it is still possible to damp vertical motions at the bow, when the divided cushion design is used. All model tests were performed in Skipsmodelltanken, Sintef Ocean. Note that all model tests presented in this report were executed with water in the aft bag and middle wall. Additional tests were performed without water in the wall, without any noticeable changes in performance. It was considered beneficial to not drain the wall, since the water may add passive roll damping.

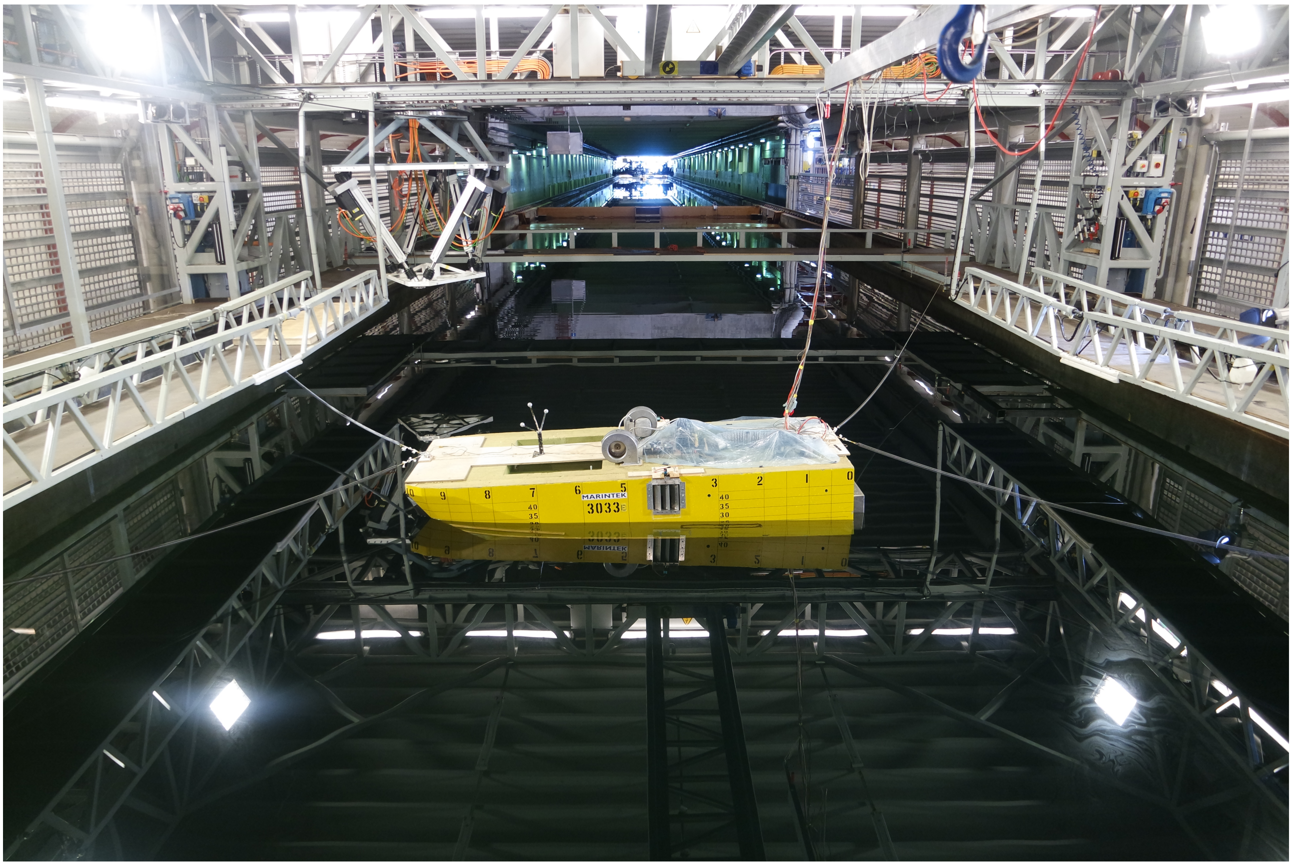

Figure 6.4: Model 3033E in the ship model tank, ready for testing.

6.2.1 Natural Periods

Before the regular and irregular waves were calibrated, natural periods in heave, roll and pitch were determined. The reason for identifying these periods was to apply waves with frequency both above, on and below the natural frequencies of the vessel. The natural periods were found by using a stick to push the vessel to a certain position and orientation for heave, roll and pitch, and then release it. By doing this, the vessel will oscillate around some mean value with its natural period. Since the air cushion pressures highly affect these periods, the tests were performed both on- and off-cushion.

The stick was placed above the port vent valve to induce roll motions and in the bow for pitch and heave. Optimally, the stick would have been pushed down above the center of gravity to induce heave motions. Due to the pressure forces, which strive to maintain the equilibrium position, this was impossible. Figure 6.5, 6.6 and 6.7 illustrate the response in roll, heave and pitch, respectively. The first peak in the figures occurred when the vessel was pushed down and released. The natural periods are determined off-cushion and on-cushion for the vent valve openings 100 %, 50 % and 0 %. 100 % opening represents the minimum pressure which may be in the air cushions during control, while maximum pressure occurs at 0 % vent valve opening.

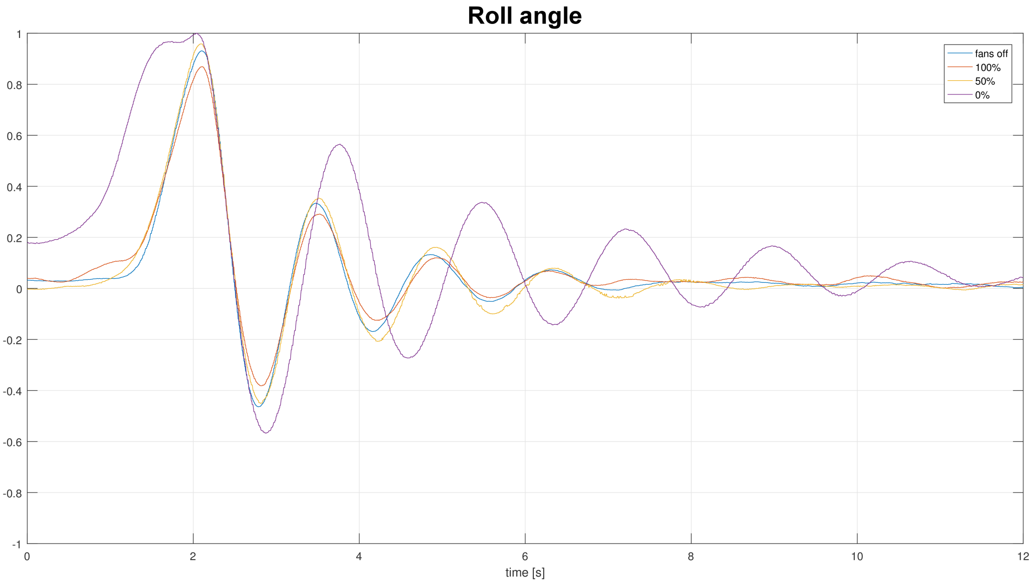

Figure 6.5: Natural roll periods on- and off-cushion.

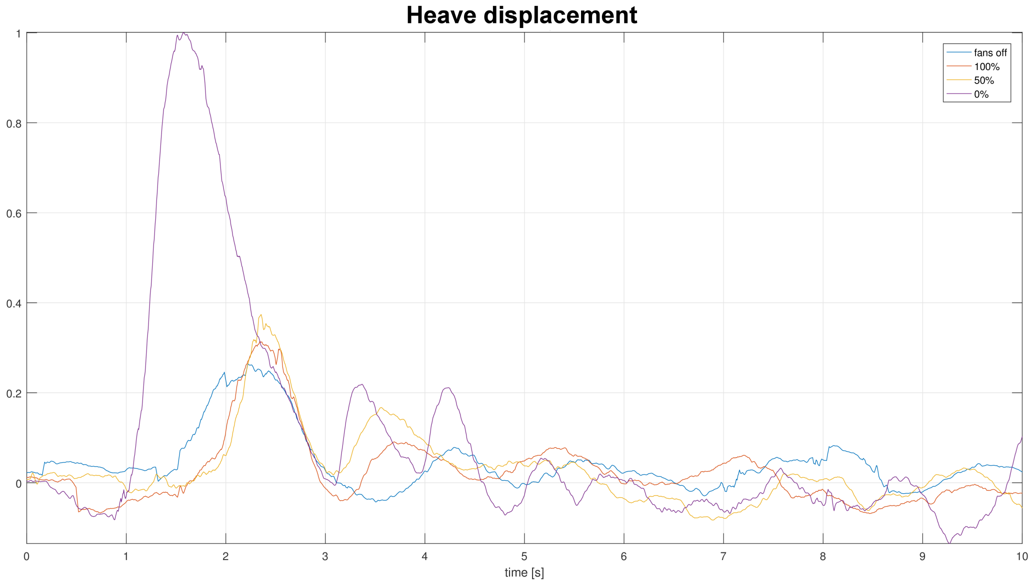

Figure 6.6: Natural heave periods on- and off-cushion.

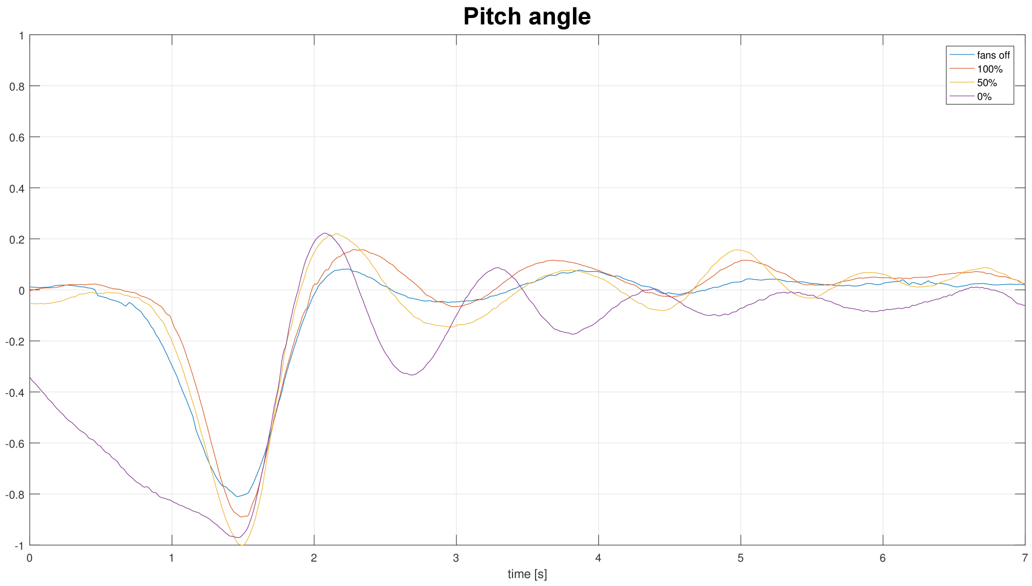

Figure 6.7: Natural pitch periods on- and off-cushion.

Note that the amount of water in the aft bag and separating wall will affect the natural periods for heave, roll and pitch. The volume of water will decrease as the pressures increase, meaning that the water inside the aft bag and separating wall will influence the periods more for off-cushion and 100% vent valve openings, than for full closed vent valves.

From Table 6.1 it is seen that the natural period for roll increases as the pressure increases, while the natural periods for heave and pitch decrease as the pressure increases. According to Fossen (2011) the natural frequencies for heave, roll and pitch can be written

$$\omega_i = \sqrt{\frac{C_i}{M_i + A_i(\omega_i)}}, \quad \text{for} \;\; i = \{\text{heave}, \text{roll}, \text{pitch}\} \tag{6.1}$$

When comparing Table 6.1 to (6.1), it makes sense that the natural frequencies varies dependent on pressure. For heave and pitch rising pressure will increase the spring stiffness, C_i, and thereby increase the natural frequencies and reduce the natural periods. Increasing air cushion pressure reduces the submerged hull volume. Therefore, it is expected that the spring stiffness in roll, C_{roll}, will be less for fully closed vent valves than fully open. This leads to increased natural roll periods for rising pressure.

Table 6.1: Test N000B and N001A. Natural periods determination.

DOF	Off-cushion (model scale / full scale) [s]	On-cushion (model scale / full scale) [s]		
		100%	50%	0%
Heave	1.86 / 5.26	1.61 / 4.55	1.41 / 3.99	0.91 / 2.57
Roll	1.39 / 3.93	1.42 / 4.02	1.42 / 4.02	1.78 / 5.04
Pitch	1.54 / 4.36	1.51 / 4.27	1.20 / 3.39	1.10 / 3.11

When the waves were calibrated, only the natural periods in roll were taken into account. This was because the main objective for this thesis is to investigate roll damping. According to 6.1, the natural periods for roll, on-cushion, varies between approximately 4 and 5 seconds, full scale. A wave period of 4 seconds full scale corresponds to 1.41 seconds model scale, which is a wave frequency of 0.71 Hz. Figure 5.13 shows the frequency response of the port servo system utilized for changing the port vent valve opening. The figure implies that the servo system has a phase lag of 20° for 0.7 Hz, meaning that the servo system may not be able to control fully open → fully closed → fully open fast enough for this period. Hence, the servo system may be to slow to compensate for waves with period 1.41 seconds. Consequently, no waves with period below 4 seconds were calibrated. Table 6.2 shows the calibrated full scale regular and irregular waves. Due to the uncertainty concerning the servo system, the irregular waves were calibrated for 5 instead of 4 seconds period. All sea waves were calibrated according to NTNU and Sintef Ocean standards.

Table 6.2: Experimental tested sea waves.
R - regular wave. I - irregular wave.

Wave Height [m]	Wave Period [s]			
	4	5	6	8
1	R	R, I	R	R
2	R	R, I	R	R

6.2.2 Roll Generation

Both static and dynamic calm water tests were performed to check if the control system is actually able to damp roll motions. This was done by doing the opposite; generating roll motions. By controlling the starboard and port air cushion pressures separately, it was expected that the pressures could induce roll motions. Three tests were executed. The vent valve signals were commanded steps for the first case, and commanded sine waves and pulse trains for the second and third.

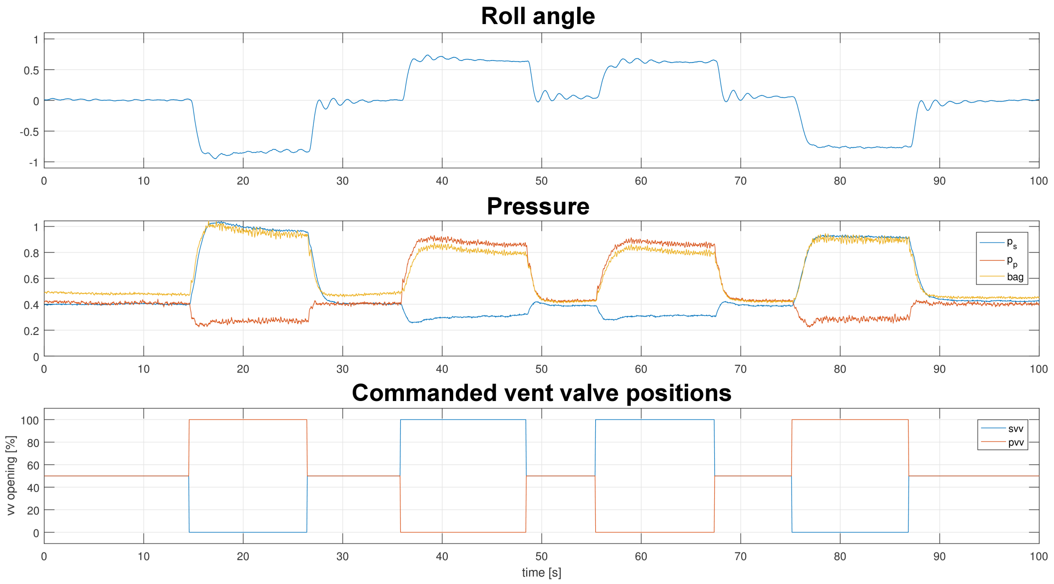

Figure 6.8: Roll angle and pressure response for step commanded vent valve positions.

Figure 6.8 illustrates the static roll generation test. Steps were used to change the commanded vent valve positions. For the first pulse, the starboard vent valve, svv, is commanded from bias opening to fully closed opening, i.e. 50 % → 0 %. The starboard pressure, P_s, is increasing, and vice versa for the port vent valve and pressure. This leads to a negative roll angle, as expected. From the plots for commanded vent valve positions and air cushion pressures it is seen that there is a time delay between the commanded signals and the pressure response. This is due to the inertia in the servo system and pressure propagation. The servos are not able to follow commanded step signals and the pressures require time to spread. The pressure plot also illustrates that the bag pressure is greater than the starboard and port air cushion pressure for bias vent valve opening. However, for fully closed starboard vent valve and fully open port vent valve, and vice versa, the bag pressure is less than the greatest pressure. By design, the bag pressure should always be greater than both pressures to ensure a stiff middle wall and no leakage between the two chambers. This is not the case, meaning leakages may occur when the starboard and port pressure are different.
Significant pressure potential differences for the pulses 1 and 4 compared to 2 and 3 are present. The potential for svv fully closed and pvv fully open is larger than the potential for vice versa openings. Consequently, the magnitude of the negative roll angle is greater than the positive roll angle induced. This may occur due to multiple reasons.

- The T-duct utilized to provide the bag fan with the highest air cushion pressure may not work as intended. A volumetric air flow from the chamber with the highest pressure to the chamber with the lowest pressure may occur over this construction. This will lead to a ”lower” upper pressure and a ”higher” lower pressure. Hence, a reduced pressure potential.

- A greater difference between port and bag pressure occurs for *pvv* fully closed and *svv* fully open, than starboard and bag pressure for vice versa vent valve openings. This implies that the separating wall will be less stiff and have more freedom to move. Since the wall is designed to operate close to the water line for maximum pressure, its stiffness is crucial. Less stiffness may lead to that the wall is laying on the water line, and a leakage from port to starboard chamber appears, reducing the pressure potential.

- The leakages along the finger skirt and aft bag may be asymmetrical and thereby unequal for the two cushions. Both skirts are designed in such a way that leakages occur in the corner skirt/side hull/water line for maximum pressure. Individual differences between pressures and leakages along the finger skirt were observed during this model test. Leakages was not observed at the starboard finger skirt corner for fully closed *svv* and fully open *pvv*. For vice versa vent valve openings, a significant leakage at the port finger skirt corner appeared. Hence, minor asymmetric seal effect may have resulted in less pressure potential.

- The separating wall is fixed to the aft bag. The wall may experience greater transversely displacements against starboard for $p_p > p_s$, than displacements against port for $p_p < p_s$. If this occurs, the leakages between the side hulls and aft bag will be different, inducing different pressure potential and explaining why the bag pressure is significantly less than the port pressure for $p_p > p_s$.

- The bag fan may not be strong enough to provide both the aft bag and middle wall with greater pressure than both chambers. The bag pressure should always have the highest numerical value, which obviously is not the case. This leads to less wall stiffness, which may induce leakage between the chambers.

Probably, the difference in pressure potential is a combination of these assumptions. The starboard pressure in pulse one has greater ascent than the port pressure in pulse two. This may be due to that the port finger skirt leakage grows as the pressure increases. If the aft bag leakages are asymmetrical, this may lead to a reduced pressure potential and greater difference between port and bag pressure. This causes a less stiff middle wall, which may induce leakage from port to starboard chamber. The pressure response from this test resulted in finger skirt, aft bag and middle wall modifications, without any improvements in performance for this test. However, the pressure differences experienced here was not a problem in the remaining tests, since the commanded vent valve signals varied to fast for the pressure to build up to its maximum value.

Figure 6.9 illustrates the dynamic roll generation tests. The roll angle and pressure response when sine waves and pulse trains are utilized for the commanded vent valve signals are shown. Both the roll angle response for commanded steps in Figure 6.8 and sine wave signals in Figure

6.9 are illustrated relative to the roll angle response for commanded pulse train signals. 1 and -1 refers to the maximum and minimum roll angle, respectively, during the pulse train time series. From Figure 6.8 and 6.9 it is seen that pulse trains generate most roll motions, thereafter sine waves and steps. The pressure response for both cases are as expected, for commanded pulse train signals the pressures have zigzag characteristics, since they should increase and decrease as fast as possible. The pressure characteristics for the commanded sine wave signals are smoother and follows the commanded signal in a better way.

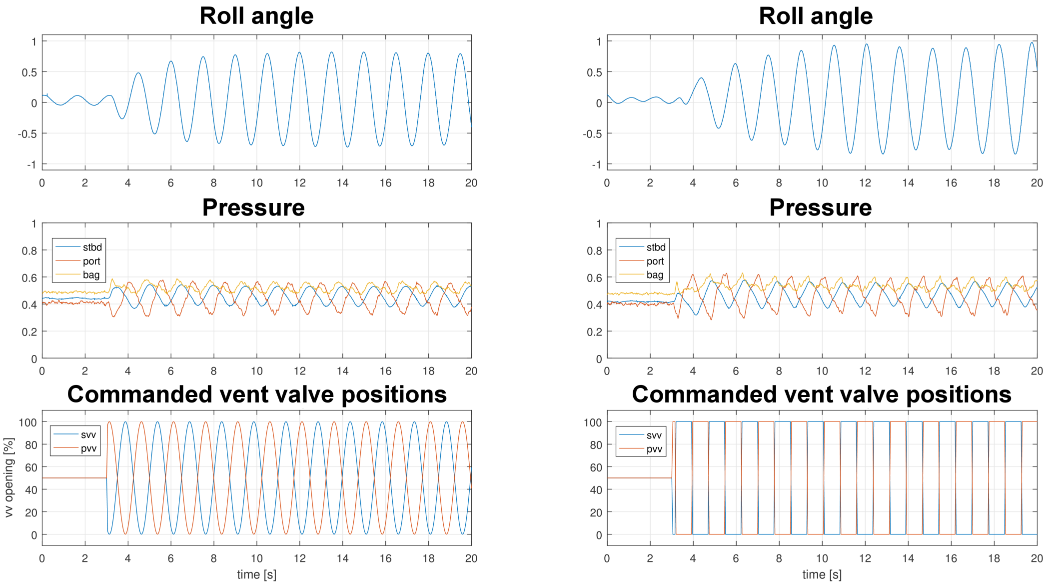

Figure 6.9: Roll angle and pressure response for sine wave (left figure) and pulse train (right figure) commanded vent valve positions.

In Figure 6.10 the roll angle response is shown versus the commanded vent valve signals frequencies. The first sequence in both plots represents the commanded sine wave signals while the second is the commanded pulse train signals. It is seen that most roll motions are generated for $0.65 - 0.7$ Hz model scale, which is are period of $4.05 - 4.35$ seconds full scale. This is inside the natural period area for roll on-cushion, and is expected to be the resonance area for roll.

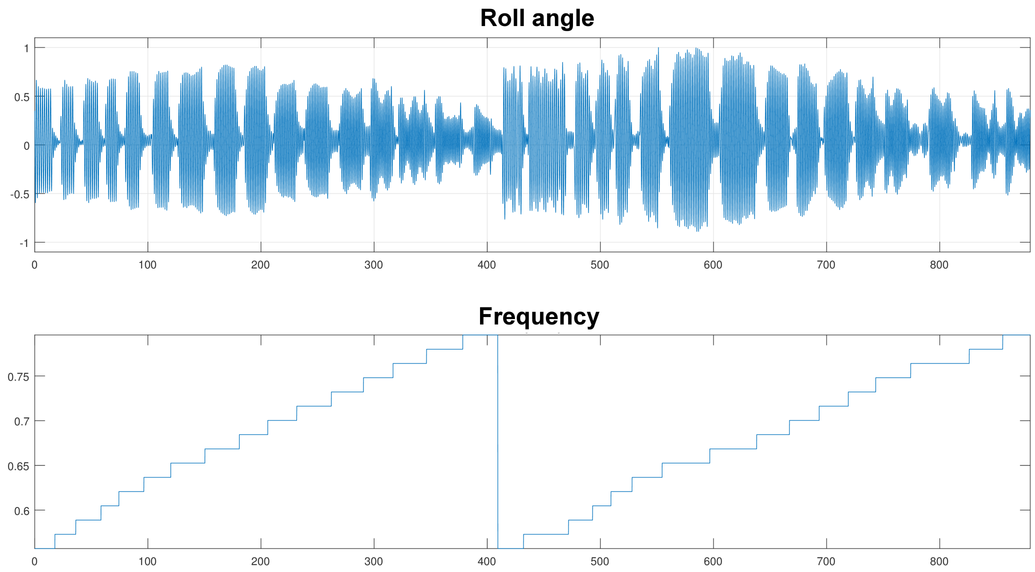

Figure 6.10: Roll angle response versus commanded vent valve signals with increasing frequency

6.2.3 Heave and Pitch Generation

A heave and pitch generation test was performed in order to validate that the control system can induce these motions by controlling the vent valves in phase. Figure 6.11 illustrates that this is possible. It is seen that the commanded vent valve signals, svv and pvv, are in phase, and thereby also starboard and port air cushion, p_s and p_p, respectively. These pressures induce both a heave displacement and a pitch angle. Therefore, it is expected that heave and pitch damping is still possible when utilizing the split cushion design.

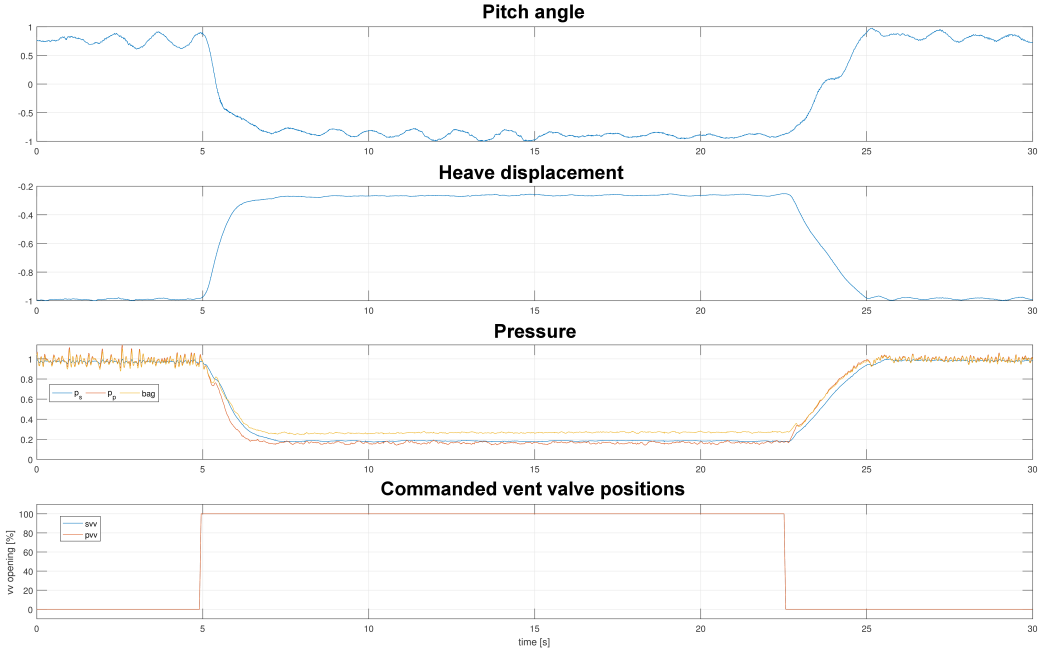

Figure 6.11: Heave displacement, pitch angle and pressure response for commanded step vv signals in phase

6.2.4 Roll Damping

Bow, beam and quartering regular and irregular seas, with wave height 1 and 2 meters and various frequencies were applied to the model vessel to verify the overall performance of the roll damping control system. In order to achieve the greatest damping percentage possible, different combinations of the PID controller were evaluated for each case.

Figure 6.12 and 6.13 illustrate the commanded vv signals, pressure and roll angle response for beam seas, wave height of 1 meter and wave periods of 8, 6, 5 and 4 seconds. The parameters utilized in each model test are shown in Table 6.3 - 6.6. From the tables and figures it is seen that the control system is able to damp roll motions significantly for these environmental conditions. The roll angle is damped approximately $55 - 65$ % for waves with period $5 - 8$ seconds. It was expected that most roll damping would have been achieved around the resonance period for roll, since the greatest roll motions appear here. Table 6.6 and Figure 6.13 indicate that this may not be true. The maximum damping percentage obtained for test N010D is 24.2 %, which is remarkably less than for the other cases. Note that the roll angle response characteristics for wave period of 8 seconds, shown in Figure 6.12, differs from the response obtained for shorter periods. The reason for this is that the model scale vessel rolls with both its natural roll period and the wave period.

From Table 6.3 and 6.4 it is seen that $k_i > 0$ for the low-frequent waves. The integral term is used to remove steady-state offsets which occur for the waves with greater period. Table

6.5 and 6.6 shows that $k_d > 0$ for the high-frequent waves. The proportional term, k_p, is the dominating part of the controller where phase lag of the servo system is not an issue.

Table 6.3: Test N013C.
Roll damping. Regular seas.

Parameter	Value
Date	18.05.2017
Result	56.4 % roll damping
Wave direction	90°
Wave height	1 m
Wave period	8 sec
k_p	10
k_i	2
k_d	0
Control on	15 s
Bias vent valves	50 %

Table 6.4: Test N012B.
Roll damping. Regular seas.

Parameter	Value
Date	16.05.2017
Result	63.4 % roll damping
Wave direction	90°
Wave height	1 m
Wave period	6 sec
k_p	10
k_i	5
k_d	0
Control on	15 s
Bias vent valves	50 %

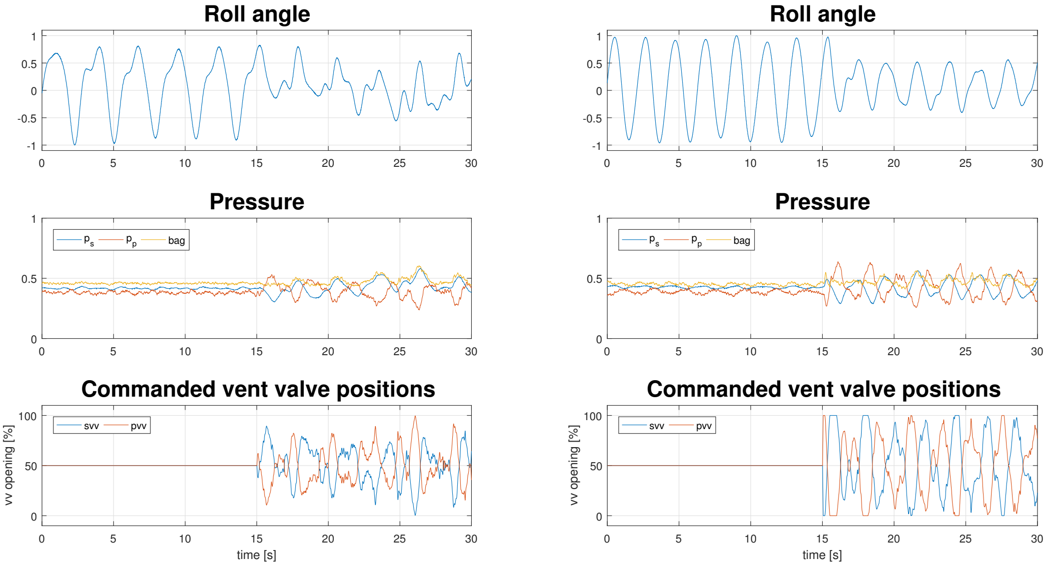

Figure 6.12: Response for regular beam seas with height and period of 1 meter and 8 (left figure) and 6 (right figure) seconds, respectively.

Table 6.5: Test N011F.
Roll damping. Regular seas.

Parameter	Value
Date	18.05.2017
Result	59.2 % roll damping
Wave direction	90°
Wave height	1 m
Wave period	5 sec
k_p	2
k_i	0
k_d	3
Control on	15 s
Bias vent valves	50 %

Table 6.6: Test N010D.
Roll damping. Regular seas.

Parameter	Value
Date	18.05.2017
Result	24.2 % roll damping
Wave direction	90°
Wave height	1 m
Wave period	4 sec
k_p	0
k_i	0
k_d	5
Control on	10 s
Bias vent valves	50 %

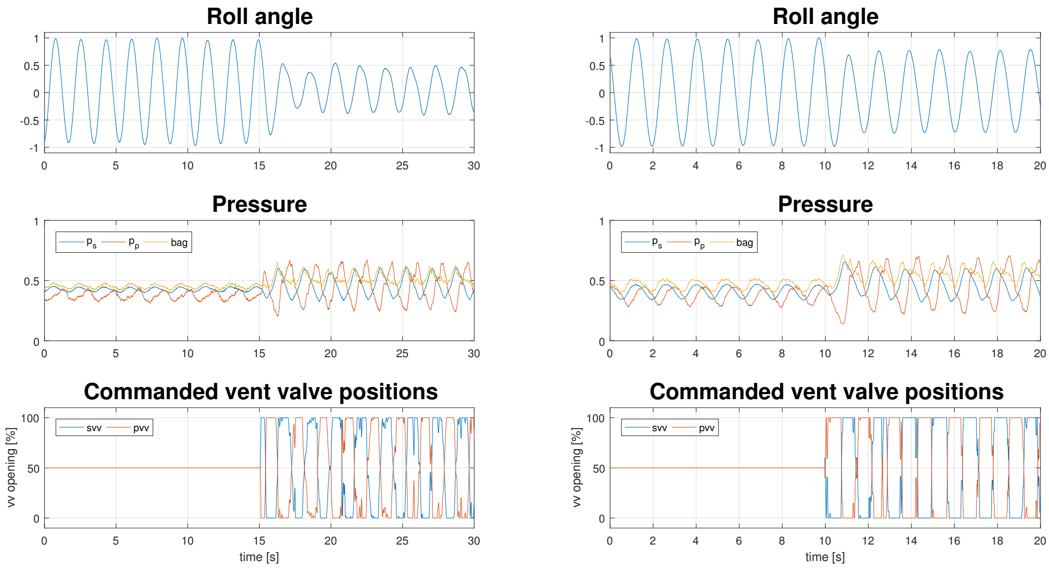

Figure 6.13: Response for regular beam seas with height and period of 1 meter and 5 (left figure) and 4 (right figure) seconds, respectively.

As discussed in Section 6.2.1 phase lag occurs on the servo system when compensating for waves with 4 seconds period. During the tests for this period, it was observed that the vent valves were not able to operate in the desired phase. This may be due to multiple reasons. Initially, roll rate was exclusively utilized for feedback, meaning $k_p > 0$. Since roll rate has its greatest magnitude for $\phi = 0$ the vent valves should have been fully open and fully closed for the wave crest and trough, respectively. By eye measure, the servo system was estimated to have a phase lag of approximately 45°. Due to the inertia of the servo system, it was considered disadvantageous to exploit roll rate for feedback. Instead, the derivative of the roll rate was used. The response pressure and vent valve response when the roll rate and roll angular acceleration is fed back to the controller is shown in the left and right time series in Figure 6.14, respectively.

The feedback signals that was exploited for test N010C and N010D are shown in Figure 6.14, left and right time series, respectively. The roll angle was obtained from Oqus, while the low-pass filtered rate, lp rate, was provided by the gyro and the roll angular acceleration is the derivative of the lp rate. It is seen that the angular acceleration is 180° and 90° phase shifted relative to the roll angle and lp roll rate, respectively, as expected. The left figure shows the vent valve and pressure response when low-pass filtered roll rate is exploited for feedback. It is seen that the vent valve signals operate in phase with the feedback signal, which is actually phase shifted approximately 15° relative to the raw roll rate. When comparing the commanded vv signals and the starboard and port air cushion pressure, it is seen that a phase shift of approximately 85° is present. This is due to the inertia of the servos and pressure propagation. The raw roll rate reaches its maximum value for $t = 2\ s$. In order to damp roll motions by feeding lp rate back to the controller, it is desired that p_s is high and p_p is low for $t = 2\ s$. This is not the case. From the pressure time serie it is seen that this occurs for approximately $t = 2.5\ s$, meaning that the pressures are phase shifted approximately 100° relative to the raw rate. The measured pressures are close to operate in phase with the roll angle.

In the right times series of Figure 6.14, roll angular acceleration is exclusively exploited for control, i.e. $k_d > 0$. It is seen that the vent valves operate in phase with the angular acceleration. Maximum starboard pressure occurs somewhere in between maximum roll rate and angle. Based on the figure, the pressures are assumed to be approximately 125° phase shifted relative to the feedback signal.

Due to the total phase lag of the system from low-pass filtered roll rate to pressure propagation, the derivative term of the PID-controller made the vent valves operate closer to the desired phase. Hence, by utilizing angular acceleration for feedback and exploiting the phase lag of the servo system, some roll damping was achieved. However, it is expected that far better performance would have been obtained by using faster servos that are able to operate in the correct phase and also reduce the noise suppression of the low-pass filer to remove feedback signal phase lag.

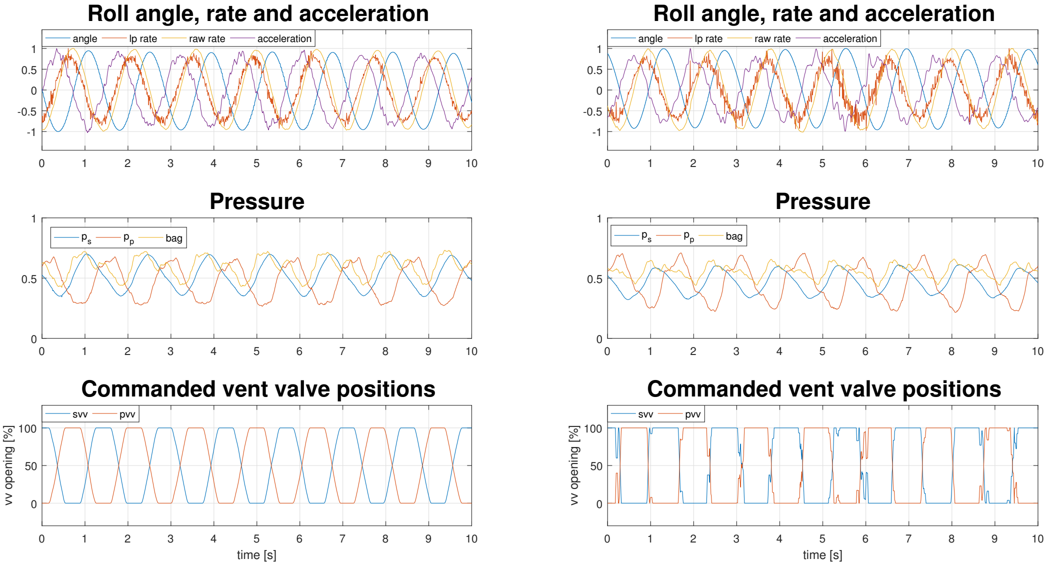

Figure 6.14: Feedback signals versus pressures and commanded vent valve signals for beam seas with wave height and period of 1 meter and 4 seconds, respectively.

Before control is turned on for each test, it is seen from the figures that the vent valves operate at bias opening, $svv = pvv = 50$ %. The pressures varies before roll is actively damped, meaning other variables than the vent valve openings affect the pressures. This is expected. Equation (2.6) implies that the pressures are dependent on heave, roll and pitch motion and also wave volume pumping. When the vessel is exposed to beam seas, pitch motions are assumed neglectable. Since the model is rolling symmetrical ±1 and heave motion is uniformly distributed over the entire vessel, it is expected that the pressure difference between starboard and port pressure is caused by wave volume pumping. From Figure 6.12 and 6.13 it is seen that before control is turned on, the peak-to-peak value of the pressure oscillations are larger for shorter wave periods. Equation (2.20) demonstrates that wave volume pumping is dependent on wave frequency, which strengthen the assumption that the pressure oscillations are caused by this parameter.

Figure 6.15 shows the response obtained when the vessel is subject to beam seas with wave height 2 meter. Time series for 5 and 8 seconds are included, where Table 6.7 presents the 5 second test parameters, while Table 6.8 belongs to the 8 second test. It is seen that the control system is able to damp approximately the same amount of roll motions for 1 and 2 meter wave height when the vessel is subject to waves with 8 seconds period. This is not the case for more high-frequent waves. This makes sense, since the roll excitation moment induced by the waves increases along with wave height. The pressure-induced roll moment, which is exploited to compensate for the wave-induced moment, has some maximum and minimum value. This implies that by increasing the roll excitation moment, less damping is expected.

Table 6.7: Test N015C.
Roll damping. Regular seas.

Parameter	Value
Date	18.05.2017
Result	19.7 % roll damping
Wave direction	90°
Wave height	2 m
Wave period	5 sec
k_p	1
k_i	0
k_d	0.5
Control on	15 s
Bias vent valves	50 %

Table 6.8: Test N017C.
Roll damping. Regular seas.

Parameter	Value
Date	18.05.2017
Result	56.0 % roll damping
Wave direction	90°
Wave height	2 m
Wave period	8 sec
k_p	3
k_i	1
k_d	3
Control on	20 s
Bias vent valves	50 %

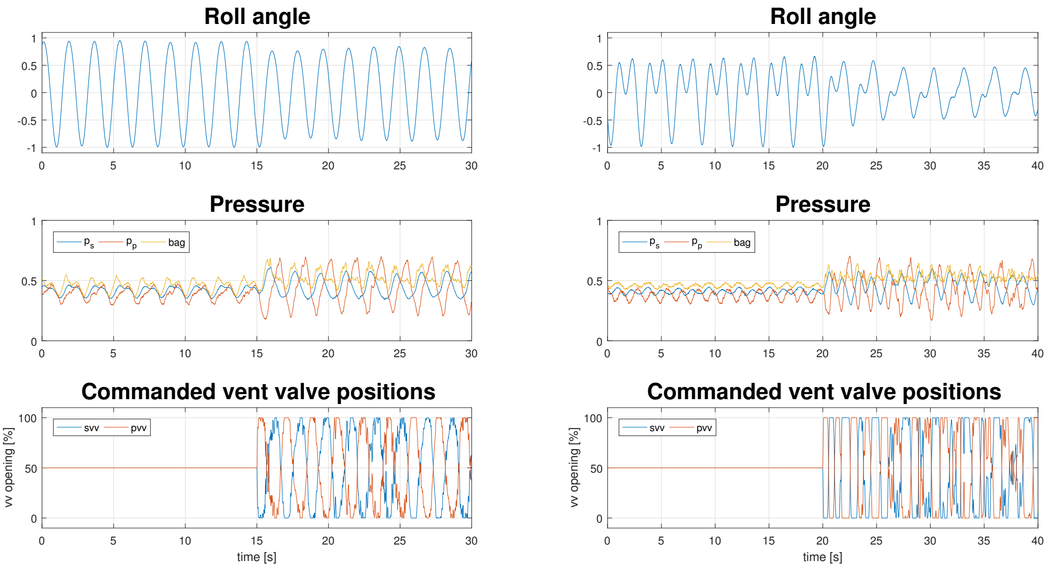

Figure 6.15: Response for regular beam seas with height and period of 2 meter and 5 (left figure) and 8 (right figure) seconds, respectively.

Irregular waves were applied to the vessel to validate the functionality of the roll damping control system in realistic environmental conditions. Figure 6.16 shows the time series of roll angle, pressures and commanded vv signals for a 20 minute run. As Table 6.9 indicates, control is turned on after 10 minutes, where the controller gains, k_p and k_d, are kept constant during the entire control on sequence. The vessel was exposed to beam seas with significant wave height $H_s = 1\ m$, and peak period $T_p = 5\ s$. The MATLAB function `rms` was utilized to compute the root-mean-square value for control off ($t < 10\ min$) and control on ($t > 10\ min$). The damping percentage was found to be 28.6 %.

Table 6.9: Test N054B. Roll motion damping. Irregular seas.

Parameter	Value
Date	18.05.2017
Result	28.6 % roll damping
Wave direction	90°
Wave height	1 m
Wave period	5 sec
k_p	2
k_i	0
k_d	3
Control on	10 min
Bias vent valves	50 %

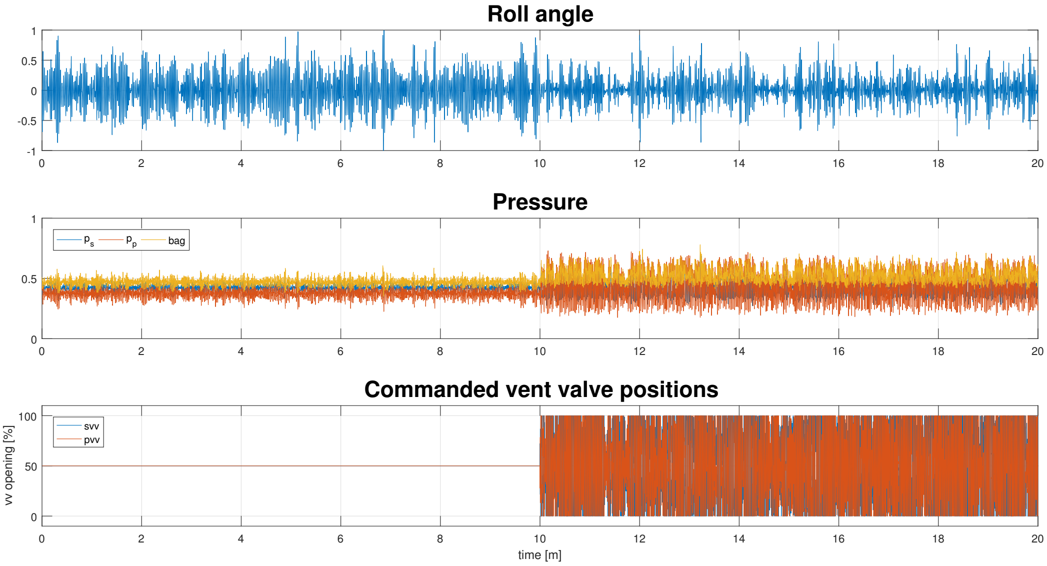

Figure 6.16: Response for irregular seas. $\psi_w = 90°$, $H_s = 1\ m$ and $T_p = 5\ s$

Figure 6.17 shows a segment of the response obtained from applying irregular beam seas with significant wave height $H_s = 2\ m$, and peak period $T_p = 5\ s$ to the vessel. Table 6.10 illustrates that the roll damping percentage was found to be 9.0 %.

Table 6.10: Test N055B. Roll damping. Irregular seas.

Parameter	Value
Date	18.05.2017
Result	9.0 % roll damping
Wave direction	90°
Wave height	2 m
Wave period	5 sec
k_p	1
k_i	0
k_d	0.5
Control on	10 min
Bias vent valves	50 %

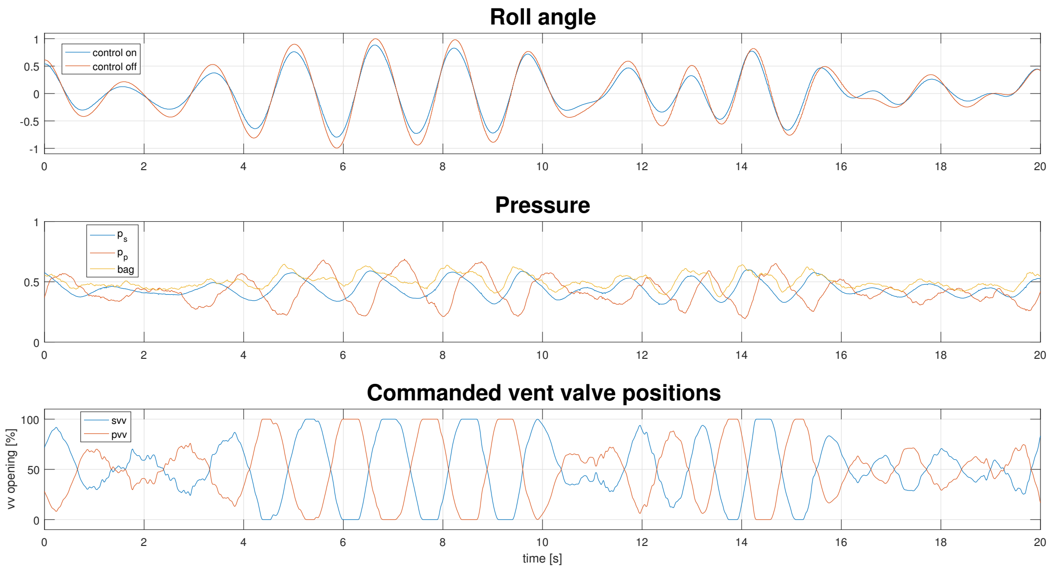
Roll angle

Pressure

Commanded vent valve positions

Figure 6.17: Response for irregular seas. $\psi_w = 90°$, $H_s = 2\ m$ and $T_p = 5\ s$

The irregular model tests were executed by using two different approaches, where the roll damping percentage obtained is more accurate for method 2 than method 1. The first method was performed as follows

- The wave maker was creating waves for 22 minutes, where the last 20 minutes were logged.
- During the first 10 minutes of logging, control was off.
- Control was activated for last 10 minutes of logging.

Test N054B was done by using method 1, while test N055B exploited method 2, which was accomplished in the following way

- The wave maker was on for 10 minutes. Control was active for the entire sequence, where the last 8 minutes were logged.
- The wave maker was restarted. Then, the same procedure was executed for control off.

From Figure 6.18 it is seen that the vessel is exposed to a more equal wave spectra for control on and off when method 2 is used. Optimally, this method should have been utilized for all irregular wave tests to achieve more accurate damping percentages. For method 1, the dominating peak for control on occurs for 0.568 Hz, which corresponds to a wave period of 4.98 seconds full scale. A dominating peak also occurs for this wave period for control off. The spectra differ for 0.610 Hz which is a wave period of 4.634 seconds full scale. The control off spectrum has a dominating peak for this frequency, while the control on spectrum does not. Since the control system damps less roll motion for shorter wave periods, the damping percentages obtained from the irregular tests where method 1 is used are assumed to be some percentage points too high. However, the peak for 4.634 seconds is above the assumed roll resonance period. Therefore, the wave spectra for method 1 is still considered to lead to fairly realistic damping performance.

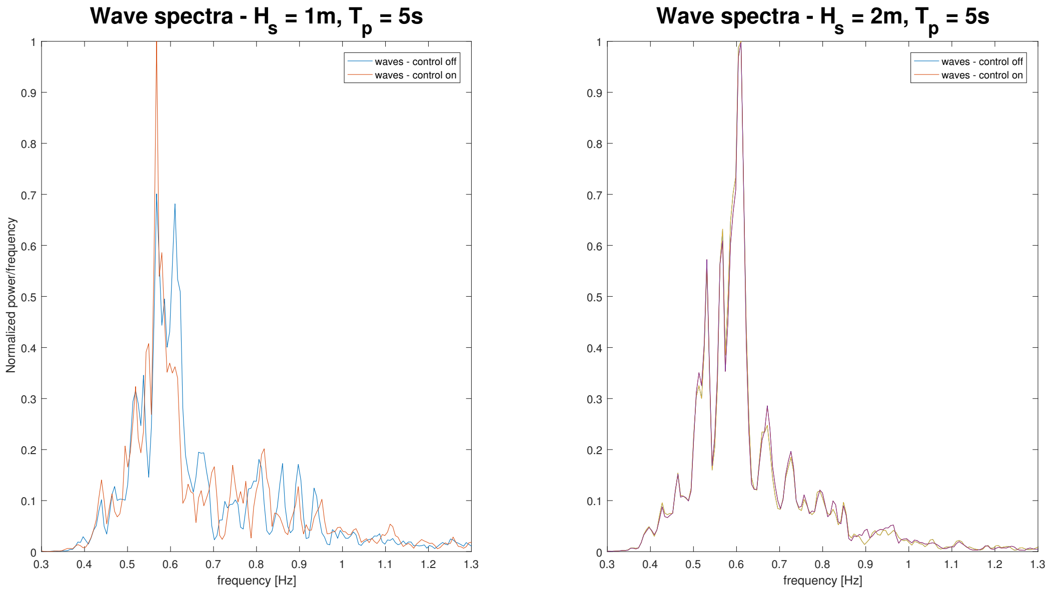

Figure 6.18: Wave spectra for irregular waves with significant wave height 1 and 2 meter, left and right figure, respectively, and wave peak period of 5 seconds.

The overall roll damping performance of the control system is illustrated in Table 6.11 and 6.12 and in Figure 6.19. The curves illustrate the roll damping percentages obtained for regular and irregular waves with various wave directions, heights and periods. The MATLAB function `spline` was exploited to interpolate between the damping percentages presented in the tables. The figure indicates that it is easier to damp roll motions for $H_w = 1\ m$ than $H_w = 2\ m$. Even though more roll damping occurs for smaller wave heights, the control system is able to damp $H_w = 2\ m$ significant. The tendency is that more roll damping appears for bow and quartering seas than for beam seas and also for longer wave periods. This makes sense since the wave excitation forces, which the pressure forces are utilized to compensate for, are dependent on wave direction, height and period. The roll excitation moment grows as the wave height increases and the wave period decreases. Its greatest numerical value appears for beam seas. Since the pressure-induced roll moment is limited due to the maximum and minimum pressure achievable in starboard and port air cushion, the roll damping percentage is expected to decrease as the roll wave excitation moment increases. Consequently, since greater roll angular deflections appear for beam seas than for bow and quartering seas, less roll damping is expected to be present for these cases.

Table 6.11: Roll damping percentages for regular seas.

Wave direction	$H_w = 1\ m$				$H_w = 2\ m$			
	4s	5s	6s	8s	4s	5s	6s	8s
45°	92.0 %	87.0 %	71.5 %	71.9 %		39.7 %	57.2 %	75.0 %
90°	24.2 %	59.2 %	63.4 %	59.0 %		19.7 %	37.7 %	47.0 %
135°	81.9 %	70.3 %	70.6 %	67.8 %	73.0 %	54.4 %	56.9 %	68.5 %

Table 6.12: Roll damping percentages for irregular seas with $T_p = 5\ s$

Wave direction	$H_s = 1\ m$	$H_s = 2\ m$
45°	54.9 %	43.1 %
90°	28.6 %	9.0 %
135°	66.2 %	41.4 %

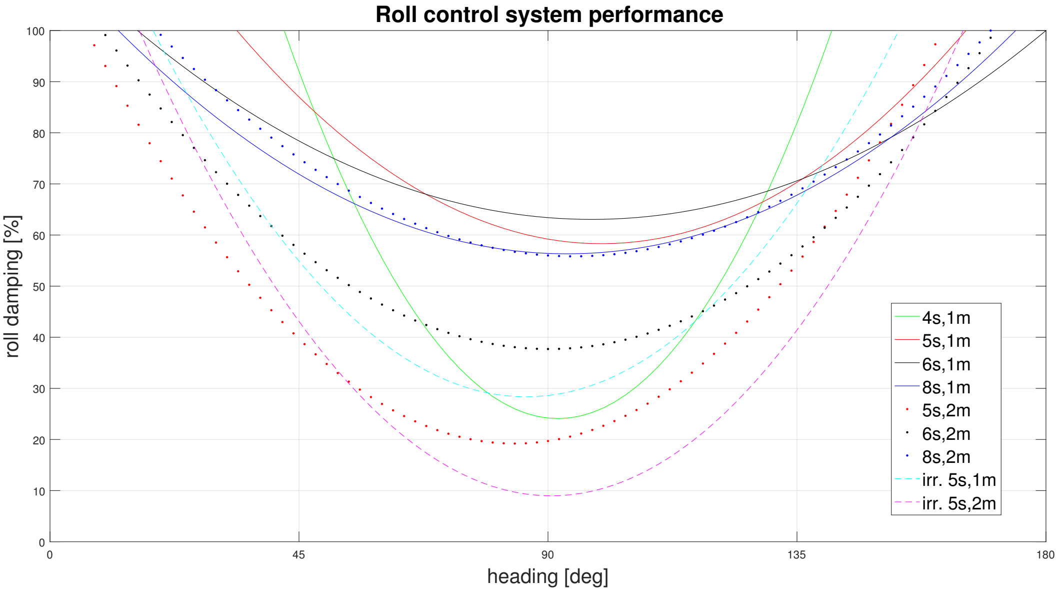

Figure 6.19: Roll damping percentage for various wave directions, heights and periods

6.2.5 Roll and Heave Damping

For bow and quartering seas heave, roll and pitch motions occur. Therefore, it was investigated if it is possible to damp both heave and roll motions exploiting the implemented split cushion design. The vessel was exposed to bow and quartering seas with period 4 seconds, which is close to the resonance period for roll when on-cushion.

Figure 6.20 shows the roll angle, heave displacement, pressure and commanded vv signals response for bow and quartering seas, with wave height 1 meter. For both cases roll damping was prioritized. From Table 6.13 and 6.14 it is seen that both roll and heave damping are present for both tests. Roll and heave rate were fed back to the controller, meaning that only the proportional term of the PID-controller was used. Due to the servo system inertia experienced for beam seas with wave period of 4 seconds, even better damping percentages may have been achieved if derivative terms had been used for roll angular acceleration and heave linear acceleration in the controller.

Table 6.13: Test N035A.
Roll and heave damping. Regular seas.

Parameter	Value
Date	15.05.2017
Result	54.3 % roll damping
	41.2 % heave damping
Wave direction	45°
Wave height	1 m
Wave period	4 sec
Control on	20 s
Bias vent valves	50 %

Table 6.14: Test N037A.
Roll and heave damping. Regular seas.

Parameter	Value
Date	15.05.2017
Result	38.5 % roll damping
	21.5 % heave damping
Wave direction	135°
Wave height	1 m
Wave period	4 sec
Control on	20 s
Bias vent valves	50 %

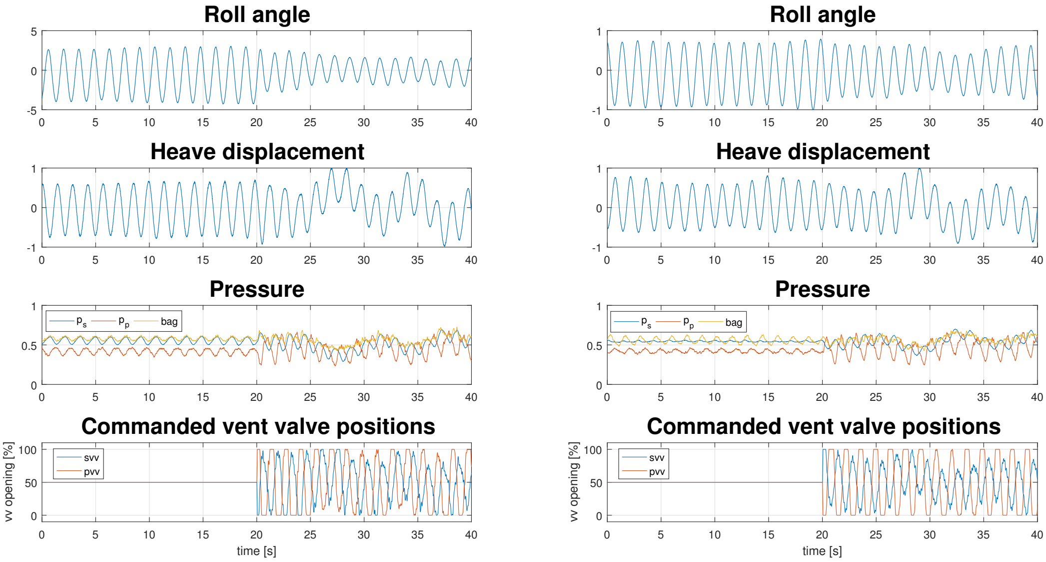

Figure 6.20: Roll and heave damping for bow (left figure) and quartering (right figure) seas.

During the model test period, problems related to the starboard vent valve system occurred. The shaft, connecting the starboard servo to the center vent valve blade, experienced a torsion fracture in one of the diameter transitions. This was probably due to its material choice and design. Brass was exploited for the starboard shaft, and radii were not used for the transitions between different shaft diameters. By not implementing radii in the transitions, greater stresses occur. This may lead to fractures when choosing a soft material like brass.
From Figure 6.20 it is seen that during control off there exists large differences between the starboard and port air cushion pressure for both cases. This occurs for identical commanded vent valve positions which is highly unexpected. Wave volume pumping induces peak-to-peak differences between the starboard and port pressure, but does not move their mean values. Therefore, it is expected that the pressure differences experienced in these tests occur due

to vent valve problems. The torsion fracture was discovered due to wrong starboard vent valve behaviour. The test setup did not include servo position/orientation sensors. However, the actual bias position was estimated by eye to be in the area of $30 - 40$ %, while it was commanded to be 50 %. It was also observed that the starboard vent valve did not utilize its entire operating area, which is $0 - 100$ %. It was operating approximately in the area of $0 - 60$ %.

By implementing a steel shaft for the connection between starboard servo and vent valve and also feed roll angular acceleration and heave linear acceleration back to the controller, the roll and heave damping percentages are expected to increase significantly.

6.2.6 Boarding Control System

The objectives of the Boarding Control System (BCS) was investigated for the split cushion design. In order to obtain appropriate feedback signals for control, an additional accelerometer was implemented at the bow. The objective was to damp vertical motions at the bow and heave motions at the center of gravity. The vertical motion at the bow is a combination of heave and pitch motions. In full scale, when the Wave Craft is free floating, the bow accelerometer is weighted more than the CG accelerometer. When the vessel is in contact with a wind turbine, the accelerometer weighting is vice versa. Therefore, tests which utilize only the bow accelerometer and tests that exploits both accelerometers were done.

From Table 6.15 and Figure 6.21 it is seen that even though the air cushion is longitudinally split, the control system is able to damp the bow displacement 49.2 % for bow seas with wave height and period 1 meter and 5 seconds, respectively. For this case heave damping in CG was not prioritized. Table 6.16 and Figure 6.21 illustrates that it is possible to damp vertical motions at the bow and CG, simultaneously. This is a trade-off. The bow motion damping decreases as the CG damping increases. From the figure it is seen that the vent valves, and hence also the pressures, operate in phase, as expected. The peak-to-peak value for the port pressure is significant larger than the value for the starboard pressure. This may be due to the wave volume pumping.

Table 6.15: Test N041A.
Bow motion damping. Regular seas.

Parameter	Value
Date	16.05.2017
Result	49.2 % bow damping
Wave direction	45°
Wave height	1 m
Wave period	5 s
Control on	15 s
Bias vent valves	50 %

Table 6.16: Test N041A.
Bow and heave motion damping. Regular seas.

Parameter	Value
Date	16.05.2017
Result	39.0 % bow damping 20.3 % heave damping
Wave direction	45°
Wave height	1 m
Wave period	5 s
Control on	15 s
Bias vent valves	50 %

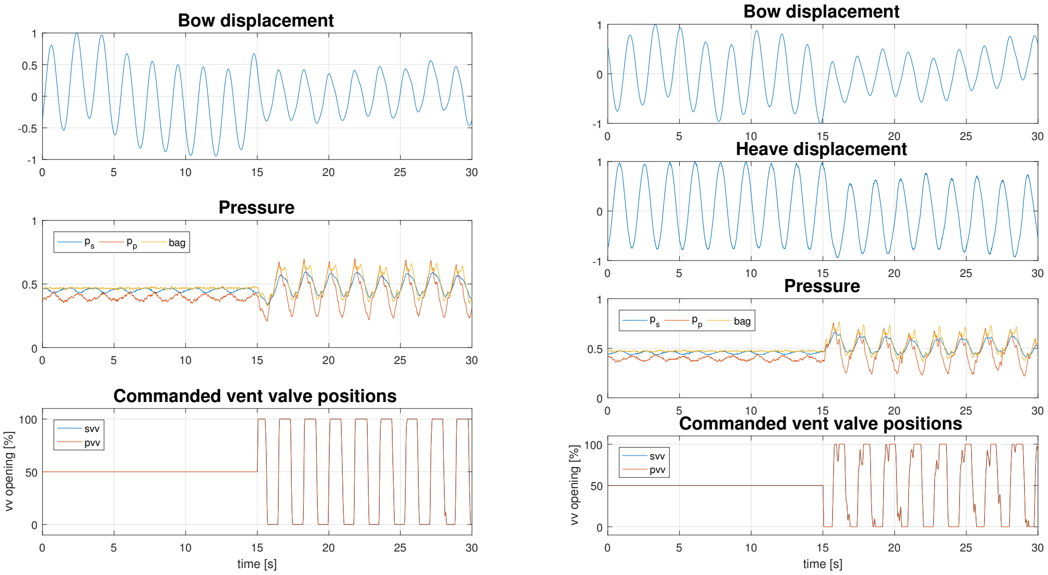

Figure 6.21: BCS response for bow seas. Both bow motion damping (left figure) and bow and heave motion damping (right figure) are shown.

Additional tests for damping of the vertical motions at the bow were performed. This was done for regular bow seas. The damping percentage achieved in waves with height 1 meter and a period of 8 seconds was found to be 74.6 %, while the control system was able to damp 28.7 % for waves with height and period of 2 meter and 5 seconds, respectively. This confirms the damping tendency experienced for roll damping. Greater damping is achieved for waves with lower height and longer period. These model tests indicate that the Boarding Control System is still able to perform its main objective when utilizing a split air cushion; namely, damping of vertical motions at the bow.

6.3 Mathematical Model Verification

In order to validate the mathematical models of the Wave Craft used in the simulators, the process plant model response is compared to the model test response for equal environmental conditions. Since the responses of the CPM and the PPM are quite similar, it is considered sufficient to exploit only the PPM for comparisons.

The pressure propagation experienced in the PPM simulations have step characteristics. This occurs since no restrictions are put on the in- and outflow of the cushions, meaning that both flows varies with step characteristics. This is not realistic and does not make sense from a practical point of view. Consequently, low-pass filters are implemented on the outflow from the cushions which lead to more realistic variations in the pressures. The cut-off frequency of the low-pass filters were tuned until the pressure response for the simulations was close to the pressure response obtained from the model tests. The vent valves were subject to similar commanded signals for the simulations and model tests.

Figure 6.22 illustrates the roll angle and pressure response when steps and sine waves are exploited for the commanded vent valve signals to generate roll motion. The figure indicates that the pressure response of the PPM is quite realistic for both cases when comparing to the the model tests (MT). By utilizing low-pass filters on the outflows from the cushions, it is seen that the pressure propagation experience realistic inertia. However, the low-pass filters also induce phase lag for the pressure response of the PPM. It is seen from the figure that the roll angle time series achieved for the simulations experience more deflections than the ones obtained from the model tests. This is either caused by deviations of the maximum roll moment achievable for the PPM and model vessel, or inertia differences. Note that there exists uncertainties for the damping coefficients utilized in the simulations. They are obtained from ShipX, where a fixed equilibrium pressure, p_0, for the cushions is assumed.

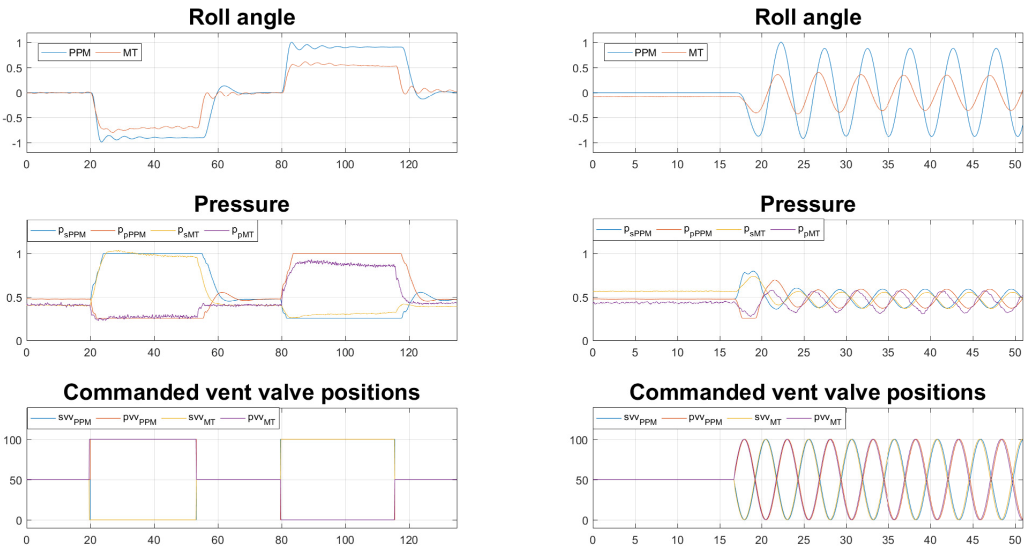

Figure 6.22: Roll generation for commanded step (left figure) and sine (right figure) vent valve signals

From Figure 6.23 it is seen that the roll angle and pressure response is similar when the commanded signals applied to the vent valves have same characteristics. The vessel is subject to beam seas with wave height of 1 meter and period of 5 seconds. For control on, the pressures for both the model test and simulation have zig-zag characteristics with approximately the same peak-to-peak values.

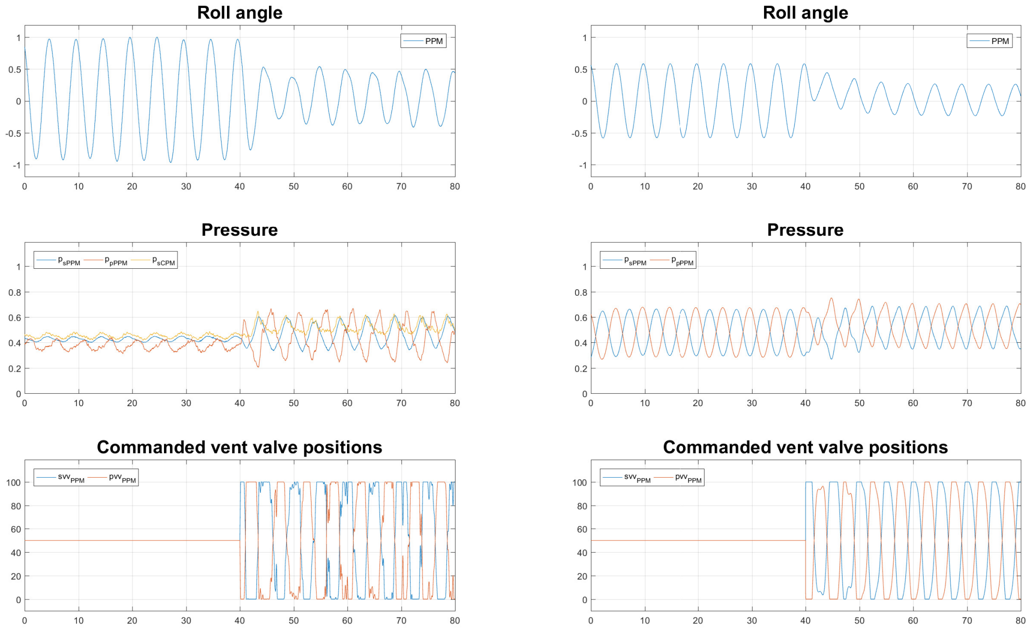

Figure 6.23: Roll damping in beam seas with wave height of 1 meters and period of 5 seconds, model test and PPM simulation, left and right figure, respectively.

The figure indicates that the simulations experience more pressure oscillations for control off than what is the case in reality. Equation 2.23 shows that the modeled nonlinear pressure propagation for the PPM varies dependent on Q_{in}, Q_{out}, Ω and $\dot{\Omega}$, which is volumetric air inflow, outflow, air cushion volume and rate of change of air cushion volume, respectively. Since the PPM pressures oscillates significantly more than the model test pressures, one or multiple of these parameters varies unrealistic much. As discussed the characteristic of the in- and outflow of the cushions are not realistic. Additionally, great uncertainties are related to Ω and $\dot{\Omega}$ which are dependent on cushion variables which may have highly nonlinear behaviour, meaning that they are difficult to model accurate. During the model test period, deviations from the modeled cushion areas, A_{c_i}, and transverse lever arms, y_{cp_i}, were observed for the model vessel. The separating wall has freedom to move at the bow and is restricted from moving at the aft bag, meaning that the cushions areas will change with triangle characteristics dependent on roll motions. They were modeled to change with rectangular characteristics. Consequently, the center of pressures for both cushions will deviate from the modeled ones, meaning that the longitudinally and transverse lever arms will differ.
Wave volume pumping, $\dot{V}_{0_i}$, and its integral, V_{0_i}, for both cushions are also uncertain. As seen from (2.19) and (2.20), both parameters are dependent on wave amplitude, $\bar{\xi}$. The integral of wave volume pumping, V_{0_i}, represents the volume occupied by waves inside the cushions, from now on denoted the wave volume. Equation (2.19) indicates that the wave volume is equal to the wave amplitude, $\bar{\xi}$, multiplied with a sine wave with period and phase, meaning that the waves present inside the cushions are identical to the ones outside the cushions. This

assumption may not hold in reality. It is expected that identical waves inside and outside the cushions only occur when the vessel is restrained from oscillating. Since the vessel follows the waves in a smooth manner, the wave height inside the cushions can not be equal to the wave height outside the cushions. It is also expected that the side hulls and separating wall will damp the incident waves, reducing their wave height. Therefore, the wave volume pumping and wave volume inside the cushions are assumed to have unrealistic peak-to-peak values. Hence, the cushion volumes and their rates of change will differ for the model vessel and the simulators, inducing different peak-to-peak values for the pressure oscillations.

The roll angle plots for the model vessel and simulator indicate that inertia differences exist, as previously discussed. The roll angle obtained from simulations oscillates approximately 40 % less than the roll angle response experienced for the model vessel This may also be caused by resonance area deviations. Even though the maximum achievable pressure-induced roll moment is expected to deviate between the simulation and model test, it is seen that the relative damping percentage for both cases are approximately equal for close to identical commanded vent valve positions.

Chapter 7

Discussion

7.1 Separating Wall

It has been proven that roll motions can be damped significantly by utilizing the current separating wall design. However, it is expected that even better performance can be obtained by excluding multiple potential weaknesses from the design.

One of these weaknesses is the T-duct. There may exist an air flow from the cushion with high pressure to the cushion with low pressure over the T-duct, which induces less pressure potential and thereby less roll damping. If the separating wall concept is considered implemented for the full scale vessel, the T-duct design is not recommended. However, it is still considered a great idea to supply the bag fan with the highest air cushion pressure. In order to do this, both cushion pressures could be compared in some valve, where the highest pressure is applied to the bag fan.

It is also considered disadvantageous to obtain the air cushion pressures by utilizing a mechanism installed inside the separating wall, like the T-duct. Leakages from the separating wall to the air cushions may occur at these locations, inducing a pressure drop in the wall. A fixed mechanism inside the wall will probably reduce its freedom to move. This is a downside if the separating wall should be able to move in order to increase the achievable pressure-induced roll moment. Therefore, it is recommended to obtain the air cushion pressures by drilling a hole for each chamber and using hoses to supply the valve with both pressures.

It should also be considered to fix the separating wall rather inside than outside the aft bag. This will lead to that the separating wall is drained through the holes in the aft bag, instead of through the current implemented draining channel.

The air cushion areas are crucial for the maximum achievable pressure-induced roll control moment. Their observed behaviour during the model tests were unexpected. Currently, the air cushion areas are changing with triangle characteristics since the separating wall is restrained from moving at the aft bag location and has freedom to move at the finger shirt location. If the wall is modified to be able to move at the aft bag location, it is expected that the air cushion areas can change with rectangular characteristics which may lead to greater changes in cushion areas. Hence, the pressure potential will increase and thereby also the pressure-induced roll moment. However, it is expected that the aft bag will restrain the separating wall from moving to some extent, when fixing them together. In order to prevent leakages between the two chambers, the separating wall and the aft bag must be fixed.

Due to the inertia of the flexible separating wall, a fixed separating wall concept should also be investigated. The flexibility may not work as intended. By design, the flexible separating wall should be vertical for all roll angles. The model tests indicate that this may not be the case, especially not near the aft bag. However, if the separating wall tends to be vertical, the starboard cushion area will be less than the port cushion area for a given positive roll angle. For this case, it is actually desired that the cushion areas are vice versa, in order to induce as large counteracting roll moment as possible. Consequently, it is expected that a fixed separating wall, that is not able to move, will achieve even better roll damping performance than a flexible design. A different approach may be to prevent the flexible separating wall from moving at the finger shirt location and thereby avoid the entire separating wall to tend to vertical position. For both approaches it is recommended to keep the dimensions of the separating wall to avoid separating wall/water line interactions during transit. The main drawback by exploiting a fixed wall instead of a flexible wall is that it may experience heavier stresses in the connection separating wall/wet deck when the vessel is subject to waves.

For the model vessel a stronger bag fan should be considered implemented. For this project the bag fan is used to pressurize both the aft bag and separating wall. From the model test responses it is seen that this pressure may be below the highest air cushion pressure. By design it should have been vice versa, which indicate that the bag fan may be too weak. The current separating wall exploits a wooden beam too keep the bottom width. This is not the best solution, taking the buoyancy force from the wood into account. Different materials should be considered implemented.

7.2 Mathematical Models and Simulations

Both the control plant model (CPM) and the process plant model (PPM) provide realistic simulations when comparing their response. Simulation analysis implies that their response is more similar than expected, when taking the complexity of the PPM into account. The PPM contains parameters the CPM does not have; couplings between DOFs, multiple damping terms, fluid memory effects and nonlinear pressures. Therefore, greater differences for the experienced responses were expected. The CPM is more accurate than predicted, making it excellent suited for control system design, observer design and stability analysis.

For both models great uncertainty concerning wave volume pumping is present. This parameter is considered to have an unrealistic large effect on the air cushion pressures. An approach to model this parameter accurate is to reduce the influence of wave volume pumping until the pressure response for a model test and a simulation, subject to equal environmental conditions, coincides.

Several air cushion variables for the CPM are assumed constant, while they are varying for the PPM. Due to the behaviour of the separating wall, the modeled air cushion areas and longitudinally and transverse lever arms are inaccurate. Since the air cushions change with triangle characteristics for the current design(as discovered during model-testing), the volume center, and thereby the center of pressure, for both cushions deviates from the modeled ones for both the PPM and CPM.

Leakages and inertia for the in- and outflow are not modeled. Instead, saturation is utilized to bound the pressure dynamics, which is not considered to represent the pressure dynamics in a good manner. Both leakages and in- and outflow inertia should be modeled to obtain realistic pressure propagation. The pressure dynamics achieved by low-pass filtering the outflow is not considered to be accurate, since phase lag occur for the response.

7.3 Instrumentation

The model tests confirm that a 3-axis accelerometer and gyro provide sufficient performance in order to obtain accurate and precise measurements of the roll angle and roll rate. The angles obtained from the accelerometer are based on the assumption that the surge and sway accelerations are sufficiently small. This makes the current setup valid only for zero speed applications. During the model tests, the vessel was also held in place by springs in sway and surge, so the accelerations when the vessel is free floating might be more significant and introduce problems with calculating the angles from the gravitational components. Additional sensors could have been implemented for the full scale vessel to increase the accuracy. This can be done by estimating the surge and sway acceleration using a GPS. When these parameters are known, more accurate estimates of the gravitational components acting in sway and surge are obtained, inducing more accurate angle estimates.

7.4 Control System and Observer Design

The control systems implemented on the CompactRIO worked as intended. Additionally, a stability analysis based on the CPM is performed which indicate that the states are ultimately bounded by a small bound. The foundation for a hybrid controller dependent on environmental conditions is designed. In real life, an operator will not set the controller manually for every change in heading, environmental conditions, etc. Therefore, hybrid control is considered the most practical solution when combining multiple DOF motion damping. By utilizing the split cushion design, the vertical motions can be damped, meaning that roll damping can be prioritized for beam seas, while pitch and heave damping may be prioritized for bow seas. By estimating the difference between the wave direction and vessel heading, $\hat{\psi}_{wave} - \psi_{vessel}$, gain scheduling can be applied automatically to assign a gain matrix, $\boldsymbol{K}$, to the controller dependent on the vessel heading relative to the wave direction. For this idea to work, the wave direction must be estimated by an observer or measured by suitable sensors.

Both Kalman filters provided accurate estimates if tuned correctly, although the response of the Kalman filter utilizing the CPM indicated that the mathematical model can not be trusted. This Kalman filter is highly dependent on air cushion variables like cushion areas and lever arms. In order to obtain great noise suppression, trust must be given to the mathematical model, meaning that these cushion variables must be modeled accurate relative to their behaviour in reality.

Since the pressure-induced roll moment is dependent on: air cushion pressures, cushion areas and transverse lever arms, which all vary with time, then the moment must be modeled with nonlinear dynamics to obtain smooth estimates. The CPM is a linear model, which is only valid for linearized pressure dynamics, meaning that it is not convenient for observer design. By implementing the PPM in the nonlinear passive observer, more accurate state estimation is expected. However, the fluid memory effects and nonlinear pressure dynamics will increase the complexity of the observer significantly leading to implementation challenges. In order to estimate the nonlinear pressures accurate, the in- and outflows of the cushions, wave volume pumping and cushion variables must be modeled as accurate as possible. Meaning, extensively testing and modeling must be executed to obtain sensible characteristics of these parameters behaviour. An observer is considered to induce great advantages, e.g. the input angle to the hybrid control system can be estimated here. Due to the complexity of the observer and since it did not work as intended, the angle estimator and low-pass filtered rates were fed back to the controller. Both the IMU KF and low-pass filter provided excellent feedback signals in the sense that they were smooth, accurate and precise.

7.5 Model Tests

The model tests illustrate that the roll damping control system works as intended. Roll motions are damped significant for various wave heights, periods and directions. Hence, the objectives for this thesis are reached. Additionally, by feeding roll and heave rate back to the controller, both roll and heave motions are damped.

Chapter 8

Conclusion

A roll damping control system was implemented on a model scale surface effect ship with longitudinally split air cushions. Model tests indicate that the split cushion design and roll damping control system should be considered tried out on a full scale SES. Roll motions are damped significantly for various wave heights, periods and directions. Additionally, it is possible to damp both roll and heave motions, simultaneous, and also vertical bow motions when exploiting the split cushion design. Therefore, the objectives of the Boarding Control System can still be fulfilled, when using a split cushion design.

Both a linear control plant model and a nonlinear process plant model are developed. Their response is surprisingly similar when both simulators are subject to equal environmental conditions. When comparing simulations and model tests inertia and maximum pressure-induced roll moment differences were discovered. This is expected and lead to different peak-to-peak values for the roll angle. Since the modeling of the air cushion variables deviates from the corresponding cushion variables for the model scale vessel, the pressure-induced roll moment will deviate. The process plant model should be further developed to include the correct cushion variables behaviour, wave volume pumping characteristics and air cushion leakages.

An observer which provides smooth, accurate and precise estimates should be considered implemented for the full scale vessel. Since the cushion pressures vary highly nonlinear, the process plant model must be used for the observer design. A foundation for a hybrid controller which is able to damp heave, roll and pitch motions based on environmental conditions is designed. By estimating the wave direction in an observer, this parameter can be applied to the switching mechanism of the hybrid controller.

The separating wall design works as intended. However, even more roll damping is expected to be present if a fixed separating wall is exploited.

Bibliography

Adams, J. D., Ernest, A. W. and Lewis, J. H. (1983), Design, development and testing of a digital ride control system for the xr-id surface effect ships; part i - classical control, Technical Report MD-AR-1180-1, Maritime Dynamics, Inc, Tacoma, Washington.

Auestad, Ø. F. (2015), The Boarding Control System: Modelling and Control of a Surface Effect Ship for improved accessibility to Offshore Wind Turbines, PhD thesis, Department of Engineering Cybernetics, Norwegian University of Science and Technology.

Bryn, H. E. (2016), Roll control system on a surface effect ship, Technical report, Department of Engineering Cybernetics, Norwegian University of Science and Technology.

Bua, N. H. and Vamråk, V. M. (2016), Sway control on a surface effect ship, Master's thesis, Department of Marine Technology, Norwegian University of Science and Technology.

Butler, E. A. (1985), 'The surface effect ship', *Naval Engineers Journal* **97**(2), 200–258.

Cummins, W. E. (1962), The impulse response function and ship motion, Technical report, Department of the Navy David Taylor Model Basin. Hydrodynamics Laboratory, USA.

Faltinsen, O. M. (2005), *Hydrodynamics of High-Speed Marine Vehicles*, Cambridge University Press, Cambridge, UK.

Fossen, T. I. (2011), *Handbook of Marine Craft Hydrodynamics and Motion Control*, John Wiley & Sons, UK.

Freescale, S. (2015), *Allan Variance: Noise Analysis for Gyroscopes*, Austin, Texas, USA.

Inc., K. I. (2014), *Guide to Comparing Gyro and IMU Technologies – Micro-Electro-Mechanical Systems and Fiber Optic Gyros*.

Kaplan, P. and Davis, S. (1978), System analysis techniques for designing ride control system for ses craft in waves., *in* 'Proceedings of the 5th Ship Contr. Syst. Symp.', Annapolis, Maryland, USA.

Khalil, H. K. (2002), *Nonlinear Systems*, Macmillan, New York, USA.

Kristiansen, E. and Egeland, O. (2003), Frequency-dependent added mass in models for controller design for wave motion damping, *in* ‘Proceedings of the IFAC Conference on Maneuvering and Control of Marine Craft (MCMC’03)’, Girona, Spain.

Kristiansen, E., Hjulstad, Å. and Egeland, O. (2005), ‘State-space representation of radiation forces in time-domain vessel models’, *Ocean Engineering* **OE-32**, 2195–2216.

Lavis, D. R. (1998), Forty-plus years of hovercraft development., *in* ‘Proceedings of the 25th, Canadian Air Cushion Technology Society: CACTS ’98’, Canadian Aeronautics and Space Institute.

O’Hanlon, J. F. and McCauley, M. E. (1974), ‘Motion sickness incidence as a function of vertical sinusoidal motion’, *Aerospace medicine* **AM-45(4)**, 366–369.

Perez, T. (2005), *Ship Motion Control: Course Keeping and Roll Reduction using Roll and Fins. Advances in Industrial Control Series*, Springer-Verlag, London, UK.

Sørensen, A. J. (2013), *Propulsion and Motion Control of Ships and Ocean Structures*, Akademika forlag, Trondheim, Norway.

Sørensen, A. J. and Egeland, O. (1995), ‘Design of ride control system for surface effect ships using dissipative control’, *Automatica* **31**, 183–199.

Tønnessen, J. (2016), Roll control system on a surface effect ship, Technical report, Department of Engineering Cybernetics, Norwegian University of Science and Technology.

Umoe, M. (2017), ‘Discover the new generation of wavecraft $^{\text{TM}}$ crew transfer vessels’.
URL: *https://www.wavecraft.no*

Vetus (2011), *Roll damping system Operating manual and installation instructions*, Vetus n.v. Schiedam, Holland.

Vik, B. (2014), Integrated satellite and inertial navigation systems, Technical report, Norwegian University of Science and Technology.

WindEurope (2017), *The European offshore wind industry – key trends and statistics 2016*, WindEurope, WindEurope, Brussels, Belgium.

Appendix A

System Matrices

A.1 Control Plant Model

$$\boldsymbol{A} = \begin{bmatrix} 0 & 0 & 0 & \frac{1}{m+A_{33}} & 0 & 0 & 0 & 0 \\ 0 & 0 & 0 & 0 & \frac{1}{I_{44}+A_{44}} & 0 & 0 & 0 \\ 0 & 0 & 0 & 0 & 0 & \frac{1}{I_{55}+A_{55}} & 0 & 0 \\ -C_{33} & 0 & 0 & -\frac{B_{33}}{m+A_{33}} & 0 & 0 & A_c p_0 & A_c p_0 \\ 0 & -C_{44} & 0 & 0 & -\frac{B_{44}}{I_{44}+A_{44}} & 0 & -y_{cp} A_c p_0 & y_{cp} A_c p_0 \\ 0 & 0 & -C_{55} & 0 & 0 & -\frac{B_{55}}{I_{55}+A_{55}} & -x_{cp} A_c p_0 & -x_{cp} A_c p_0 \\ 0 & 0 & 0 & -\frac{\rho_{c0} A_c}{K1(m+A_{33})} & \frac{y_{cp} \rho_{c0} A_c}{K1(I_{44}+A_{44})} & \frac{x_{cp} \rho_{c0} A_c}{K1(I_{55}+A_{55})} & -\frac{K3}{K1} & 0 \\ 0 & 0 & 0 & -\frac{\rho_{c0} A_c}{K1(m+A_{33})} & -\frac{y_{cp} \rho_{c0} A_c}{K1(I_{44}+A_{44})} & \frac{x_{cp} \rho_{c0} A_c}{K1(I_{55}+A_{55})} & 0 & -\frac{K3}{K1} \end{bmatrix} \tag{A.1}$$

$$\boldsymbol{B} = \begin{bmatrix} 0 & 0 \\ 0 & 0 \\ 0 & 0 \\ 0 & 0 \\ 0 & 0 \\ 0 & 0 \\ \frac{K2}{K1} & 0 \\ 0 & \frac{K2}{K1} \end{bmatrix} \tag{A.2}$$

$$\boldsymbol{C} = \begin{bmatrix} 0 & 1 & 0 & 0 & 0 & 0 & 0 & 0 \\ 0 & 0 & 1 & 0 & 0 & 0 & 0 & 0 \\ 0 & 0 & 0 & \frac{1}{m+A_{33}} & 0 & 0 & 0 & 0 \\ 0 & 0 & 0 & 0 & \frac{1}{I_{44}+A_{44}} & 0 & 0 & 0 \\ 0 & 0 & 0 & 0 & 0 & \frac{1}{I_{55}+A_{55}} & 0 & 0 \\ 0 & 0 & 0 & 0 & 0 & 0 & 1 & 0 \\ 0 & 0 & 0 & 0 & 0 & 0 & 0 & 1 \end{bmatrix} \tag{A.3}$$

$$\boldsymbol{E} = \begin{bmatrix} 0 & 0 & 0 & 0 & 0 \\ 0 & 0 & 0 & 0 & 0 \\ 0 & 0 & 0 & 0 & 0 \\ 1 & 0 & 0 & 0 & 0 \\ 0 & 1 & 0 & 0 & 0 \\ 0 & 0 & 1 & 0 & 0 \\ 0 & 0 & 0 & \frac{\rho_{c0}}{K1} & 0 \\ 0 & 0 & 0 & 0 & \frac{\rho_{c0}}{K1} \end{bmatrix} \tag{A.4}$$

$$\bar{\boldsymbol{E}} = \begin{bmatrix} 0 & 0 & 0 \\ 0 & 0 & 0 \\ 0 & 0 & 0 \\ 1 & 0 & 0 \\ 0 & 1 & 0 \\ 0 & 0 & 1 \\ 0 & 0 & 0 \\ 0 & 0 & 0 \end{bmatrix} \tag{A.5}$$

A.2 Process Plant Model

$$\boldsymbol{M}_{RB} = \begin{bmatrix} 94260 & 0 & 0 & 0 & -211142 & 0 \\ 0 & 94260 & 0 & 211142 & 0 & 0 \\ 0 & 0 & 94260 & 0 & 0 & 0 \\ 0 & 211142 & 0 & 2159354 & 0 & -102801 \\ -211142 & 0 & 0 & 0 & 4210576 & 0 \\ 0 & 0 & 0 & -102801 & 0 & 4115523 \end{bmatrix} \tag{A.6}$$

$$\boldsymbol{M}_A(\infty) = \begin{bmatrix} 3194 & 0 & 0 & 0 & 0 & 0 \\ 0 & 107013 & 0 & -51508 & 0 & -210329 \\ 0 & 0 & 20767 & 0 & 45306 & 0 \\ 0 & -21875 & 0 & 395912 & 0 & 354713 \\ 0 & 0 & 52227 & 0 & 669776 & 0 \\ 0 & -164343 & 0 & 245581 & 0 & 3933285 \end{bmatrix} \tag{A.7}$$

$$\boldsymbol{B}_v(\infty) = \begin{bmatrix} 3445 & 0 & 0 & 0 & 0 & 0 \\ 0 & 115432 & 0 & 0 & 0 & 0 \\ 0 & 0 & 0 & 0 & 0 & 0 \\ 0 & 0 & 0 & 520000 & 0 & 0 \\ 0 & 0 & 0 & 0 & 4200000 & 0 \\ 0 & 0 & 0 & 0 & 0 & 4103044 \end{bmatrix} \tag{A.8}$$

$$\boldsymbol{C} = \begin{bmatrix} 0 & 0 & 0 & 0 & 0 & 0 \\ 0 & 0 & 0 & 0 & 0 & 0 \\ 0 & 0 & 356601 & 0 & 232007 & 0 \\ 0 & 0 & 0 & 4458662 & 0 & -1277040 \\ 0 & 0 & 232007 & 0 & 9003844 & 0 \\ 0 & 0 & 0 & 0 & 0 & 0 \end{bmatrix} \tag{A.9}$$

Appendix B

General Arrangements

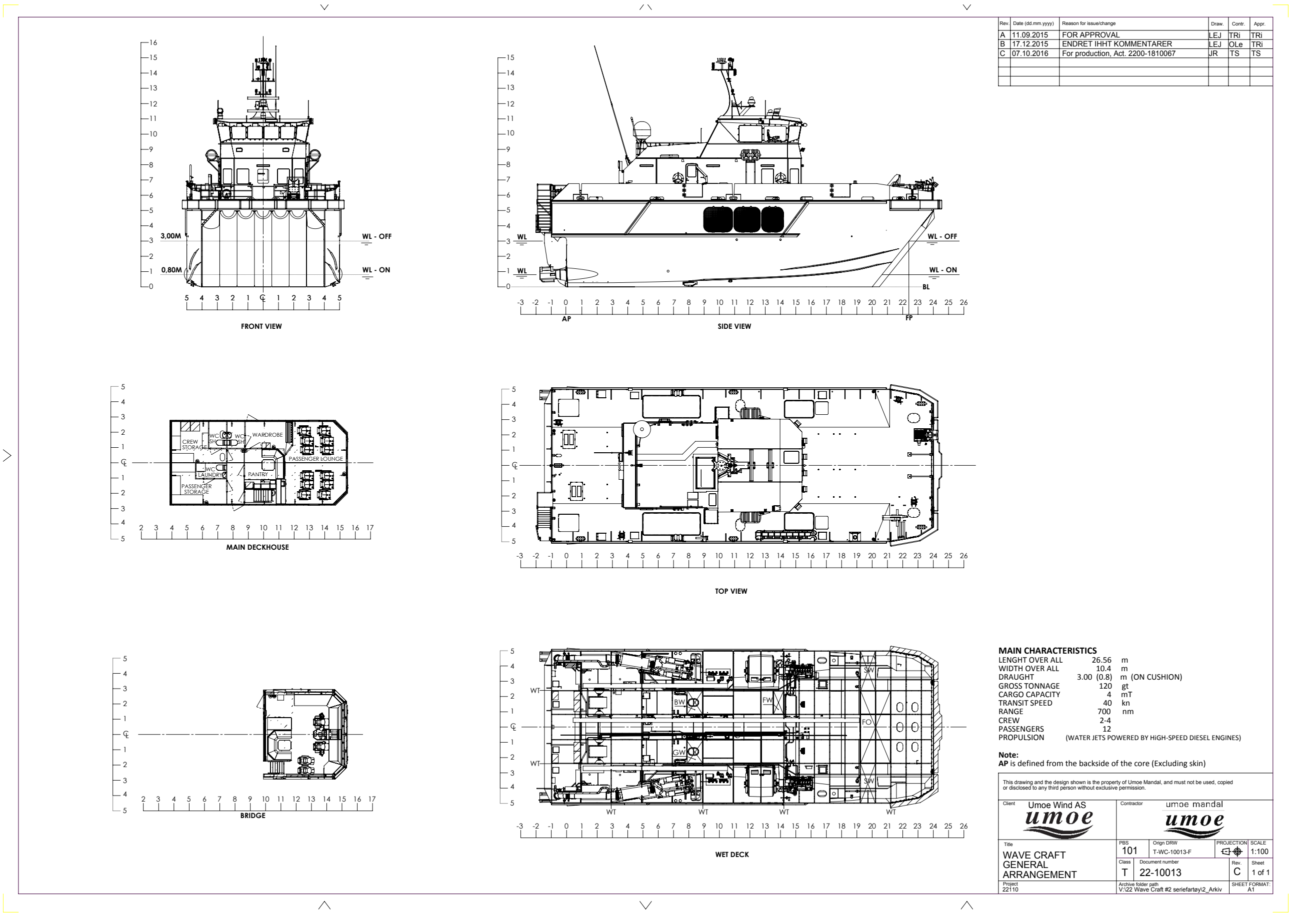

Rev.	Date (dd.mm.yyyy)	Reason for issue/change	Draw.	Contr.	Appr.
A	11.09.2015	FOR APPROVAL	LEJ	TRi	TRi
B	17.12.2015	ENDRET IHHT KOMMENTARER	LEJ	OLe	TRi
C	07.10.2016	For production, Act. 2200-1810067	JR	TS	TS

MAIN CHARACTERISTICS

LENGHT OVER ALL	26.56	m
WIDTH OVER ALL	10.4	m
DRAUGHT	3.00 (0.8)	m (ON CUSHION)
GROSS TONNAGE	120	gt
CARGO CAPACITY	4	mT
TRANSIT SPEED	40	kn
RANGE	700	nm
CREW	2-4	
PASSENGERS	12	
PROPULSION	(WATER JETS POWERED BY HiGH-SPEED DIESEL ENGINES)	

Note:
AP is defined from the backside of the core (Excluding skin)

This drawing and the design shown is the property of Umoe Mandal, and must not be used, copied or disclosed to any third person without exclusive permission.

Client: Umoe Wind AS		Contractor: umoe mandal			
Title: WAVE CRAFT GENERAL ARRANGEMENT	PBS: 101	Orign DRW: T-WC-10013-F		PROJECTION	SCALE: 1:100
	Class: T	Document number: 22-10013		Rev.: C	Sheet: 1 of 1
Project: 22110	Archive folder path: V:\22 Wave Craft #2 seriefartøy\2_Arkiv			SHEET FORMAT: A1	

Figure B.1: General arrangements Wave Craft

Appendix C

Simulink Diagrams for Real-time Control

C.1 Top View

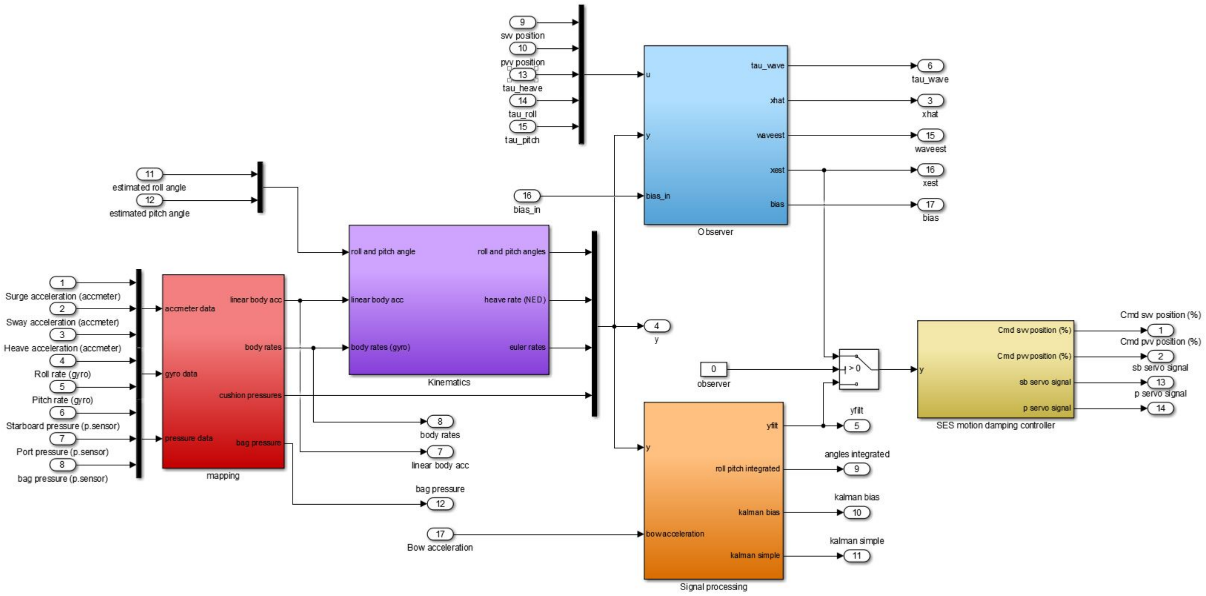

Figure C.1: Top view of the Simulink diagram.

C.2 Mapping and Calibration

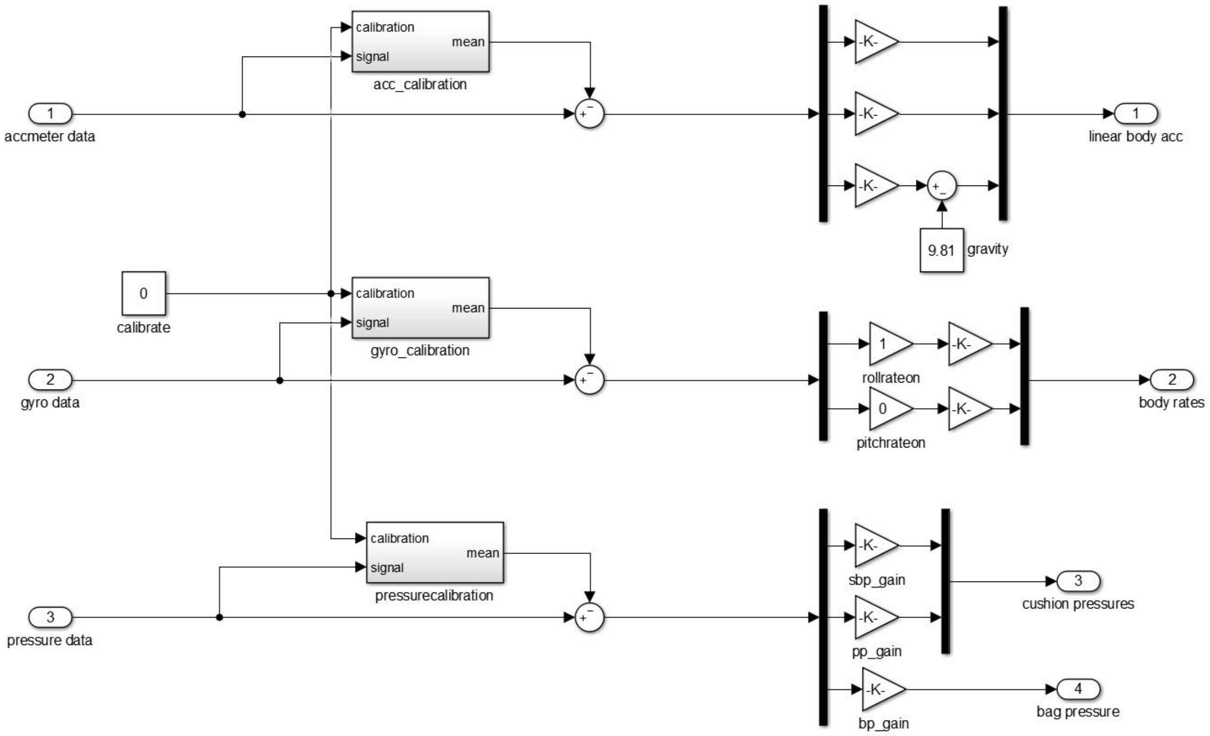

Figure C.2: Sensor mapping from voltage to measurement quantity.

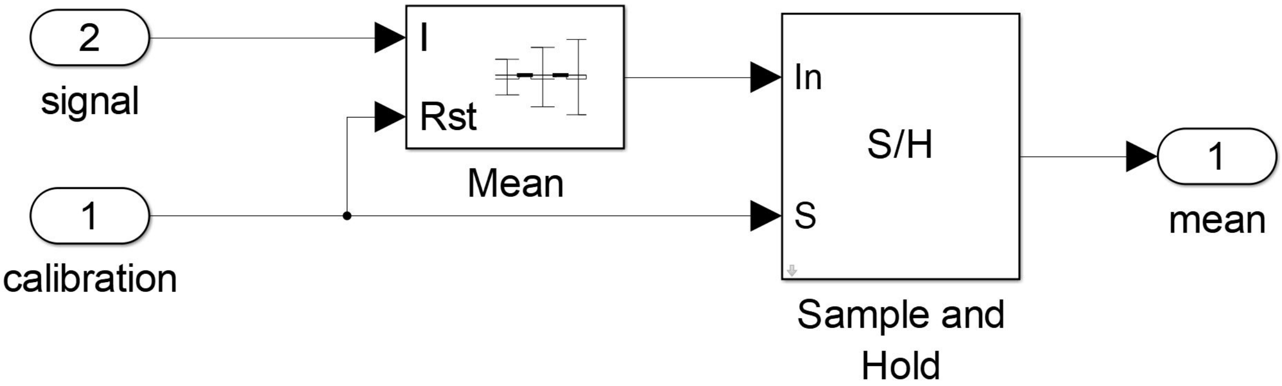

Figure C.3: Calibration routine.

C.3 Kinematics

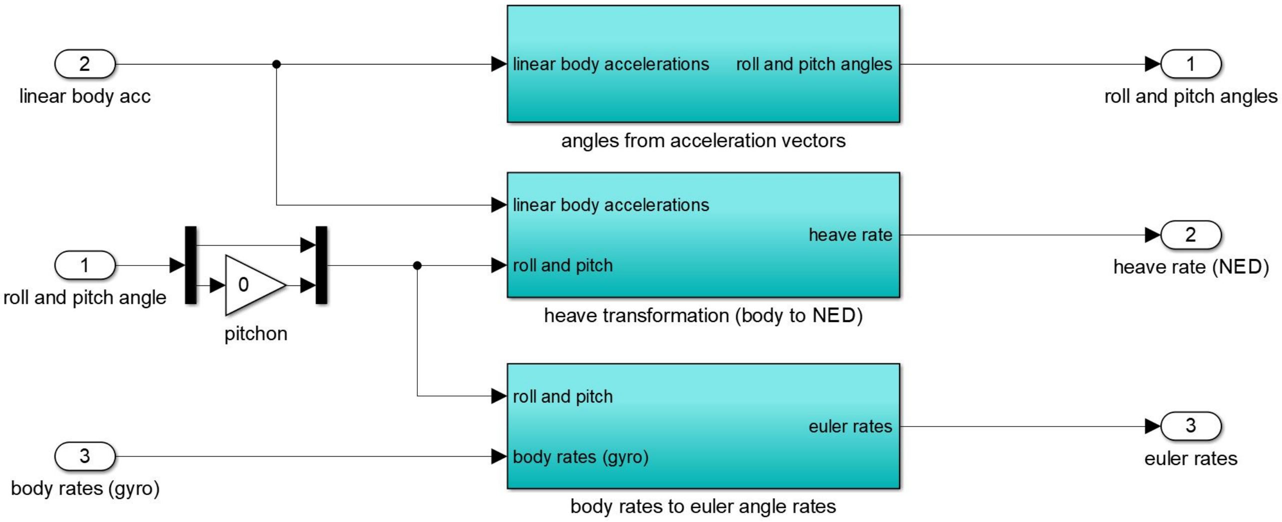

Figure C.4: Kinematic transformation blocks.

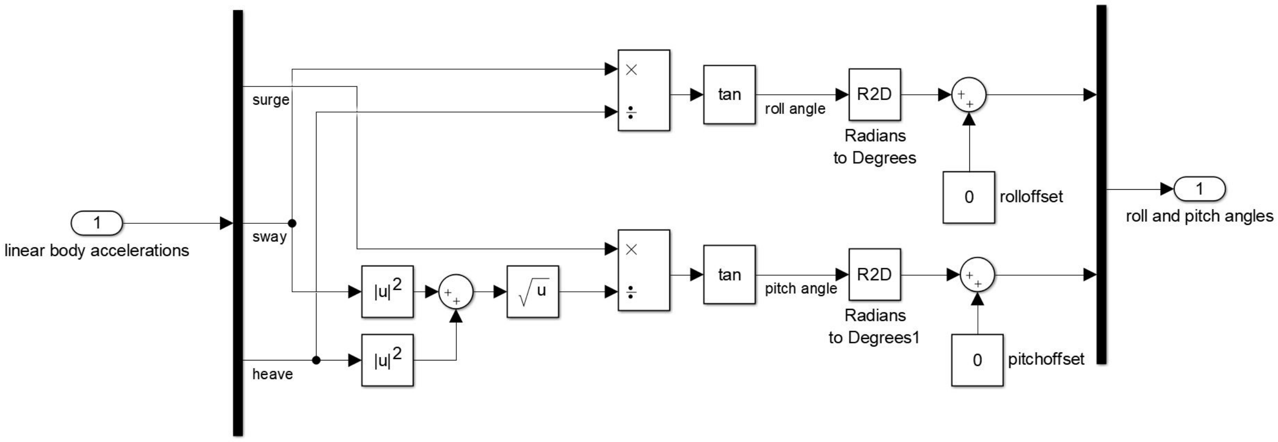

Figure C.5: Acceleration to angles.

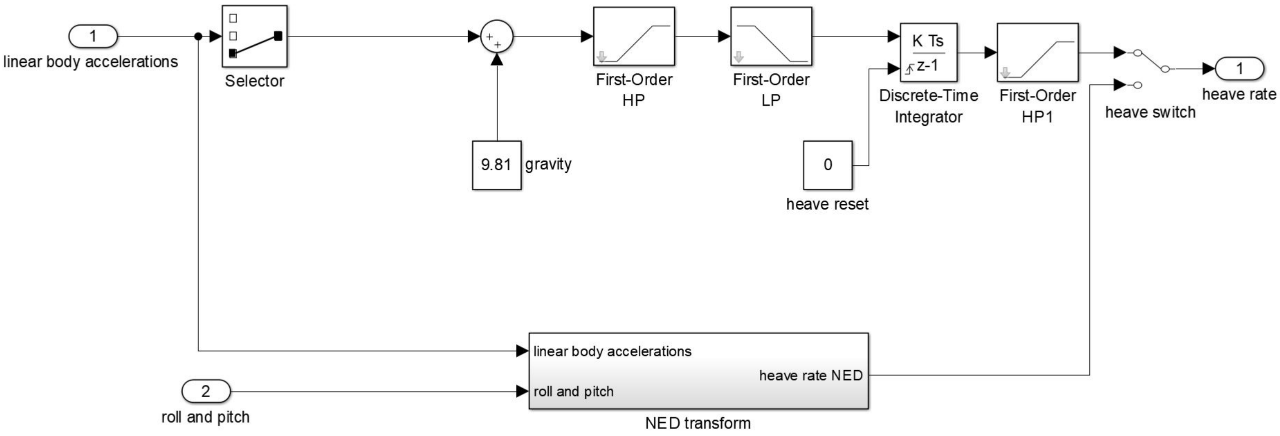

Figure C.6: Heaverate from body to NED. (unused)

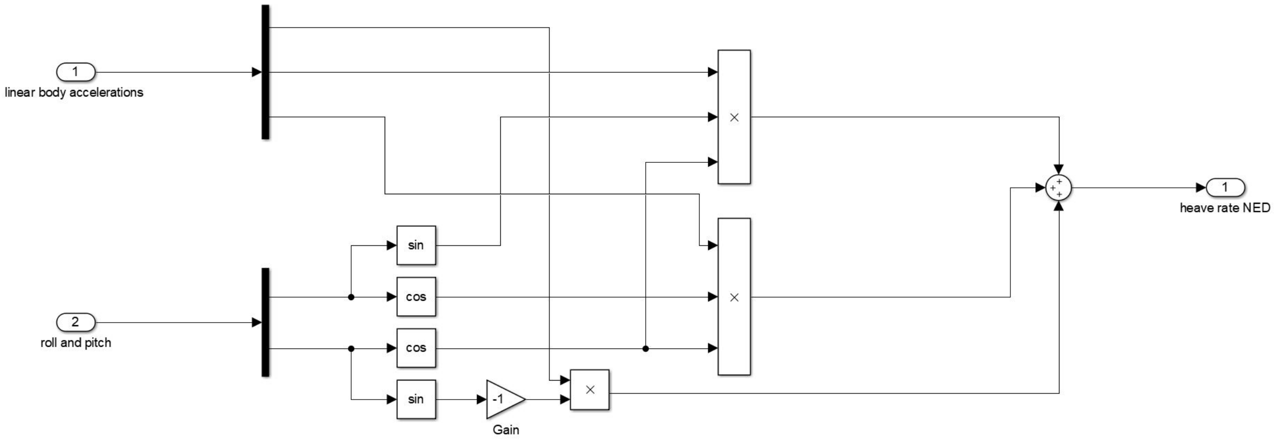

Figure C.7: Heaverate in body with filtering.

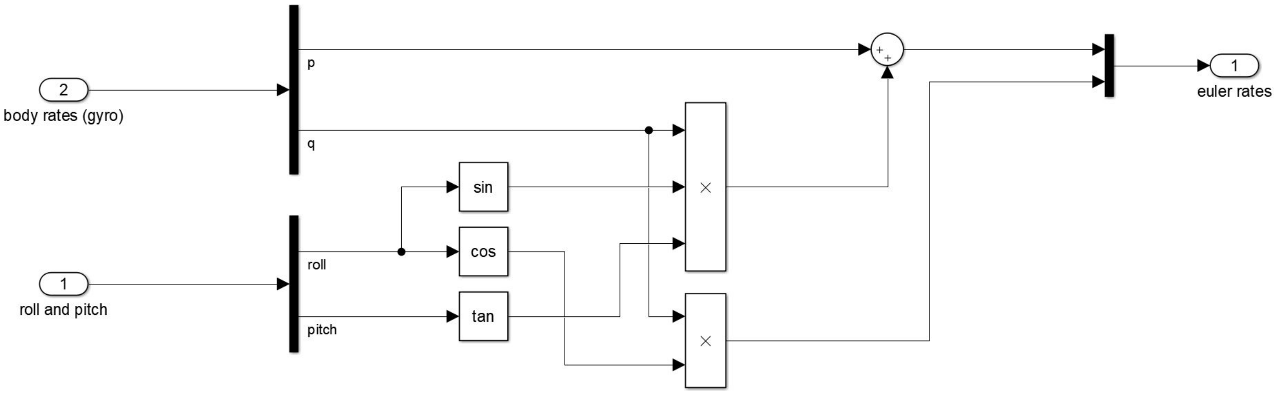

Figure C.8: Body rates to Euler rates.

C.4 Observer

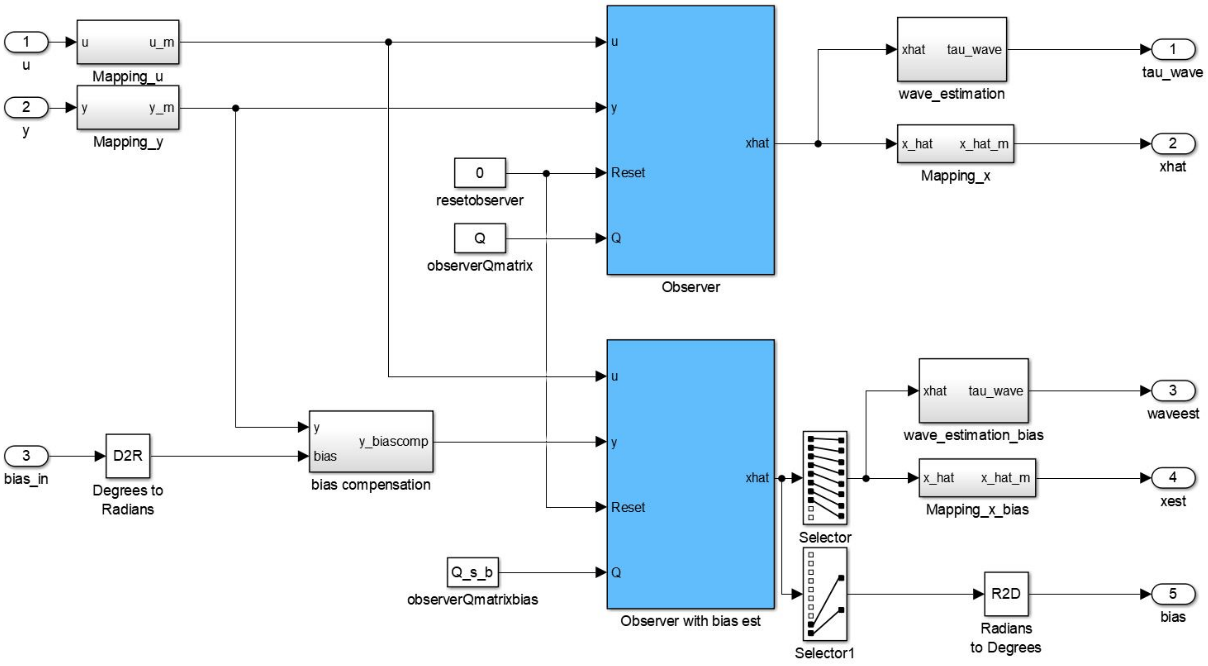

Figure C.9: CPM KF with and without bias estimation.

C.5 Signal Processing

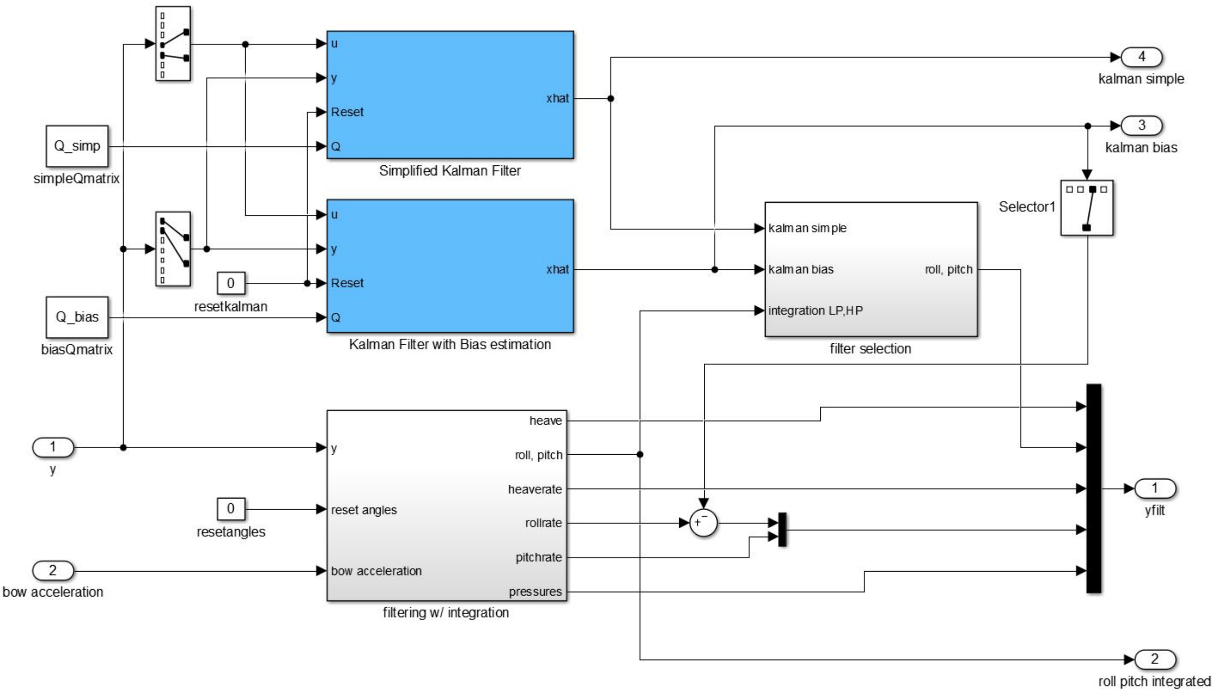

Figure C.10: Signal processing and IMU KF.

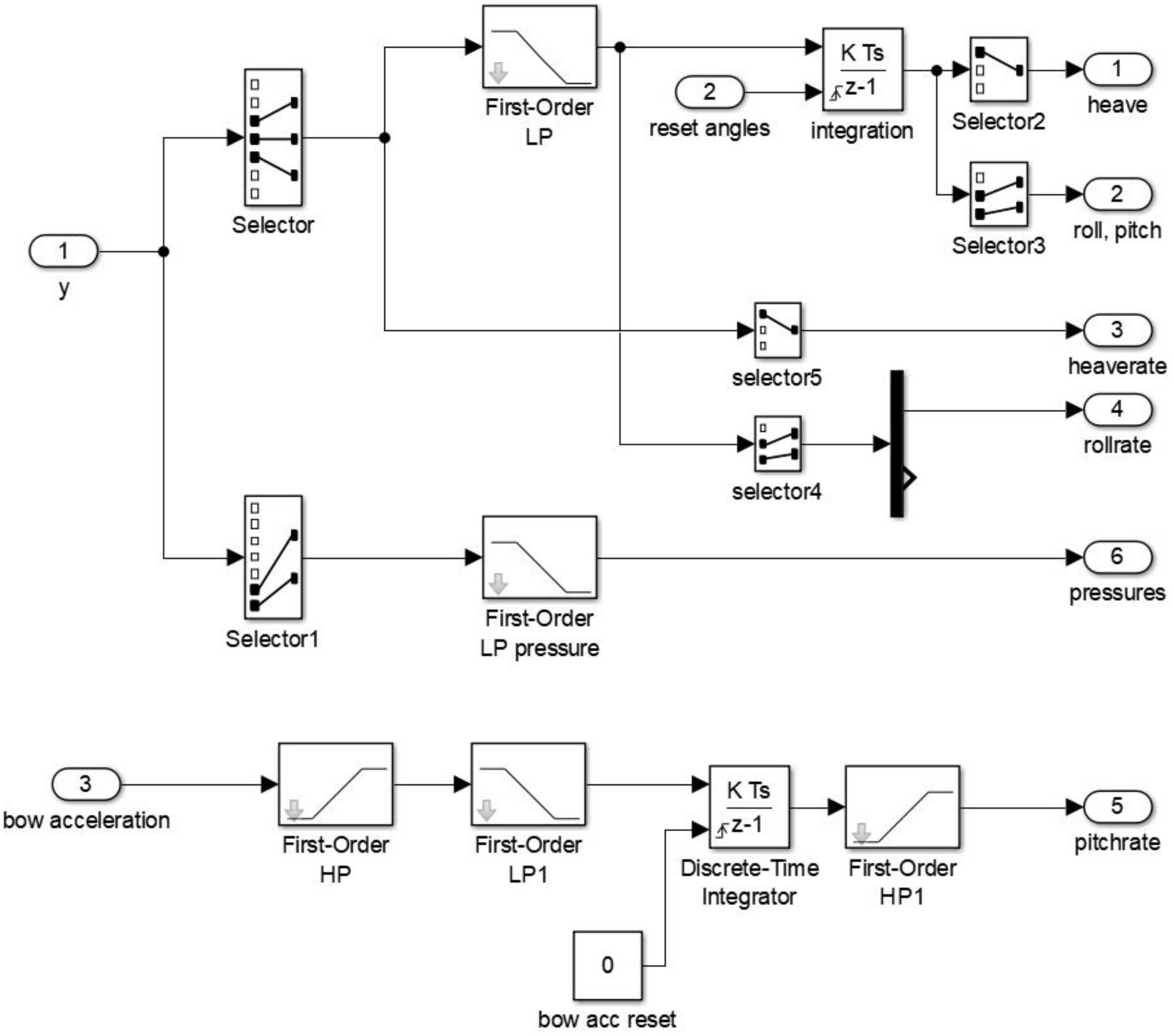

Figure C.11: Filtering.

C.6 SES Motion Damping Controller

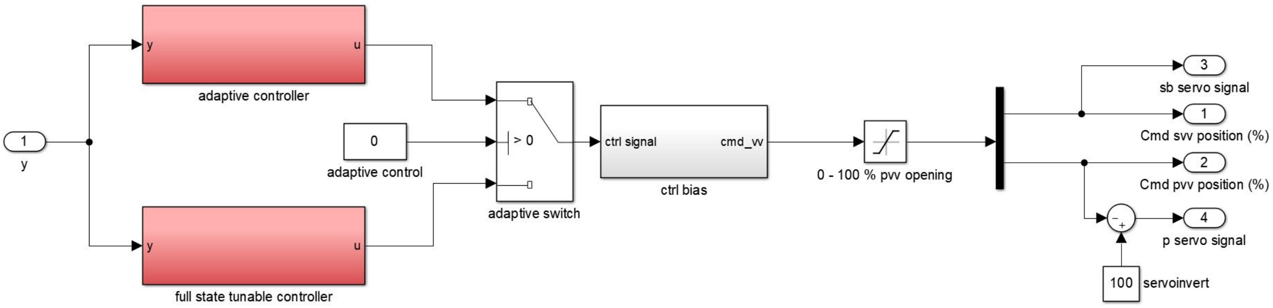

Figure C.12: Control system top view.

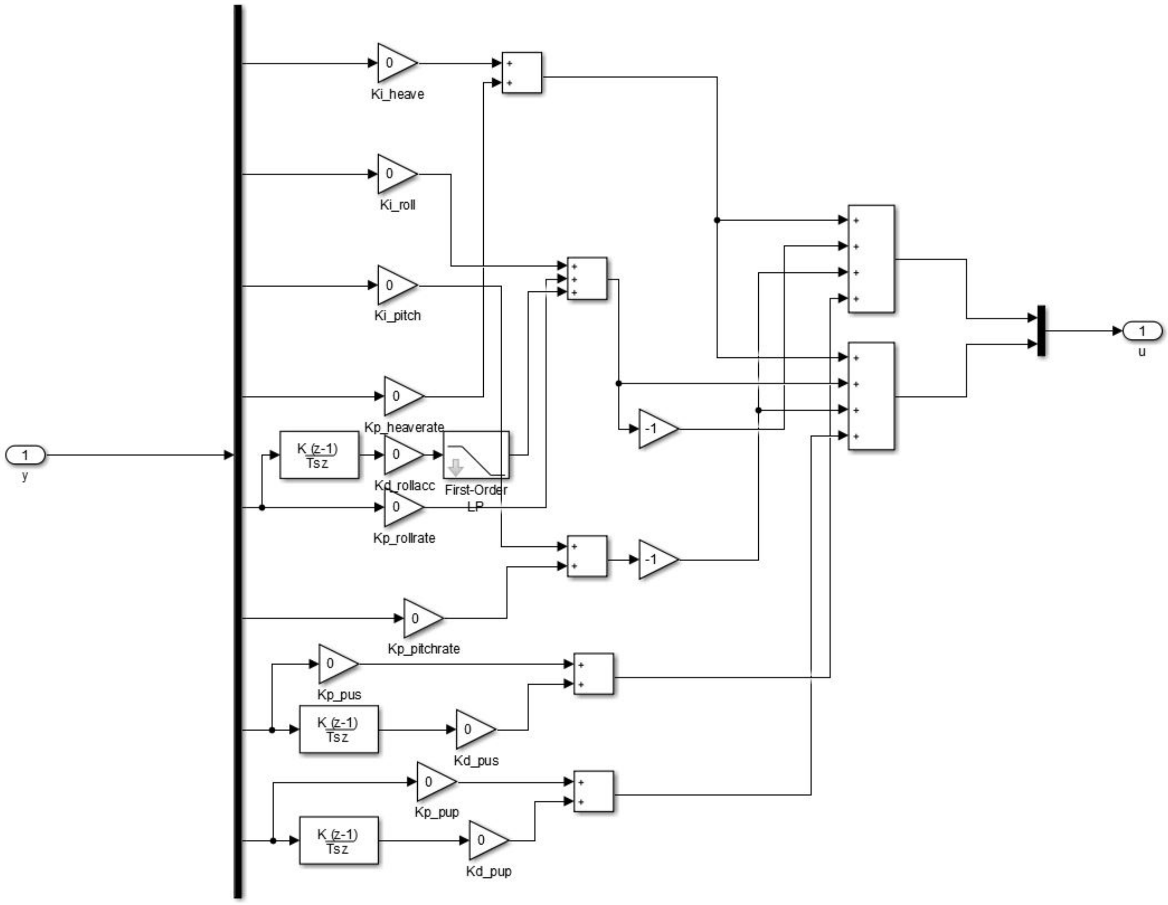

Figure C.13: Tunable controller.

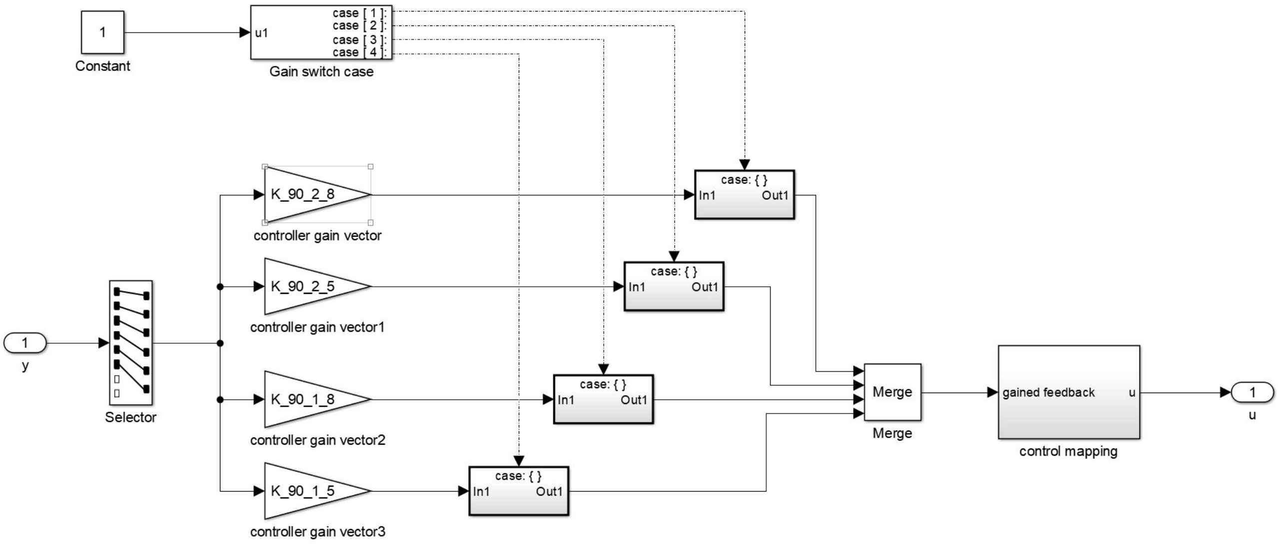

Figure C.14: Adaptive controller.

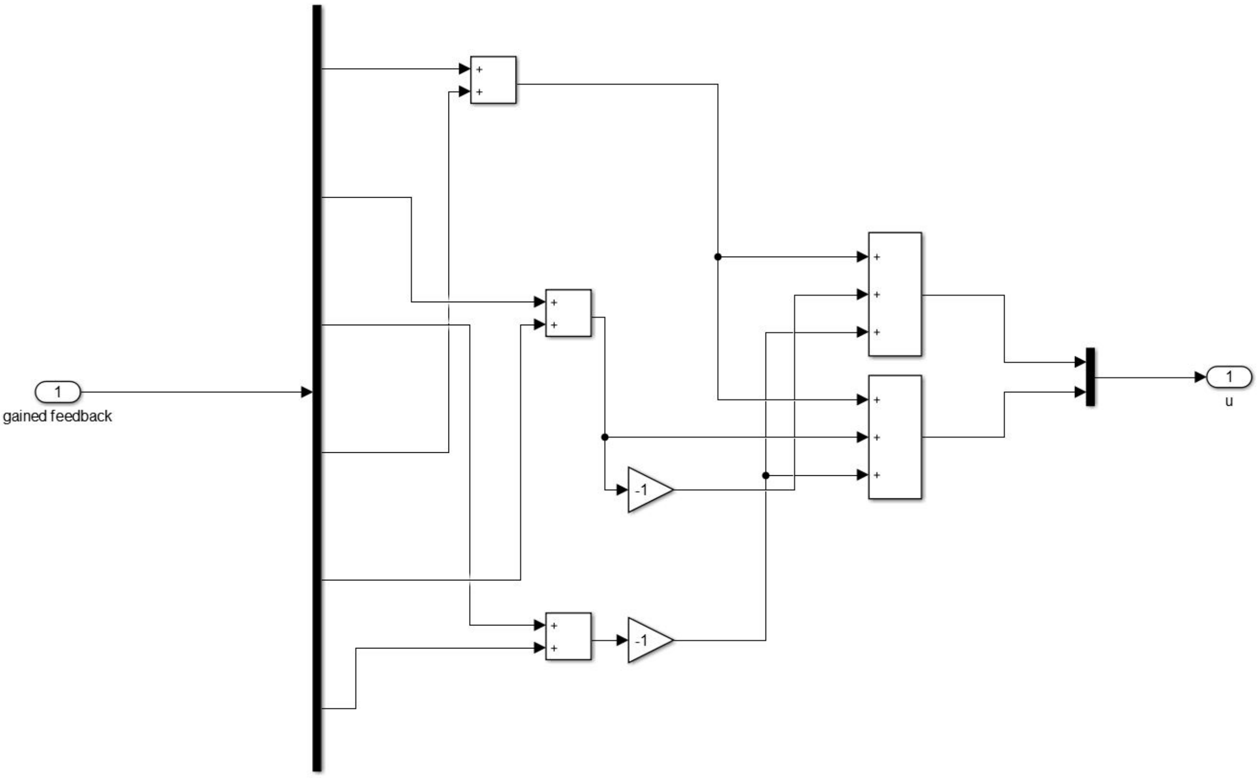

Figure C.15: Adaptive control mapping.